# DOCTORAL (PhD) DISSERTATION


# INVESTIGATION OF NEW COMPOSITION CVD COATING FORMULATIONS IN TERMS OF MECHANICAL PROPERTIES AND CUTTING EFFICIENCY

DOI:10.18136/PE.2025.940

**Compiled within the framework of the**
**University of Pannonia**
**Doctoral School of Chemical Engineering and Material Sciences**
**Material Sciences and Technology/Metallurgical Engineering**

Written by:

**Osamah Ihsan Ali**

MSc in Materials Engineering

Supervisor:

**Dr. István Gábor Gyurika**
Associate professor

Research Centre of Engineering Sciences, Department of Materials Engineering,
Faculty of Engineering
**University of Pannonia**

Veszprém, Hungary
2025

Investigation of New Composition CVD Coating Formulations in Terms of Mechanical Properties and Cutting Efficiency

Thesis for obtaining a PhD degree in the Doctoral School of Chemical Engineering and Material Sciences of the University of Pannonia in the branch of Material Sciences and Technology

Written by Osamah Ihsan Ali

Supervisor: Dr. István Gábor Gyurika

propose acceptance (yes / no) ……
(supervisor)

As reviewer, I propose acceptance of the thesis:

Name of Reviewer: ….....….…..... yes / no
……..
(reviewer)

Name of Reviewer: ….....….….....yes / no
……..
(reviewer)

The PhD-candidate has achieved ….....% at the public discussion.

Veszprém

…….
(Chairman of the Committee)

The grade of the PhD Diploma …..... (…….. %)

Veszprém

……
(Chairman of UDHC)

## ABSTRACT

This dissertation presents a comprehensive investigation into the tribological behavior, oxidation resistance, and wear properties of titanium nitride-based coatings produced by chemical vapor deposition (CVD) technology. The study investigates different coating compositions and microstructures, including bilayer TiN/TiC coatings and other TiN-based systems, applied to different substrates such as (WC-Co) cermet and alloy steel used in cutting tools applications. Advanced characterization techniques were used to evaluate the relationships between coating composition, structure, and performance. Tests included microscopy and spectroscopy (SEM with EDS, OM, and XRD), mechanical tests (Vickers micro-hardness, tribology, surface roughness, adhesion), and thermal measurements (thermal conductivity, infrared-imaging, and oxidation).

A key finding of this study is the superior suitability of zirconium oxide counterparts compared to steel for ball-on-disc wear test of bilayer TiN/TiC coatings. Unlike steel, which adheres to the coating surface within few seconds, zirconia counterpart do not cause adhesion or significant surface heating during the test. This discovery enables more accurate and reliable wear testing methodologies for hard coatings.

The oxidation behavior of bilayer TiN/TiC coatings was investigated using a novel approach. Oxidation tests revealed a significant increase in oxygen content accompanied with substantial decreases in carbon and nitrogen content due to the formation of gaseous by-products (CO, $CO_2$, and $N_2$). XRD analysis confirmed the transformation of the TiN coating into titanium oxide (rutile-$TiO_2$), attributed to complete nitrogen depletion. This oxidation process degraded the mechanical properties, including the tribological performance and Vickers-microhardness. Interestingly, the study observed colour change in the TiN/TiC coatings from gold/yellow to greyish-black during oxidation, providing a visual indicator for evaluate the oxidation stages and identifying damage in coated cutting tools.

Additionally, a comparative analysis of different TiN based CVD coatings with various elemental compositions (TiN/TiC, TiCN/Al/TiN, and TiCN) provided further insights into their tribological and mechanical properties. The results showed that, the surface roughness and the hardness had a greater influence on wear volume and stability of coatings rather than their thickness in terms of tribological performance.

## الخلاصــة

تقدم هذه الأطروحة دراسة شاملة للسلوك التريبولوجي (الاحتكاكي)، مقاومة الأكسدة، وخصائص البلى لطلاءات شديدة الصلابة قائمة على نيتريد التيتانيوم وتم انتاجها بواسطة تقنية الترسيب الكيميائي للبخار (CVD). تم خلال هذه العمل دراسة انظمة طلاءات صلبة ذات تركيب كيميائي مختلف ، عدد طبقات وبنية مجهرية متنوعة ، بما في ذلك طلاءات ثنائية الطبقة مثل (TiN/TiC) وأنظمة أخرى متعدة الطبقات (TiN-based systems) ، تم ترسيبها على ركائز مختلفة مثل كربيد التنغستن - كوبالت (cermet) والفولاذ السبائكي المستخدم في تطبيقات أدوات القطع. تم استخدام تقنيات توصيف متقدمة لتقييم العلاقة ما بين تركيب الطلاء وبنيته وأدائه. شملت اختبارات التصوير والتحليل الطيفي مثل (المجهر الإلكتروني الماسح مع التحليل الطيفي لتشتت الطاقة SEM/EDS ، المجهر الضوئي OM، وحيود الأشعة السينية)، واختبارات ميكانيكية مثل (الصلادة المجهرية الدقيقة (صلادة فيكرز)، الاختبارات التريبولوجية، خشونة السطح، ومقاومة الالتصاق)، اما الاختبارات الحرارية شملت (التوصيل الحراري، التصوير بالأشعة تحت الحمراء، واختبارات الأكسدة).

أحد اهم النتائج الرئيسية لهذه الدراسة هو التفوق الملحوظ لنظائر اوكسيد الزركونيوم ($ZrO_2$-counterpart) المستخدم في اختبارات البلى من نوع (ball-on-disc-wear tests) مقارنة بنظائر الفولاذ (steel-counterpart) المستخدمة في نفس الاختبار للطلاءات ثنائية الطبقة (TiN/TiC-CVD) ، على عكس الفولاذ الذي يلتصق بسطح الطلاء في غضون ثوانٍ قليلة، فإن اوكسيد الزركونيوم لا يسبب التصاقًا أو تسخينًا للسطح أثناء إجراء هذه الاختبارات، مما يسمح باستخدام منهجيات اختبار بلى أكثر دقة وموثوقية لهذا النوع من الطلاءات الصلبة.

تم التحقيق في سلوك أكسدة الطلاءات ثنائية الطبقة (TiN/TiC) باستخدام نهج جديد ، حيث كشفت اختبارات الأكسدة عن زيادة كبيرة في المحتوى الذري للأوكسجين (at.%) مصحوبة بانخفاض كبير في محتوى الكربون والنيتروجين بسبب تكوين وتحرر الغازات الناتجة من مهاجمة الاوكسجين لمكونات الطلاء عند درجات الحرارة العالية مثل ($N_2$ ،$CO_2$ ،CO). كما أكد تحليل حيود الاشعة السينية XRD تحول طبقة الحماية شديدة الصلابة المكونة من نتريد التيتانيوم إلى أكسيد التيتانيوم (روتيل-$TiO_2$)، والذي يُعزى إلى استنفاذ النيتروجين بالكامل. كذلك أدت عملية الأكسدة هذه إلى تدهور الخصائص الميكانيكية، بما في ذلك الأداء التريبولوجي والصلادة المجهرية فيكرز. ومن المثير للاهتمام أن الدراسة لاحظت تغيرًا كبيرا في لون هذه الطلاءات من الذهبي المصفر إلى اللون الرمادي المسود أثناء تقدم اختبارات الأكسدة حيث بعد كل دورة أكسدة تعطي لونا مختلفا لطبقات السطح المتأكسدة، مما يوفر مؤشرًا بصريًا لتقييم مراحل الأكسدة وتحديد التلف في أدوات القطع المطلية.

بالإضافة إلى ذلك، قدم التحليل المقارن لمختلف طلاءات CVD-TiN ذات التركيب الكيمياوي المختلف (TiN/TiC)، (TiCN/Al/TiN) و (TiCN) رؤى إضافية حول خصائصها التريبولوجية والميكانيكية. أظهرت النتائج أن خشونة السطح والصلادة كان لهما تأثير أكبر على حجم البلى واستقرار الطلاءات مقارنةً بسماكتها من حيث الأداء التريبولوجي.

## Table of contents

## List of tables

## List of figures

## List of symbols

| | |
|---|---|
| $\delta$ | boundary layer thickness |
| $\eta$ | viscosity |
| $\Theta$ | incident angle of the X-ray beam on the sample |
| $\mu$ | friction coefficient |
| $\mu_a$ | friction coefficient due to adhesion |
| $\mu_d$ | friction coefficient due to asperity deformation |
| $\mu_p$ | friction coefficient due to ploughing |
| $\rho$ | mass density |
| $d$ | grain size |
| $k$ | material constant in Hall-Petch relation |
| $k_w$ | wear rate |
| $n$ | number of considered peaks for the texture coefficient calculation |
| $p$ | vapor pressure in the bulk gas |
| $p_0$ | vapor pressure at the surface |
| $s$ | sliding distance |
| $v$ | gas flow velocity |
| $v_w$ | wear volume per unit sliding distance |
| $x$ | distance |
| $d$ | grain size |
| $k$ | material constant in Hall-Petch relation |

## List of abbreviations and acronyms

| | |
|---|---|
| APCVD | atmospheric pressure chemical vapor deposition |
| BSE | backscattered electron |
| CVD | chemical vapor deposition |
| EDS | energy dispersive spectroscopy |
| GAXRD | glancing angle X-ray diffraction |
| GDOES | glow discharge optical emission spectroscopy |
| GIR-FTIR | grazing incidence reflection Fourier transform infrared |
| HTCVD | high temperature chemical vapor deposition |
| ICDD | international centre for diffraction data |
| JCPDS | joint committee of powder diffraction standards |
| LOM | light optical microscopy |
| LPCVD | low pressure chemical vapor deposition |
| LTCVD | low temperature chemical vapor deposition |
| MOCVD | metal organic chemical vapor deposition |
| MTCVD | medium temperature chemical vapor deposition |
| PACVD | photo-assisted chemical vapor deposition |
| PECVD | plasma-enhanced chemical vapor deposition |
| PVD | physical vapor deposition |
| SE | secondary electron |
| SEM | scanning electron microscopy |
| TACVD | thermally activated chemical vapor deposition |
| UHVCVD | ultrahigh vacuum chemical vapor deposition |
| XRD | X-ray diffraction |

# Acknowledgement

This dissertation was carried out as part of the research activities at the Research Centre of Engineering Sciences, Faculty of Engineering, University of Pannonia. I would like to express my deepest gratitude to my supervisor, Dr. István Gábor Gyurika, whose invaluable guidance, encouragement, and advice have been instrumental in shaping this work. I am also continuously thankful to Dr. Miklós Jakab for his crucial support, help and motivation throughout this journey. Their regular monitoring and dedicated time have been vital to my success over these four years.

Additionally, I extend my heartfelt gratitude to Dr. Tamás Korim, the head of the Research Centre of Engineering Sciences, Department of Materials Engineering, for his unwavering help and support.

I am deeply appreciative of all my colleagues I had the privilege to exchange ideas and knowledge: Mrs. Éva Pfeifer, Dr. Olga Shypul, Mr. Miklós Boleraczki, Mr. István Béni, Mr. Szabolcs Hanich and Ms. Ivett Simon. Your patience and assistance have been truly invaluable.

I cannot extend enough thanks to my family, especially my parents, brothers, and sisters, whose constant encouragement has been a cornerstone of my perseverance throughout this process.

Finally, this work would have been an immeasurably more difficult feat without the unwavering support of my caring lovely wife and my little angel Sunan. Thank you both for your steadfast support and for reminding me to take breaks and enjoy moments of fun when I felt overwhelmed.

# 1. Introduction

In metal cutting operations, tool performance directly effects on the manufacturing efficiency, productivity, and the costs. As industrial demand for machined components continues to rise, enhancing the durability and performance of cutting tools has become a critical technological challenge (*Mayrhofer et al., 2006*). This dissertation addresses this challenge through a comprehensive investigation of titanium nitride (TiN)-based coatings deposited by chemical vapor deposition (CVD), with a particular focus on their tribological behavior, oxidation resistance, and wear properties. The present study focuses on the following key areas:

1. Establish more reliable testing methodologies for evaluating the tribological performance of hard coatings.
2. Characterize the oxidation behavior of bilayer TiN/TiC coatings under high-temperature conditions.
3. Identify the relationship between coating composition, microstructure, and layers thickness for enhanced wear resistance and thermal stability.

This study employs advanced characterization techniques, including scanning electron microscopy with energy-dispersive X-ray spectroscopy (SEM-EDS), optical microscopy (OM), X-ray diffraction (XRD), mechanical testing (Vickers microhardness, tribology, surface roughness, adhesion), and thermal analysis (thermal conductivity, infrared imaging, and oxidation testing). This multifaceted approach enables a comprehensive evaluation of different coating systems, including bilayer TiN/TiC, TiCN/Al/TiN, and other TiN-based coatings applied to WC-Co cermet and steel substrates.

This research provides significant contributions by developing more accurate wear testing protocols to enhance the reliability of coating performance evaluations, deeper understanding of oxidation behavior to extend tool life in high-temperature applications, and identifying optimal coating compositions and structures to improve tribological performance.

The following sections constitute the first part of this dissertation, focusing on the properties and production of CVD hard coatings. This part is divided into three main

subsections: the CVD coating process, types of CVD hard coatings, and the properties of CVD hard coatings, as outlined in the subsequent sections.

## 2. Properties and production of CVD hard coatings

Today, with increasing performance requirements for machined components, the application of hard coatings has emerged as a powerful solution to improve the properties of cutting tools against wear and thermal shock under service conditions. For over three decades, depositing hard coatings onto cemented carbide cutting tools has proven remarkably effective in enhancing tool lifetime and cutting performance. The commercial application of these coatings began with the thermal chemical vapor deposition (CVD) process. Over the years, various plasma-assisted physical vapor deposition (PVD) techniques, have also been introduced (*Gissler & Jehn, 1992; Akgün et al., 2023*).

Currently, hard coatings have evolved into complex composites consisting of various materials, each fulfilling different requirements, such as excellent adhesion to the substrate with minimal interaction with the workpiece material (*Lavrinenko, 2022*). The development of hard coatings initially began with the single-phase coatings such as $Al_2O_3$. Subsequently, the variety expanded with the development of hard materials such as TiC and TiN. Since the mid-1980s, the deposition of these coating structures has garnered considerable interest. The coatings within the Ti-C-N system are widely used in the cutting tool industry. The substitution of Ti atoms in the face-centered cubic (fcc) TiN lattice by N results in hard coatings, typically referred to as fcc-$Ti_{1-x}C_xN$ ($0 \leq x \leq 1$) coatings. These coatings exhibit high oxidation resistance, superior tribological properties, and excellent hardness (*Xin et al., 2022*).

### 2.1 The CVD coating process

This sub-section is one of the main subjects of the section one and it provides an overview of CVD coatings and focuses on the CVD system process, the principles and mechanisms, as well the structure of the coatings.

### 2.1.1 Overview of CVD coating processes

Chemical vapor deposition (CVD) is a complex process in which solid materials are deposited on a substrate through the chemical reactions of gaseous precursors. For cutting tools, CVD processes have been used to deposit thin film layers of the coatings on substrates such as cemented carbide, oxides, cermet, etc. (*Carlsson & Martin, 2010*). These coatings are typically composed of refractory materials like titanium nitride (TiN), titanium carbonitride (TiCN), and titanium aluminum nitride (TiAlN), as well as other materials like chromium nitride (CrN) and diamond-like carbon (DLC) coatings. CVD techniques are classified based on specific process characteristics (*Choy, 2003; Pierson, 1999*):

1. Reaction activation method: This category includes thermally activated chemical vapor deposition (TACVD), often referred to as thermal CVD or conventional CVD, as well as plasma-enhanced CVD (PECVD) and photo-assisted CVD (PACVD).
2. Precursor type: Metal-organic chemical vapor deposition (MOCVD) employs metal atoms combined with organic radicals.
3. Temperature range: Processes can be categorized based on temperature: high-temperature CVD (HTCVD) operates between 850-1200°C, medium-temperature CVD (MTCVD) functions at 700-850°C, and low-temperature CVD (LTCVD) is conducted below 700°C.
4. Deposition pressure: This includes atmospheric pressure CVD (APCVD) at 105 Pa, low pressure CVD (LPCVD) ranging from 10 to 1000 Pa, and ultrahigh vacuum CVD (UHVCVD) at pressures below 0.1 Pa.

This present study focuses on the process of thermal chemical vapor deposition (CVD), particular the deposition of hard coatings for cutting tools application. Thermal CVD is a powerful technique that offers a multitude of advantages, notably its ability to uniformly deposit coatings on geometrically complex parts. High deposition rate, CVD can deposit single/multi layers of coatings. Additionally, CVD is highly flexible, as the equipment typically does not require ultrahigh vacuum conditions. Moreover, CVD can be more economical than physical vapor deposition (PVD) process, as it does not demand the same level of vacuum technology and is suitable for a wide range of applications. However, CVD also has certain limitations. One significant drawback is

the high temperature requirement; CVD is most effective at temperatures of 700°C and above, which can be problematic for substrates that are not thermally stable at these temperatures. Furthermore, CVD necessitates chemical precursors with high vapor pressure, which can be hazardous and sometimes extremely toxic. The by-products of CVD reactions are also maybe a toxic and corrosive (*Hitchman & Jensen, 1993*).

### 2.1.2 CVD coating systems

Chemical vapor deposition (CVD) systems are highly adaptable and can be tailored to specific coating materials or substrate geometries. Regardless of the process type, all CVD systems consist of three principal components: a chemical vapor precursor supply system, a CVD reactor, and an exhaust gas treatment unit (*Ohring, 2002*). Figure 1 illustrates a schematic of a production unit designed for applying coatings on cutting tools. The precursor supply system generates and delivers gaseous precursors into the reactor. Gaseous precursors, such as argon, hydrogen, or nitrogen, can be metered and fed directly from gas cylinders. However, liquid and solid reactants require specialized equipment. Liquid precursors are typically evaporated in a bubbler system, where an inert carrier gas, like argon or hydrogen, flows through the precursor liquid. The evaporated reactant saturates the gas phase and is delivered into the reactor. The precursor concentration can be controlled by adjusting the liquid precursor temperature, carrier gas flow rate, and total pressure. Temperature regulation of bubblers is crucial, as the heat removal during evaporation can change the precursor partial pressure. This issue can be mitigated by utilizing flash-evaporation, where the liquid is directly evaporated in a gas stream using pumps. Common liquid precursors for hard coating deposition include titanium tetrachloride ($TiCl_4$) and acetonitrile ($CH_3CN$) (*Larsson & Ruppi, 2002*).

Evaporation of solid precursors can be challenging, as high temperatures are often required. For instance, the titanium-containing precursor titanium tetrachloride ($TiCl_4$) is created by reacting titanium with hydrogen chloride (HCl) at temperatures above of the $TiCl_4$ sublimation temperature. The vapor is then transferred with a carrier gas into the reactor (*Herzler & Roth, 2002*).

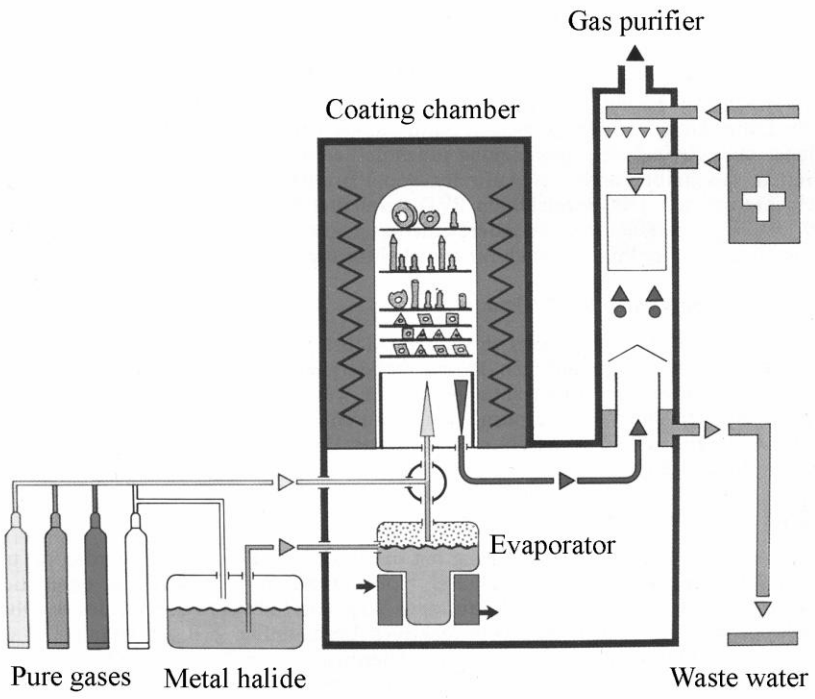


**Figure 1**: CVD production unit (*Wagner, 2007*).

The CVD reactor isolates the reaction gases from the environment and heats the substrates to the deposition temperature. Reactors can be classified as hot-wall or cold-wall systems. In hot-wall systems, the entire reactor is heated, while in cold-wall systems, only the substrate is heated. The cutting tool industry primarily utilizes hot-wall reactors, where the entire interior, including the reactor wall, is coated. This can lead to precursor depletion effects. After the deposition process, the exhaust gas treatment unit neutralizes the remaining precursors and by-products in the system. Water and sodium hydroxide are commonly used to decompose and neutralize metal chlorides and released hydrogen chloride (HCl) (*Love et al., 1993; Abu-Thabit & Makhlouf, 2020*).

### 2.1.3 Principles and mechanisms of the CVD coating process

Chemical vapor deposition (CVD) designed to form thin film layers of coatings onto heated substrate surfaces under controlled atmospheric conditions. The main steps in the CVD process are schematically illustrated in Figure 2. The gas flow plays a significant role in the deposition process. Key steps of the deposition process occur as follows (*Carlsson & Martin, 2010*):

1. **Transport of reactants:** The process begins with the movement of gaseous reactants into the reaction chamber where intermediate species are formed.

2. **Surface reactions at lower temperatures:** This includes heterogeneous reactions on the surface that occur at temperatures below the dissociation temperature of the intermediate species:

   a. The gaseous reactants move across the boundary layer and adsorb onto the substrate surface.

   b. Chemical reactions take place between the adsorbed species and/or between vapor phase species.

   c. The deposits spread along the surface, forming nucleation centers and aiding in the film's growth.

   d. By-products desorb from the surface and diffuse through the boundary layer into the bulk gas.
3. **Homogeneous gas phase reactions:** At higher temperatures, intermediate species react within the gas phase.
4. **Removal of by-products:** By-products and any unreacted precursors are removed from the deposition chamber.

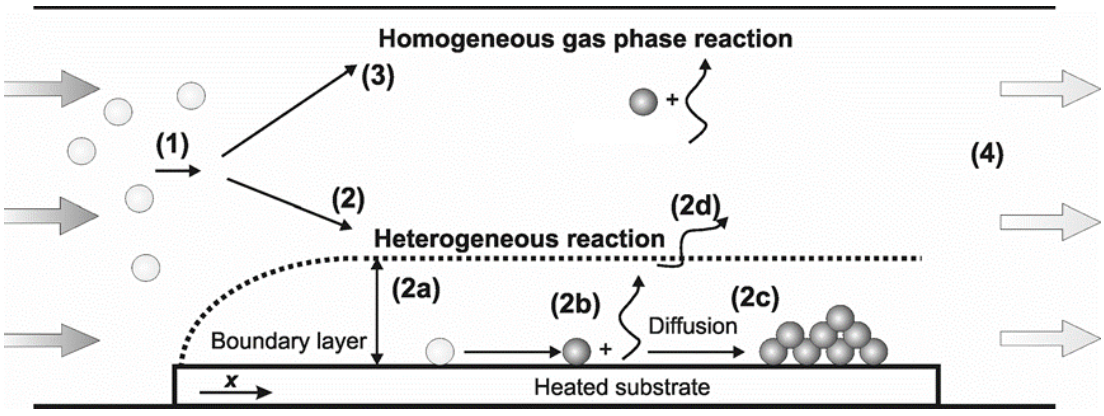


**Figure 2**: Key steps in the CVD process (*Ohring, 1992*).

It is worth mentioning that each of these steps influences the deposition of coatings and consequently the coating properties, such as growth rate, uniformity, stoichiometry, structure, and density (*Vargas Garcia & Goto, 2003*). The principles of the CVD process involve gas transport, ensuring uniform reactant delivery, and kinetic considerations, focusing on reaction driving forces and rates, as described in the following sub-sections:

#### 2.1.3.1 Gas transport

The availability and distribution of precursors within the CVD reactor are dominated by the intricate nature of gas transport phenomena. Consequently, reactant transport plays

a pivotal role in determining the coating thickness uniformity, deposition efficiency, and the structure and properties of the coatings (*Kafizas et al., 2013*). Typically, CVD processes operate at low flow velocities to maintain laminar flow. High velocities would induce turbulence, inhibiting the formation of uniform films. During laminar viscous flow, a boundary layer forms at the substrate surface, where the flow velocity, gas concentration, and temperature change from those in the main gas stream. Consequently, gradients in the velocity, concentration, and temperature profiles develop around the substrate. These profiles exert a crucial influence on the deposited coatings, as the chemical reactions occur within this region (*Pedersen & Elliott, 2014*). The thickness $\delta$ of boundary layer at a position $x$ on the substrate is given by (*Carlsson, 1985*):

$$\delta \propto (\eta x/\rho v)^{1/2} \tag{1.1}$$

Considering gas viscosity ($\eta$), gas density ($\rho$), and flow velocity ($v$), the boundary layer expands with decreased flow velocities. The temperature and pressure dependence of $\eta$ and $\rho$ suggest that the boundary layer thickness increases with higher temperatures and lower total pressures, respectively. These processes play a crucial role in mass transport through the boundary layer. The flux ($J$) through the boundary layer is expressed as (*Ohring, 1992*):

$$J = -D\,[(p - p_0) / (\delta RT)] \tag{1.2}$$

where $D$ represents diffusivity, $p$ denotes the vapor pressure in the bulk gas, $p_o$ signifies the vapor pressure at the surface, $R$ stands for the universal gas constant, and $T$ represents the absolute temperature. The gas diffusivity can be calculated by use the kinetic theory of gases (*Ohring, 1992*):

$$D \propto (T^{3/2}/p) \tag{1.3}$$

According to equation 1.3, decreasing pressure enhance the diffusivity. Mass transport, as per equation 1.2, is directly proportional to the ratio of diffusivity ($D$) to boundary layer thickness ($\delta$). While both $D$ and $\delta$ increase with decreasing pressure, the increase in diffusivity outweighs the effect of the thicker boundary layer $\delta$. Low-pressure CVD systems capitalize on this enhanced mass transport for efficient deposition processes (*Wagner, 2007*).

#### 2.1.3.2 Kinetic considerations in film growth

The kinetics of chemical vapor deposition (CVD) film growth is a complex phenomenon, involving various processes at the gas/substrate interface. The growth of thin films via CVD is a multistep process, including several distinct stages. Initially, the gaseous precursor species must undergo mass transport from the bulk gas phase to the substrate surface. Upon reaching the surface, the precursor molecules undergo adsorption, a process dominated by the surface characteristics and the strength of intermolecular interactions. Subsequent to adsorption, the adsorbed species may undergo dissociation or surface migration, driven by the thermal energy supplied to the system. These surface processes lead to the formation of stable nuclei, which act as seeds for film growth. As the deposition progresses, the nuclei combine, leading to the formation of a continuous film. Simultaneously, the by-products of the chemical reactions desorb from the surface and undergo mass transport back to the bulk gas phase, facilitated by diffusion and convection mechanisms. The complex interactions between these various steps dominate the overall kinetics of the film growth process. Typically, the individual steps which are influenced by parameters such as the temperature inside the reactor, the coating process time, the pressure, and precursor concentrations, collectively determine the overall growth rate and the resulting film properties (*Gao & Zhang, 2017; Wang & Wu, 2023*). Consequently, a comprehensive understanding of the growth kinetics is crucial for optimizing the CVD process and achieving the desired characteristics in thin film layers of CVD coatings. Generally, the rate-controlling mechanisms in CVD can be classified into two categories (*Choy, 2003*):

1. **Surface kinetics control**: In this scenario, the growth rate is constrained by the processes occurring at the surface, such as chemical reactions, lattice incorporation, or the desorption of by-products. The growth rate is slower than the mass transport to or from the surface.
2. **Mass transport control**: The processes at the surface occur more rapidly than the mass transport to the surface.

The determination of the rate-limiting mechanism can be inferred from the temperature behavior of the growth rate. According to the Arrhenius law, the growth rate ($R_d$) in CVD reactions follows the equation (*Carlsson, 1985*):

$$R_d = A \cdot e^{(-Ea/RT)} \quad (1.4)$$

where $A$ is exponential factor and $E_a$ is activation energy. Schematic Arrhenius plots (ln $R_d$ – $1/T$) illustrate this relationship for different total pressures ($p_1$, $p_2$, and $p_3$) as depicted in Figure 3. The diffusivity of reactants, representing mass transport, can be increased by reducing the total pressure, as per equation 1.3. Consequently, a decrease in pressure extends the surface kinetics control to higher temperatures. Most CVD processes operate within the domain of surface kinetics control. The abundant availability of precursors and the slow chemical reaction facilitate the deposition of homogeneous coatings, independent of the reactor or the geometry of substrate, as reported by (*Christian, 2002; Acosta, 2021*).

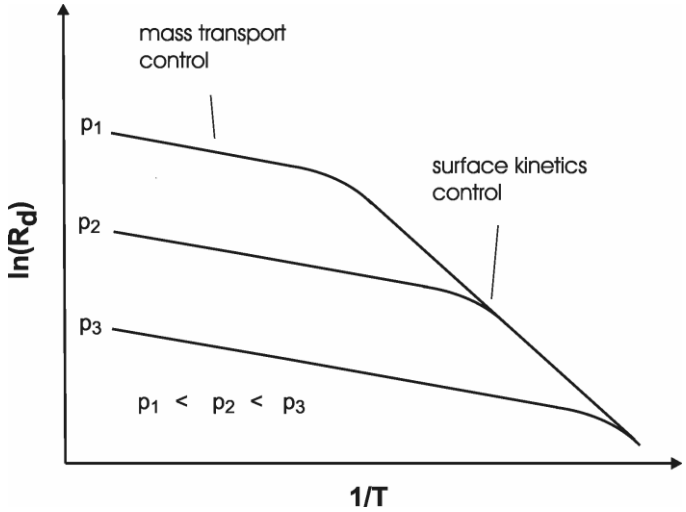


**Figure 3:** Arrhenius plots illustrates the effect of total pressure on the growth rate (*Acosta, 2021*).

### 2.1.4 The coating's structure

The coating structure greatly affected by the growth of thin films. The growth stages illustrated in the Figure 4, initial stage involves the primary nucleation of clusters on the surface of substrate, initiating condensation and film growth (stage 1). This nucleation phase is significantly impacted by the structural preconditions and chemical composition of the substrate (*Juarez et al., 2003*). Notably, the nature of the substrate can affect in the chemical reactions, potentially acting as a catalyst to activate reactions. Organic compounds, such as $CH_4$, are particularly susceptible to catalytic substrate effects. Additionally, high temperatures and chemically aggressive precursors may attack the substrate, altering the substrate and coating composition. Following the nucleation stage, dispersed crystals begin to grow (stage 2), as described by (*Jin et al., 2013*).

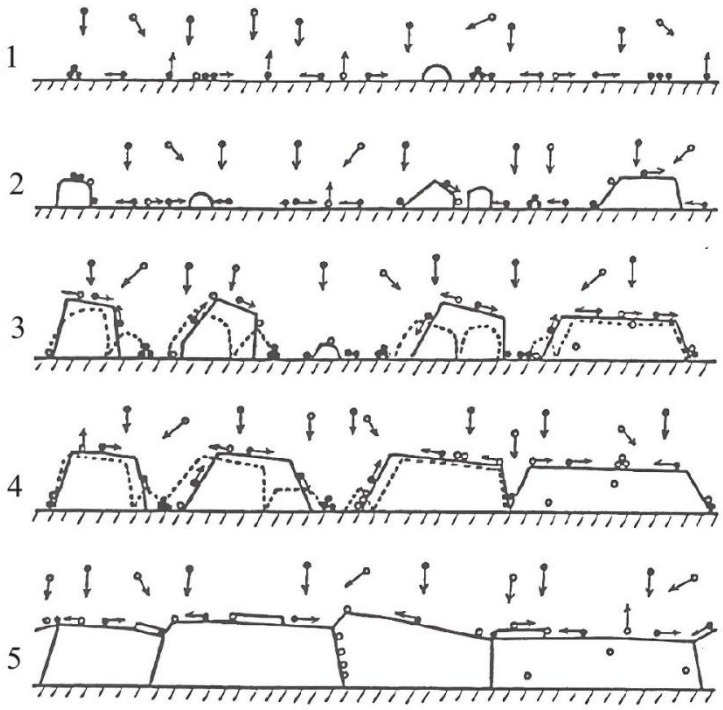


**Figure 4**: Evolutionary stages of structure in polycrystalline thin films: 1.) nucleation; 2.) crystal (grain) growth; 3.) coalescence; 4.) filling of channels; 5.) continuous film growth (dark circles indicate coating material, bright circles represent impurities) (*Wagner, 2007*).

The orientation of these crystals plays a significant role in determining the subsequent growth processes. Growth occurs through direct particle capture from the vapor phase and migration of adsorbed coating species. As crystal size increases, adjacent crystals come into contact, initiating the coalescence stage (stage 3). Complete coalescence leads to the formation of new separate crystals, causing changes in crystals orientation and the development of a structured texture associated with the lowest interface energy. This stage accompanied by the contraction of coalescing crystals, leaving some uncovered substrate areas, but continuous the condensation in these areas leads to secondary nucleation and new grains, initiating a cycle of nucleation and grain growth. Over time, channels between crystals are filled (stage 4), followed by continuous film growth (stage 5), characterized by crystals of various orientations and different types of grain boundaries. Defects, such as screw dislocations, stacking faults, or irregular corners, can influence the growth rate and result in highly textured coatings. These defects may originate as early as the nucleation stage. For instance, low deposition temperatures during the chemical vapor deposition (CVD) of titanium nitride (TiN) promote the formation of twinned crystals. In the case of laminated twins (see Figure 5a), the most

rapid growth occurs along the (211) direction, aligned with the re-entrant corners of the (111) twin plane. Consequently, the resulting coating morphology displays pyramidal or lenticular-like TiN structures. In the case of multiply twinned crystals, growth along (111) twin planes with (110) co-axis results in star-shaped crystals, as shown in Figure 5b. A combination of star-shaped and lenticular-like structures can be observed in Figure 5c. Scanning electron microscopy (SEM) image depicts the surface of a TiN coating deposited at 850°C. Elevated deposition temperatures lead to twin-free nuclei and coating growth along thermodynamically favorable crystal faces, resulting in polyhedral structures. Impurities or additives may obstruct crystal growth, leading to repeated nucleation and inhibiting further coating growth. Consequently, the resulting film consists of equiaxed, rounded crystals interspersed with the impurity phase (*Acosta, 2021; Mei et al., 2023*).

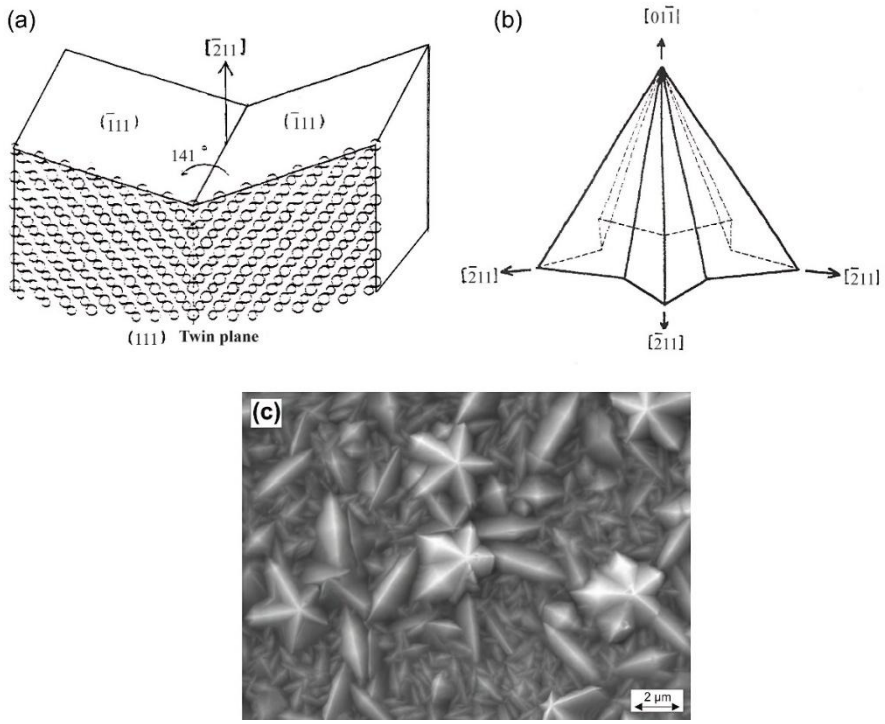


**Figure 5:** Schematic illustration of laminated twinned crystal (a); multiply twinned star-shaped crystal (b); and SEM image of TiN surface (c) (*Wagner, 2007*).

The development of structure zone models (SZMs) has significantly advanced our understanding of the correlation between deposition process parameters and coating structure, ultimately influencing the resultant properties. The first SZM, introduced by Movchan and Demchishin, linked the structure of thick vacuum-condensed metallic and oxidic coatings to the homologous temperature $T_s/T_m$ where, $T_s$ is the substrate

temperature and $T_m$ is the melting point of the coating material (*Movchan & Demchishin, 1969*). This parameter serves as an indicator of diffusivity (i.e., surface and bulk diffusion) and desorption of the coating material. They categorized the observed structures based on the homologous temperature $T_s/T_m$ into three distinct zones, as shown in Figure 6. In Zone 1, the surface mobility of condensed atoms is minimal or non-existent, resulting in porous columnar structures. Zone 2, dominated by surface diffusion, producing dense columnar grains extending from the bottom to the top of the film. In Zone 3, bulk diffusion becomes predominant, leading to a recrystallized structure with equiaxed grains and further densification of the film (*Schalk et al., 2022*). Thornton considered the inert sputtering gas pressure into the model and identified a fourth zone, the transition zone (Zone T), between Zones 1 and 2. In Zone T, surface diffusion is more pronounced than in Zone 1, resulting in competitive growth and a denser fibrous structure (*Thornton, 1974*).

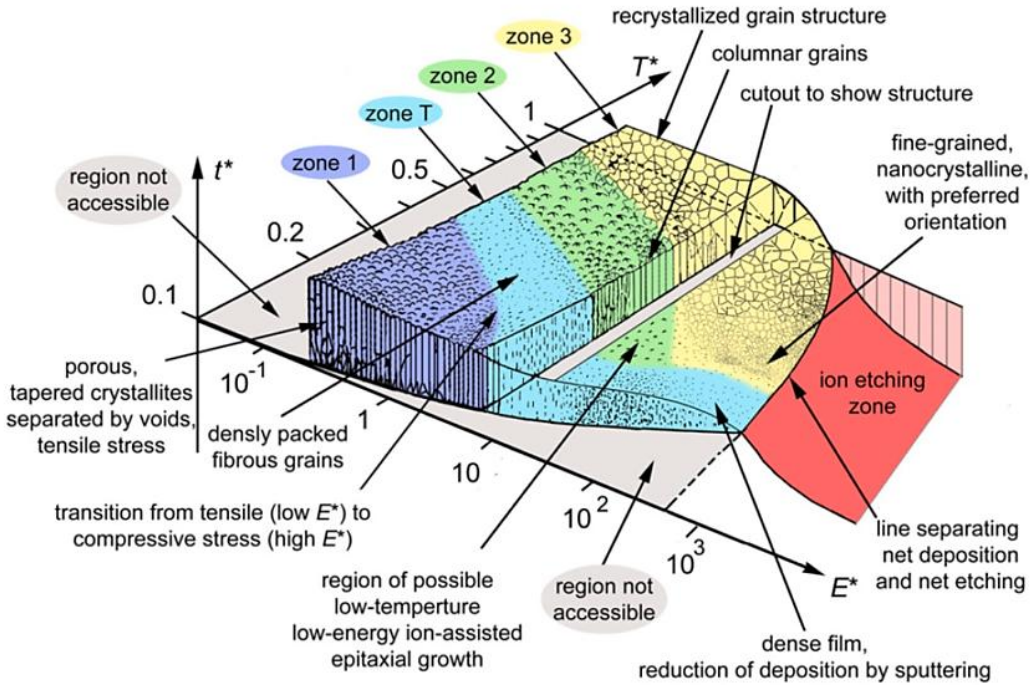


**Figure 6:** Structure zone model for CVD thin film growth (*Schalk et al., 2022*).

Finally, in CVD processes may occurs supersaturation which influenced by the temperature due to the thermally activated of the reactions. When the temperature is low and supersaturation is very high, the adsorbed species have limited mobility, causing the deposition reaction to happen mainly at the initial adsorption sites, which results in amorphous structures. As the temperature increases and supersaturation decreases, the deposits become more crystalline and form fine equiaxed polycrystalline structures.

With further temperature increases, the mobility of the adsorbed species rises, leading to coarser, dendritic structures. At low supersaturation and high temperatures, growth evolves from platelet structures to eventually epitaxial structures, as shown in Figure 7 (*Martin, 2010; Mayrhofer et al., 2006*).

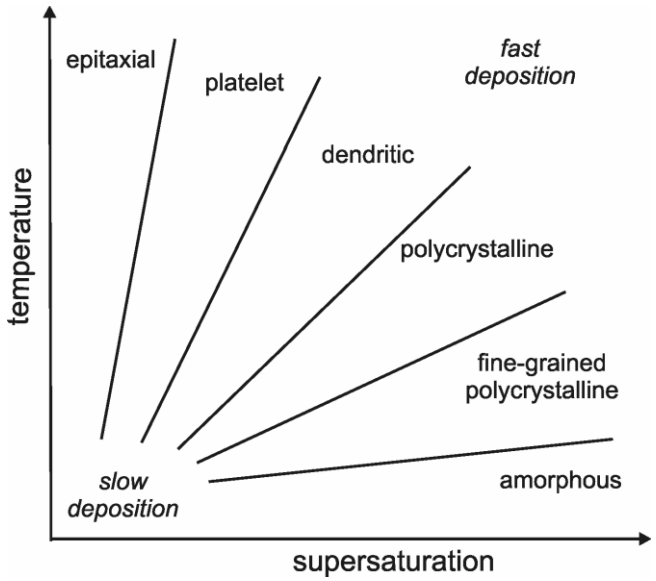


**Figure 7:** Influence of supersaturation and temperature on coating morphology (*Martin, 2010*).

### 2.1.5 Substrate materials for Ti-based CVD coatings

Many materials used as substrates for the deposition of Ti-based chemical vapor deposition coatings, as showed in Table 1. The selected substrates included cermets, cemented carbides, and steel, all of which are commonly used in various machining operations such as metal cutting, milling, and turning. Therefore, it is necessary to enhance the mechanical properties and oxidation resistance of these substrates (*Choy, 2003*). Generally, the cermet is a material consists of both ceramic and metallic components. This combination allows cermets to integrate the desirable properties of ceramics, such as high temperature resistance and hardness, with those of metals, such as plastic deformability. In cermets, the metal typically utilized as a binder for an oxides or a carbides. Commonly, used tungsten carbide with the cobalt (*Zhou et al., 2024*). Additionally, the steel-base substrates known for their ability to retain hardness at elevated temperatures, are extensively used in applications such as metal cutting, milling, and turning after applying the CVD coatings (*Bjerke et al., 2022*).

**Table 1**: Overview of studies on various substrates used for deposit CVD coatings.

| Substrates | Coatings | Improvements | Applications | Refs. |
|---|---|---|---|---|
| WC- 6.0 wt.% Co | TiCN, TiAlN | Tribological properties | Inserts for cutting tools | (*Kimura et al., 2001*) |
| WC- 15.0 wt.% TiC | TiCN, TiAlN, $Al_2O_3$ | Tribological, wear properties and hardness | Metal cutting tools, milling and turning | (*Schwanekamp et al., 2022*) |
| WC- 7.5 wt.% Co | TiCN, TiAlN | Tribological and wear properties | Metal cutting tools, milling and turning | (*Singh et al., 2024*) |
| High speed steel | TiCN, SiC, TiAlN, $Al_2O_3$ | Wear, oxidation | Metal machining | (*Alcántara, 2020*) |
| 42CrMo steel | TIC, Ti(C,N), TiN and $A1_2O_3$ | Wear resistance | Bearings, shafts, cams and tappets | (*Ruppi et al., 1998*) |
| Alloy steels, cast irons | Ti-base coatings, SiC, $Al_2O_3$ | Oxidation, abrasive and corrosion | Heat-exchangers, Mining tools and burners | (*Bjerke et al., 2022*) |
| Hot work tool steel, carbon steel, alloy steel | WC, Ti-base coatings, $Al_2O_3$ | Wear, extend service tools life, Oxidation | Extrusion dies, metrology parts, bearings and hot and cold forming tools | (*Bejjani et al., 2021*; *Zhao et al., 2022*) |
| Ti-6Al-4V alloy | Boron-films, SiC, TiCN | Hardness and wear | Bearings, high-performance cars parts | (*Din et al., 2018*; *Han et al., 1998*) |
| Graphite | TiCN, TiAlN, SiC | Oxidation | Heater elements | (*Kumar et al., 2017*) |

In this study, the focus was primarily on cermets and steels, due to their importance in industrial applications. So, applied Ti-based CVD coatings on these substrates aims to improve and enhance the surface properties, such as hardness, wear-resistant, oxidation resistance, increase the estimate cutting-tools life and improve machining performance.

### 2.2 Types of CVD hard coatings

The deposition of hard coatings is a significant method for protecting and prolonging the service lifetime of tools. Over the years, various coating materials have been developed for this purpose, such as titanium nitride (TiN), titanium carbide (TiC), and titanium aluminum nitride (TiAlN), etc., each tailored to specific requirements *(Qiu et al., 2024*). The current study focuses on titanium nitride (TiN) based coatings produced via CVD technique, given their widespread utilization and well-established efficacy in providing desired functional characteristics. Titanium nitride (TiN) based coatings have garnered significant attention due to their exceptional hardness, chemical stability, and wear resistance, making them highly suitable for applications demanding superior

tribological performance and durability. The synergistic combination of CVD coatings materials, which employed as multilayer structures, offers a unique opportunity to utilize the complementary strengths of each constituent, thereby enhancing overall performance and expanding the range of potential applications, especially in machining workpieces during cutting operations (*Yang et al., 2023*).

### 2.2.1 TiN coatings

The application of titanium nitride (TiN) as a hard coating is well established in the cutting industry due to its exceptional combination of hardness, toughness, and thermal stability. Classified as an interstitial compound, TiN crystallizes in a face-centered cubic (fcc) B1-NaCl structure (*Veprek et al., 2005*). The binary phase diagram illustrating the Ti–N system elucidates the wide stability range of TiN over varying compositions, (Figure 8). Reported nitrogen-to-titanium ratios for bulk TiN materials range from 0.6 to 1.16. In under-stoichiometric thin films (N/Ti < 1.0), vacancies reside on the nitrogen sub-lattice, while over-stoichiometric compositions (N/Ti > 1.0) feature vacancies on the titanium sub-lattice (*Azadi et al., 2014*).

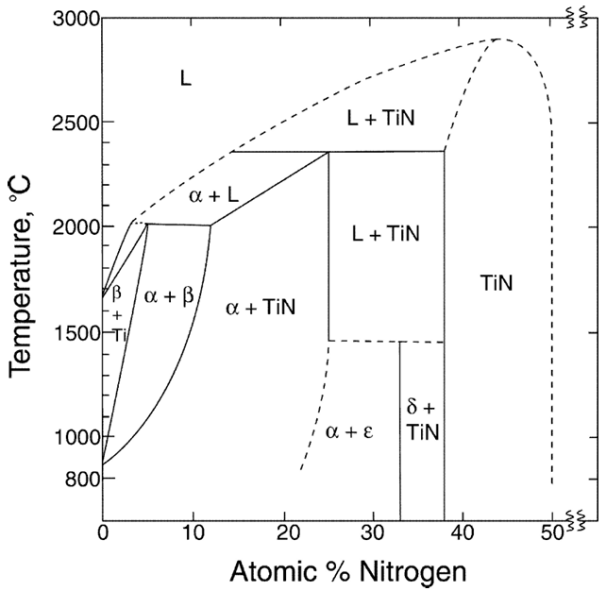


**Figure 8:** The binary phase diagram of the Ti-N system (*Pal & Deevi, 2003*).

The presence of vacancies and their distribution within the TiN lattice can significantly influence the material's properties, such as hardness, toughness, and oxidation resistance. Formore, Cheng et al., reported that under-stoichiometric TiN coatings with nitrogen vacancies exhibited higher hardness compared to stoichiometric or over-stoichiometric compositions (*Cheng et al., 2010*). The thermal chemical vapor

deposition (CVD) of TiN onto cemented carbide cutting tools conventionally employs gas mixtures comprising titanium tetrachloride ($TiCl_4$), nitrogen ($N_2$), hydrogen ($H_2$), and argon (Ar). $TiCl_4$ and $N_2$ serve as the source materials for coating constituents, with $H_2$ functioning as the reducing agent. Ar, an inert gas component, acts as a carrier gas and facilitates the achieve of the appropriate mass fluxes to ensure deposition rates. Typically, these coatings exhibit stoichiometric compositions with minimal chlorine incorporation and demonstrate excellent adhesion to cemented carbide substrates, featuring a columnar microstructure (*Cheng et al., 2010*). Additionally, substitution of nitrogen source $N_2$ with ammonia ($NH_3$) in the reaction allows for reduction in process temperatures for TiN formation, typically in the range of 550°C to 750°C. This low-temperature process, predominantly explored in microelectronics for TiN application as a diffusion barrier, offers a fine-grained structure, although with potential drawbacks including lower film density and incorporation of elevated chlorine content, as noted by (*Rebouta, 1995; Wächtler et al., 2024*).

### 2.2.2 TiC coatings

In recent years, research has focused on synthesizing TiC coatings using deposition methods, particularly chemical vapor deposition (CVD) technology to coat cutting tools (Mhadhbi, 2020). The TiC system consists of solid phases α-Ti, β-Ti, and a refractory monocarbide (TiC), as illustrated in Figure 9, which depicts the binary phase diagram of the Ti-C system. Also, titanium carbide with chemical formula TiC, crystallizes in the cubic system: NaCl type with a space group (Z = 4). The lattice constant is a = 0.4327 nm, with Ti atoms occupying the origin positions (0,0,0), while C atoms are located at (1/2,1/2,1/2) positions. Ti and C atoms are octahedrally coordinated with each other, resulting in Ti6C octahedra sharing edges (*Hamedi et al., 2011*).

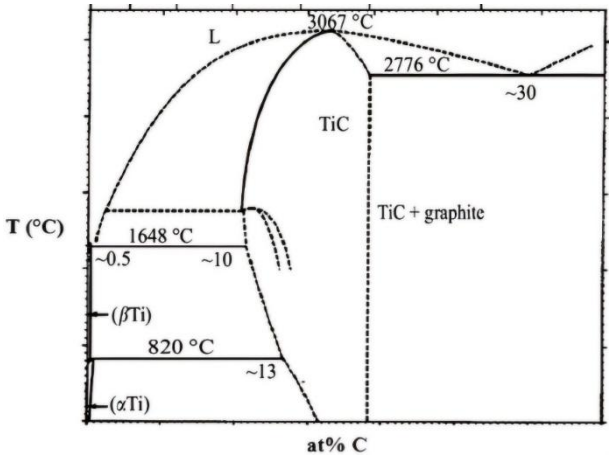


**Figure 9:** Phase diagram of Ti-C system (*Hamedi et al., 2011*).

Carbide deposition commonly achieved by reacting a halide with a hydrocarbon in the presence of hydrogen or nitrogen gas. Noel et al. synthesized TiC thin films using hydrogen gas, titanium tetrachloride ($TiCl_4$), methane ($CH_4$), and acetylene ($C_2H_2$) as source gases (*Noel & Kovar, 2002*). They prepared a thin titanium carbide layer by chemical vapor deposition (CVD) in the $TiCl_4$-$CH_4$ system at temperatures between 850 and 1050°C under a hydrogen atmosphere, with pressures ranging from less than 100 Pa to 1 atm. The resulting product is a hard, wear-resistant coating that forms a chemical bond with the substrate (*Noel & Kovar, 2002*). Azadi investigated the effect of different parameters on the CVD rate of TiC produced from $TiCl_4$-$CH_4$-$H_2$ mixtures. The study found that the deposition rate slightly increases with higher pressure, is directly proportional to the $CH_4$ content, inversely proportional to the equilibrium HCl concentration in the reactor, and almost inversely proportional to the $TiCl_4$ content in the inlet gas when no HCl is added (*Azadi, 2018*).

### 2.2.3 Ti-C-N coatings

The most important zone within the ternary system Ti-C-N for the deposition of hard coatings is the TiN-TiC quasibinary-system. This region delineates the interplay between titanium nitride (TiN) and titanium carbide (TiC), dictating the composition and properties of resulting coatings. The phase diagram of the Ti-C-N system (Figure 10), which as a fundamental guide for the strategic design of TiCN-CVD coatings. TiC shares the same crystal structure as TiN, but exhibits a higher hardness due to a strong covalent bonding. The miscibility occurred among TiN and TiC, where the nitrogen could be substituted and replace by the carbon in fcc structure, resulting in $TiC_xN_{1-x}$ ($0 \leq x \leq 1$) solid solution. This gradual difference in the composition allows

for continuous-adjustment of properties of the coating, as elucidated by (*Bonetti et al., 1990*).

In the contemporary context, two primary deposition processes are employed for $TiC_xN_{1-x}$ coatings on cutting tools, utilizing precursors for TiN deposition such as $TiCl_4$, $N_2$, $H_2$, and Ar. Carbon is introduced through the addition of $CH_4$ during the process, typically carried out between 850 and 1050°C. The carbon content (x) in $TiC_xN_{1-x}$ coatings can be regulated between 0 and 1 by manipulating the partial pressures of $CH_4$ and $N_2$, along with the deposition temperature (*Mayrhofer et al., 2006*). The structure and morphology of $TiC_xN_{1-x}$ coatings are influenced by varying deposition temperature and composition. A model for the structure of $TiC_xN_{1-x}$ coatings has been suggested by Du et al., with the morphology transitioning from rounded hillocks to plate-like structures (Figure 11), and eventually pyramidal crystals as the deposition temperature increased (*Du et al., 2018*).

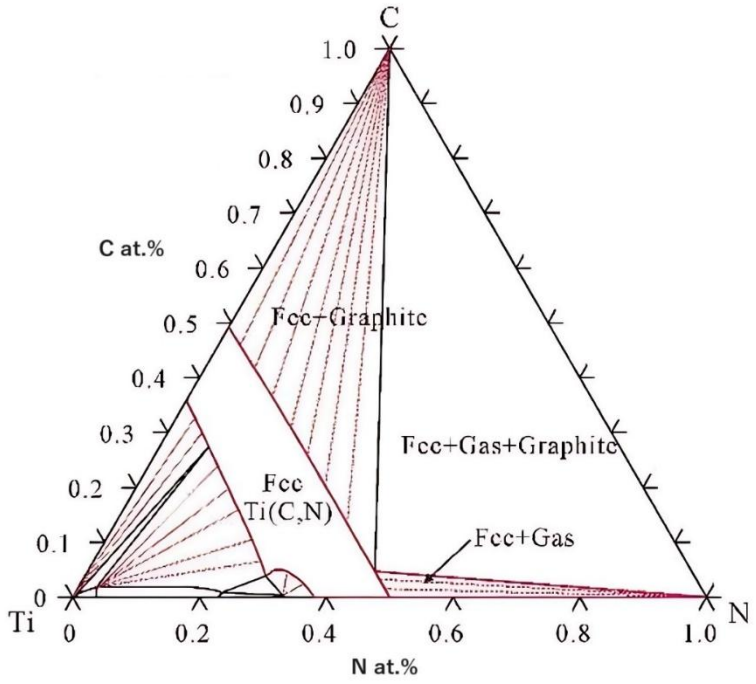


**Figure 10:** Phase diagram of Ti–C–N system (*Du et al., 2018*).

An alternative method for depositing $TiC_xN_{1-x}$ films involves the use of $CH_3CN$ instead of $CH_4$. Deposition temperatures are lower, usually ranging between 800 and 900°C, leading to this process being referred to as MTCVD to emphasize the lower temperatures. Bonetti et al. delineated competing reaction paths for $TiC_xN_{1-x}$ formation

at different temperatures, emphasizing the influence on nitrogen content (*Bonetti et al., 1990*). At 850°C, the reaction occurs by the following equation:

$$6TiCl_4 + 2CH_3CN + 9H_2 \rightarrow 6TiC_{0.67}N_{0.33} + 24HCl \quad (1.5)$$

At lower temperatures, higher N contents can be achieved through the following reaction:

$$4TiCl_4 + 2CH_3CN + 9H_2 \rightarrow 4TiC_{0.5}N_{0.5} + 2CH_4 + 16HCl \quad (1.6)$$

Compared to the use of $CH_4$, the compositional range in MTCVD coatings is limited to a narrow range. MTCVD coatings exhibit a distinct columnar-structure of preferred (211) orientation, while HTCVD coatings include of the equiaxed-grains. The advantages of MTCVD coatings include lower tensile stresses due to reduce the temperatures and reduce the tendencies to decarburization and formation of η-phase (*El Azhari et al., 2020; Larsson & Ruppi, 2002*).

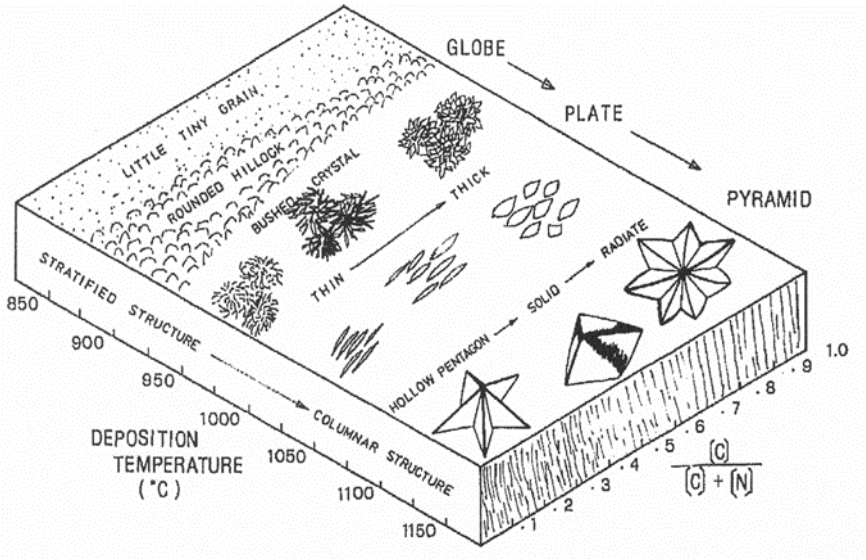


**Figure 11:** Morphological evolution of $TiC_xN_{1-x}$ coatings deposited via $TiCl_4$ –$H_2$ – $N_2$ – $CH_4$ system (*Derakhshandeh et al., 2023*).

### 2.2.4 Ti-Al-N coatings

TiAlN hard coatings demonstrate superior cutting performance as the TiN and TiCN coatings, particularly in applications requiring high-temperature hardness and oxidation resistance (*Derakhshandeh et al., 2023*). Within the ternary Ti–Al–N system, the quasi-binary TiN–AlN system is crucial for CVD coatings, as shown in Figure 12. AlN crystallizes in a hexagonal close-packed (hcp) structure, with categorized as covalent

hard material, while face-centered cubic (fcc) TiN is classified as metallic hard material. The phase diagram for TiN–AlN system illustrates a maximum solubility of AlN in TiN about 5 mol.%, with negligible solubility of TiN in AlN. This limited diffusion can result in atoms remaining in an intermixed supersaturated state upon direct condensation from the vapor phase. At higher AlN concentrations, the hcp structure predominates, while fcc structures form more broadly, and amorphous deposits can occur at low temperatures (*Pal & Deevi, 2003*). Also, the crystal structures of TiN and fcc–$Ti_{1-x}Al_xN$, as illustrated in Figure 13 (a and b), show that Al atoms partially replace Ti atoms, leading to a reduced lattice parameter of the cubic structure. The fcc structure's stability is influenced by the Al content and its distribution within the lattice (*Gao et al., 2008*).

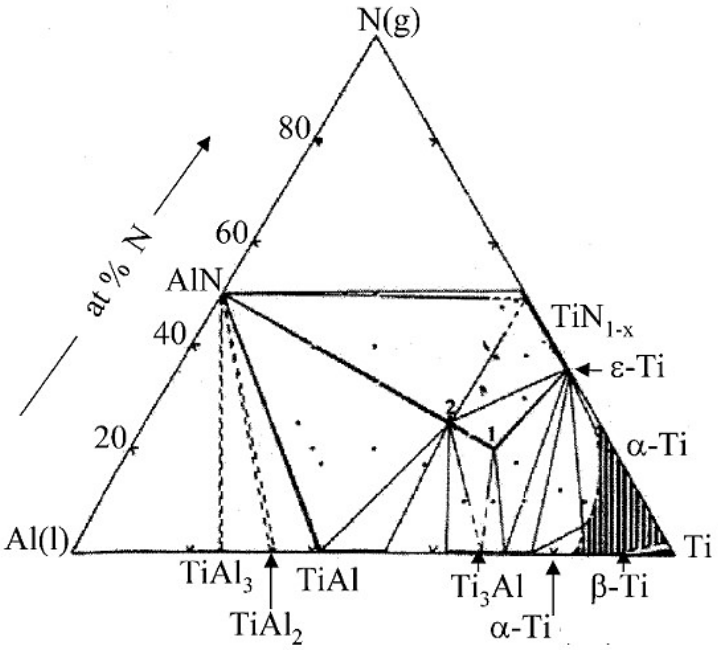


**Figure 12:** The ternary phase diagram of Ti–Al–N system (*Gao et al., 2008*).

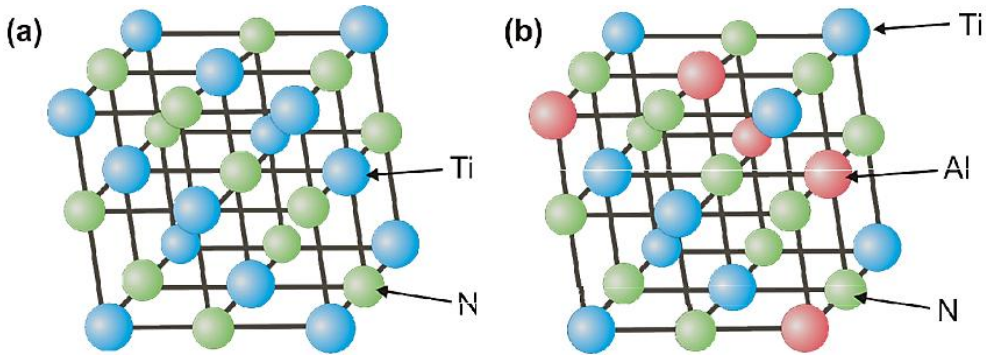


**Figure 13:** Face-centered cubic (FCC) crystal structure for: (a) TiN and (b) fcc–Ti-Al-N (*Patscheider, 2003*).

Usually, the deposition process involves $TiCl_4$, $AlCl_3$, $N_2$, and $H_2$; however, replacing $N_2$ with $NH_3$ is necessary for the formation of the coatings, resulting in fcc–$Ti_{1-x}Al_xN$ coatings with Al content up to 0.90 at temperatures between 700°C and 900°C, and chlorine content below 1.00 at.% (*Gupta & Meletis, 2004*). Alternatively, using metal halides derived from in-situ chlorination of a $Ti_{0.5}Al_{0.5}$ alloy, along with $NH_3$ and $H_2$ at 700°C, produces fcc–$Ti_{1-x}Al_xN$ films up to x ~0.40, with chlorine impurities ranging from 1.00 at.% in Ti-rich films to 12.00 at.% in Al-rich coatings (*Hou et al., 1998*). Madar et al. explored the deposition of $Ti_{1-x}Al_xN$ coatings at 550°C to 650°C, where the cubic structure forms by replacing Ti atoms with Al atoms in the TiN lattice. Higher Al content significantly enhances the coating's mechanical properties and oxidation resistance. (*Madar et al., 2001*). Furthermore, Vogiatzis et al. evaluated TiAlN coatings deposited by CVD for dry machining applications on various materials. The study found TiAlN coatings outperformed other coatings, including CVD TiCN/$Al_2O_3$, on steel and cast iron (*Vogiatzis et al., 2017*). Moreover, Todt examined the oxidation resistance of $Ti_{1-x}Al_xN$ coatings, noting that CVD $Ti_{0.05}Al_{0.95}N$ maintained excellent oxidation resistance up to 1100°C, with minimal degradation (*Todt et al., 2016*).

### 2.3 Properties of CVD hard coatings

This section provides a comprehensive literature survey of the properties and characterization of CVD coatings, including hardness, surface roughness, tribological behavior, mechanisms of friction and wear, adhesion to substrates, and high-temperature oxidation. Additionally, the subsections describe how these properties influence on the performance of CVD-coated components.

#### 2.3.1 Mechanical and surface properties

The mechanical properties of chemical vapor deposition (CVD) coatings, including, the tribology, wear resistance, hardness and adhesion, have undergone extensive study due to their crucial significance across a range of applications like cutting tools, wear-resistant components, and protective coatings. These properties are essential in determining the performance and longevity of coated materials (*Banapurmath et al., 2018*). The following characteristics significantly influence on the behavior and effectiveness of the coatings.

#### 2.3.1.1 Hardness of CVD coatings

For TiN-based CVD coatings, the hardness influenced by chemical composition, grain size, texture, and impurities. Hardness of TiC/TiN coatings can be modified by changing the element composition, such as replacing nitrogen atoms with carbon atoms, increasing the degree of covalent bonds as discussed by other researchers (*Das et al., 2020*). Also, the microhardness of CVD TiCN coatings can be enhanced by controlling the grain size according to the Hall-Petch relation (*Naik & Walley, 2020*):

$$H = H_0 + kd^{-1/2} \tag{1.7}$$

Where, *(H)* is the hardness, *($H_0$)* is the intrinsic hardness of a single crystal, *(k)* is a material constant, and *d* is the grain size. The grain size in coatings can reach down to several nanometers, depending on the deposition technique and the coating material.

The microhardness of CVD coatings, particularly those composed of titanium carbonitride (TiCN), is linked to the coatings' structural characteristics. CVD coatings often exhibit coarse structures, especially at high deposition temperatures, resulting in large columnar growth structures with micron-sized diameters. Grain size can be altered by adjusting deposition parameters such as temperature and concentration of gases. Fine-grained structures, crucial for enhancing microhardness, require lower deposition temperatures and higher supersaturation of reactive gases (*Shanbaraki et al., 2024*). Lowering deposition temperatures and increasing precursor partial pressures can form finer structures, though this may reduce deposition rates and increase impurities from decomposition of $TiCl_4$. Chlorine impurities reduce grain size, but also negatively affect coating hardness. Voids within the coating structure can significantly impact material strength and hardness, as hardness may decrease below bulk values due to the voids (*Abadias et al., 2018*).

A well-defined diamond stylus indents the material at a specific load, and hardness is calculated from the load and indent area. For thin coatings, it is crucial to avoid substrate contribution, with the indent depth not exceeding 1/10 of the coating thickness (*Chowdhury et al., 2005*). The diamond indenter with a three-sided pyramid geometry commonly used, and hardness derived from the plastic deformation depth, subtracting the elastic contribution. Figure 14 shows typical load-displacement curve and related indent cross-section (*Holmberg & Matthews, 2009*).

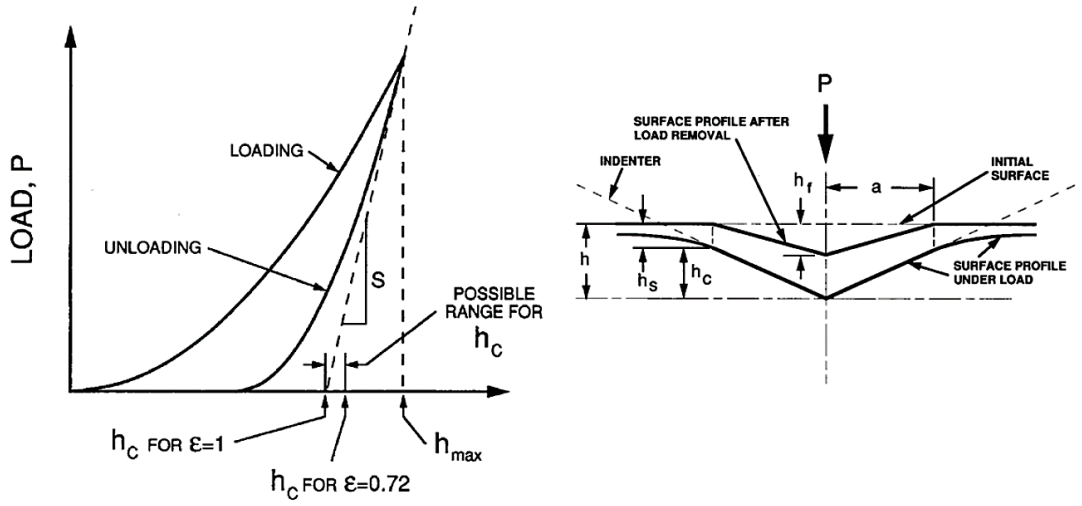


**Figure 14:** Illustration of a standard load-displacement profile and associated indent cross-section during microhardness test, where: P: applied load, $h_{max}$: maximum indentation depth, $h_f$: final indentation depth, S: slope of unloading curve at maximum load, $h_c$: contact depth between the indenter and the material under maximum load, $\epsilon$: a geometric constant that refer to the shape of the indenter (*Holmberg & Matthews, 2009*).

### 2.3.1.2 The surface roughness of CVD coatings

Surface roughness values give information about the texture and irregularities of a surface, often quantified by the presence of peaks and valleys. The surface roughness of chemical vapor deposition TiN based coatings significantly impacts their performance under various operational conditions (*Chen et al., 2024*). Typically, surface roughness characterized using a stylus profilometer, measuring vertical deviation of the profile from the centerline with parameters such as $R_a$, $R_z$, and $R_p$ as shown in Figure 15. $R_a$ (average roughness) is the arithmetic mean of the absolute surface height deviations from the mean line within a specified evaluation length. $R_z$ (average maximum peak to valley) is the average vertical distance between the highest peak and the lowest valley within the measured range. $R_p$ (maximum peak height) is the vertical distance between the highest peak and the mean line within the measuring length. $R_p/R_z$ (peak to valley ratio) measures the proportionality between the maximum peak height and the maximum valley depth (*Holmberg & Matthews, 2009; Das et al., 2021*).

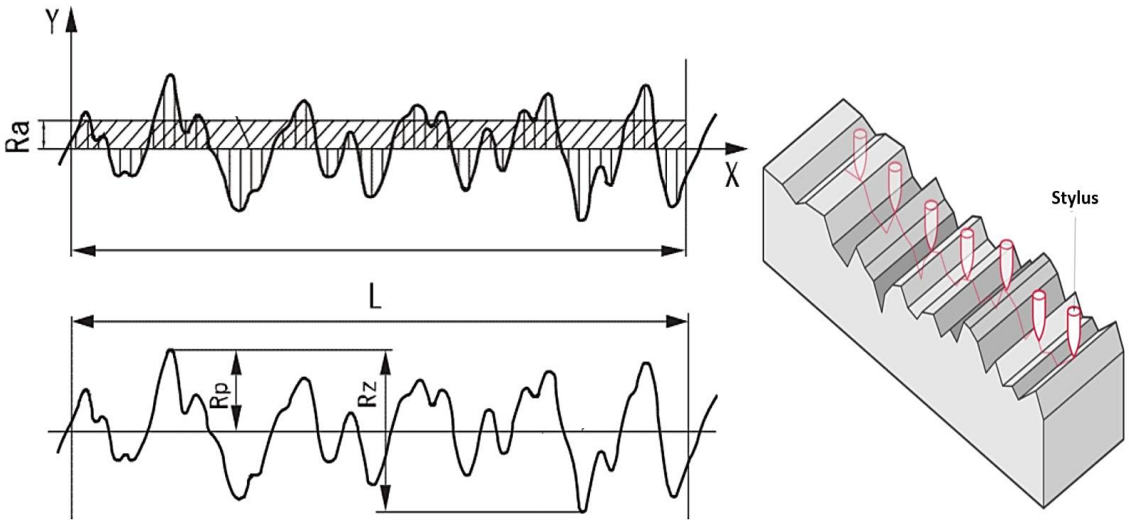


**Figure 15:** Schematics of the parameters of surface roughness (*Wei et al., 2022*).

The roughness of TiN based coatings is influenced by many factors, including deposition parameters, substrate material, post-treatment processes, and environmental conditions. Variations in deposition parameters like temperature, pressure, and precursor chemistry directly affect the growth kinetics and morphology of the coating, impacting its roughness characteristics. For instance, higher deposition temperatures create smoother coatings due to enhanced surface diffusion and reactivity, while lower temperatures may result in rougher surfaces due to incomplete precursor decomposition (*Yunata et al., 2017*). The choice of substrate material significantly affects the roughness of TiCN coatings, with substrate surface morphology, crystal structure, and chemical composition playing crucial roles in influencing nucleation and growth processes during CVD (*Hayward et al., 1992*). Kajikawa discussed the mechanisms causing roughness evolution during CVD, classifying them into two stages: the initial stage of deposition on the substrate and the growth stage of continuous films (*Kajikawa, 2008*). Positive-feedback growth includes shadowing, concentration gradient, and preferential deposition of particles, while non-positive-feedback growth includes the effects of crystallographic planes, crystallinity, composition, and catalytic activities.

### 2.3.2 Chemical, thermal, and structural properties

Chemical vapor deposition (CVD) coatings exhibit a wide range of chemical, thermal, and structural properties that directly impact the performance of CVD-coated components under high-temperature conditions. These properties such as adhesion, cohesion, oxidation resistance, and microstructural evolution are crucial for the

efficiency and durability of CVD coatings in machining and wear-resistant applications (*Zhang et al., 2025*).

#### 2.3.2.1 Adhesion and cohesion characteristics of CVD coatings

Adhesion refers to the ability of a coating to remain attached to its substrate, and inadequate adhesion can result in the loss of the surface's operational functionality. Thus, adhesion is crucial for the performance of CVD coatings as it affects the coating's ability to withstand various stresses and environmental conditions. In the case of hard coatings deposited by thermal CVD on cemented carbide, presence micro–cracks are common. Also, thermal stresses may arise during the heating/cooling period through the machining operation, due to differences in the thermal expansion between the substrate and the coatings, with the low thermal expansion coefficient of cemented carbide about ($\alpha$ = 5.0–6.0 · $10^{-5}$ $K^{-1}$) and TiCN coatings ($\alpha$ = 7.5–9.0 · $10^{-5}$ $K^{-1}$) (*Gissler & Jehn, 1992*).

When using tools with CVD coatings, adhesion strength is most importance. The ability of the coating system to reduce shear stresses at the interface significantly influences adhesion. Cracking due to debonding at the interface depends on local load levels, load directions, resulting stress conditions, strain, and deformation. In the design of coating systems, it is crucial to consider the interaction between the substrate and the coating. Pure adhesion involves the chemical reactivity, i.e., the atomic binding forces, resulting in various interfacial binding forces, as showed in Figure 16. These forces may consist of valence forces, interlocking forces, or both. Interfacial cracks occur when these bonds are broken, a phenomenon described by the term interfacial fracture toughness (*Bull et al., 1988*).

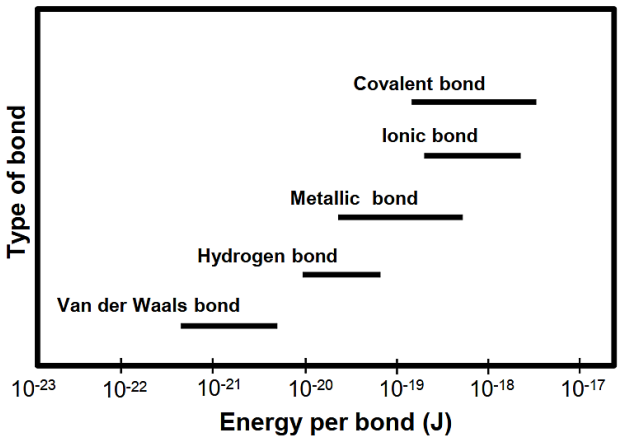


**Figure 16:** Comparison of binding energies across various bondings (*Gissler & Jehn, 1992*).

The adhesion of chemical vapor deposition TiCN coatings is influenced by several factors, as elucidated by recent research (*Stylianou et al., 2020*). Emphasize the importance of clean substrates, free of hydrocarbon or oxide contamination, for promoting strong coating adhesion. This requires thorough cleaning and degreasing of substrates before deposition, with residual impurities and oxide layers effectively removed through chemical reduction using $H_2$ at elevated temperatures. However, impurities within the coating can pose challenges. Chandra et al. highlight that high chlorine concentrations within coatings can negatively impact adhesion, as chlorine atoms tend to diffuse to the coating/substrate boundary over time, leading to corrosion and interface weakening (*Chandra Behera et al., 2023*).

Surface roughening can enhance adhesion by increasing the effective contact area between the roughened surface and the coating (*Peng et al., 2023*). Additionally, high deposition temperatures during thermal CVD promote excellent coating adhesion by facilitating interdiffusion between the coating and substrate, leading to gradual changes in composition and stress distribution (*Yalçin et al., 2024*).

Interfacial reactions between coating elements and the substrate are also critical. (*Shen et al., 2020*) report that diffusion of coating elements into the substrate under high temperature and/or high element content can lead to significant interfacial reactions. Finally, silicon-containing precursors may form silicides with the substrate, while boron can react to form borides, such as CoB and WCoB. Deposition of interlayers like TiN or TiC can mitigate such diffusion (*Wagner et al., 2006*). Therefore, understanding and optimizing the complex factors influencing the adhesion of CVD TiCN coatings, such as substrate cleanliness, surface roughness, deposition parameters, and interfacial reactions, is crucial for achieving robust coating-substrate adhesion and enhancing the performance of coated materials.

#### 2.3.2.2 Oxidation behavior of CVD coatings

The oxidation behavior of TiN based CVD coated significantly affects their performance and longevity. The oxidation process involves the reaction of the coating material with atmospheric oxygen, leading to the formation of surface oxides, as illustrated in Figure 17. Typically, these hard coatings exhibit excellent resistance to mechanical loads, but they may fail at high temperatures and in aggressive

environments. In such cases, chemical inertness becomes more critical than hardness. The oxidation rate increases with temperature, which can rise during machining operations, resulting in a decrease in the coating's mechanical properties and overall performance (Figure 18) (*Weiser et al., 2019*). At elevated temperatures during machining operations, the oxidation process can be divided into two main stages: the formation of oxynitrides ($TiN_xO_y$) and oxycarbides ($TiC_xO_y$) as intermediate steps before the formation of rutile-$TiO_2$. During oxidation, oxygen can infiltrate the layers of the CVD coating by dissolving into interstitial sites, and substituting carbon and nitrogen atoms with oxygen. The primary oxidation products are $TiO_2$ and the release of $CO_2$ and $N_2$. Thus, it is important to study the oxidation properties of these coatings and monitor their oxidation (*Moritz et al., 2023*).

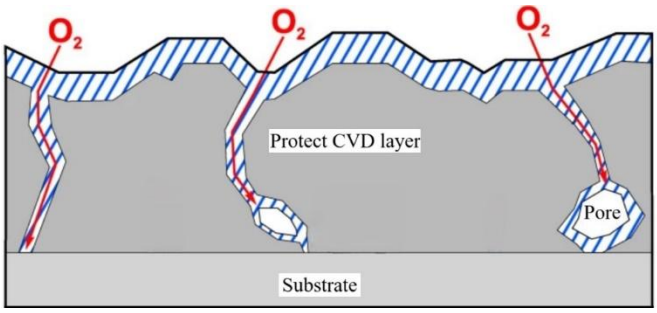


**Figure 17:** Diagram illustrate oxygen penetration through oxidized CVD layers (*Ali & Gyurika, 2024*).

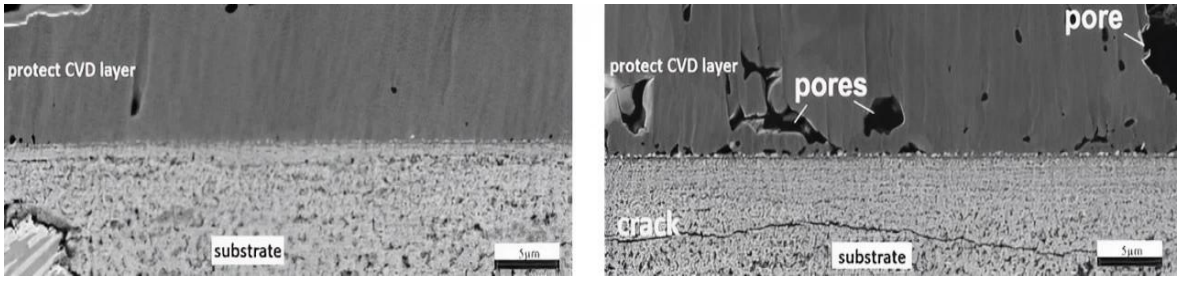


**Figure 18:** Microscopic images of CVD coated sample after 24 hours of oxidation at 800°C in air (*Weiser et al., 2019*).

Oxidation behavior of TiN based CVD coated on cermet carbide substrate at high temperatures has been studied extensively in the literatures. According to Pang's experiment, the oxidation behavior of CVD coated cermet at 500°C to 900°C was elaborated (*Peng et al., 2013*). You's cutting process showed that the local temperature of TiN/TiC coatings prepared by CVD method during the cutting operation was 800°C (*You et al., 2021*). At high temperatures, the failure CVD coatings of the substrate as a

multi-phase component consisting of Co, WC, and Ti (C, N), which reacts with oxygen, generating $WO_3$, $CoWO_4$, and $TiO_2$, as observed by Bagnall et al. and Wang et al. (*Bagnall et al., 2018; Wang et al., 2019*). Many studies, investigated effect of atomic ratio of C and N on the performance of CVD-TiN/TiC coatings. Shi et al. and Ragothuman et al. mentioned that the Ti ($C_{1-x}$, $N_x$)-based cermet (WC-Co) were prepared by three different content ratios of C and N including 5:5, 7:3, and 10:0. The results showed that the variation in the nitrogen content led to the different performances of oxidation resistance and the CVD coating with C/N ratio of 7:3 had the best comprehensive properties (*Shi et al., 2013; Ragothuman et al., 2019*). The size distribution of the individual crystals on the surface was studied by Qian et al. used the line-intercept method. The average grain size of the samples was 0.81, 0.76, 0.70 and 0.72 μm. It was found that the fraction of the fine grains showed a maximum at least N content (*Qian et al., 2022*). Alvaredo studied the grain size distribution and found that the grain size decreased with increasing nitrogen content. Also, the results exhibited that with increase of N content, the thermodynamic stability of Ti(C, N) coatings increases (*Alvaredo et al., 2013*). Zhu et al. found that the oxidation rate of TiN/TiC coatings is always slower than that of Ti(C,N,O). After 600 minutes of oxidation at 600°C, X-ray diffraction (XRD) patterns showed that the oxide layer of TiN/TiC coatings consisted of anatase and rutile $TiO_2$. However, poor interfacial adhesion impaired the oxidation resistance of TiN/TiC coatings, promoting defect formation during cyclic oxidation and leading to accelerated oxidation (*Zhu et al., 2016*). Hsieh et al. also studied the oxidation and wear behavior of Ti-based thin films, finding that TiN/TiC coatings had the highest oxidation resistance, with thermal resistance up to 800°C and 700°C, respectively. The wear rates and friction coefficients of the coatings were also measured, with TiN/TiC coatings having the lowest wear rates (*Hsieh et al., 2006*).

The characterization of coating microstructure has a significant effect on the oxidation and mechanical properties of the TiN/TiC coatings. Fieandt et al. found that the TiCN coatings had nano columnar crystal structure with an elongated columnar crystal structure and had (111) and (200) orientation texture, this microstructure led to enhance the oxidation and tribological performance. Additionally, the study found that the dominant wear mechanisms were oxidation wear, abrasive wear, and adhesive wear (*Von et al., 2018*). Jin et al. and Yang et al. discussed the structure and properties of amorphous $TiO_2$ thin films, which were formed as a result of the oxidation process

applied to TiN and TiC coatings. The authors observed a direct relationship between the oxidation of titanium and various influencing factors, including temperature and duration of oxidation. The results displayed that $TiO_2$ exhibited a combination of anatase and rutile phases. Also, the study appeared that anatase represented a metastable phase of $TiO_2$, characterized by high surface area in comparison to rutile and more reactive. In contrast, rutile emerged as the most stable phase of $TiO_2$, distinguished by a greater density and hardness (*Jing et al., 2022; Yang et al., 2023*). Chen et al. investigated the oxidation behavior of titanium nitride films using X-ray diffraction and field emission scanning electron microscopy, noting the appearance of rutile-$TiO_2$ at temperatures above 600°C (*Chen & Lu, 2005*). Similarly, Chen et al. studied the oxidation behavior of WC–Co hard metal with designed multilayer coatings, showing that the oxidation resistance of WC–Co substrates was markedly improved after deposition of multilayer coatings (*Chen et al., 2012*).

Previous research has demonstrated that, the mechanical properties of TiN based CVD coatings is influenced by varying oxidation conditions. However, there are no studies that focus on monitoring the oxygen content within the thin film layers of coatings during the oxidation process. This gap in the literature is comprehensively addressed in the section 5 (results and discussion). Finally, understanding the oxidation behavior of TiN-based CVD coatings, influenced by factors such as composition, microstructure, temperature, and environmental conditions, is crucial. By comprehending these factors, it is possible to enhance the oxidation resistance of these coatings and extend the service life of coated cutting tools.

#### 2.3.2.3 The microstructure of CVD layers coatings

Coatings are categorized based on their architectural type, which includes the number of layers and how they are arranged, as well as their chemical composition. Their mechanical properties, including hardness, tribological characteristics, and resistance to oxidation, are also key features used for characterization. The microstructure of coatings are frequently examined because they have a significant impact on these mechanical properties. Recent research has focused on modifying the architecture and microstructure of certain CVD coatings to enhance their performance. These coatings can range from the single layer designs to more complex multi-layered

structures (Figure 19). Different coatings with different designs have distinct constructure, chosen to address specific problems (*Sousa & Silva, 2020*).

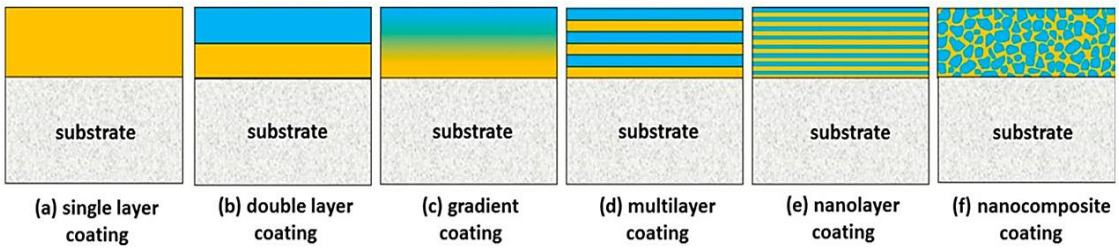


**Figure 19:** Varieties of hard coating designs (*Çalışkan et al., 2017*).

In surface engineering applications, single-layer coatings have long dominated the CVD method. These coatings, typically composed of singular or multi-phases, are cost-effective and widely used in industrial operations, e.g., TiC, TiN, $Al_2O_3$, and $MoS_2$ (Figure 20). However, the development of combined multi-layer coatings has significantly improved substrate properties, particularly in machining tools. Multilayer coatings combine appealing characteristics of each layer, increasing hardness and crack propagation resistance, thus enhancing the performance of cutting tools (*Cheng et al., 2023*).

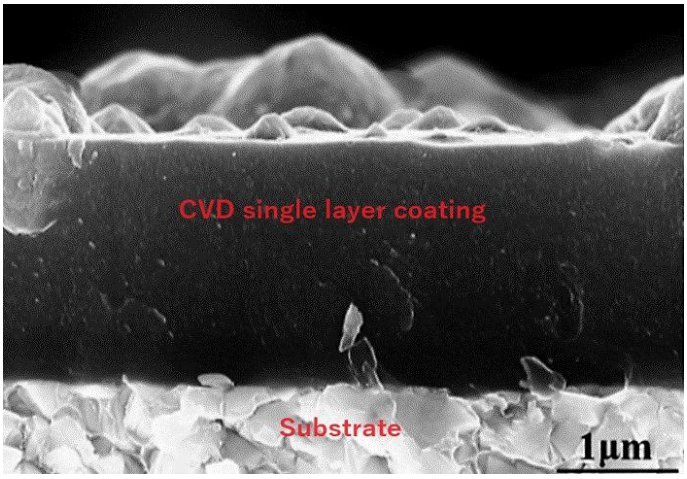


**Figure 20:** Cross-section of single-layer coatings of TiN (*Laikhtman et al., 2009*).

Experimental work by Narasimhan developed hard Ti-C-N coatings with excellent resistance to abrasive wear. These coatings, between 6 to 25 μm thick, showed remarkable improvements in wear resistance when tested on cemented carbide materials (*Narasimhan et al., 1995*). Kainz compared the performance of multi-layered CVD coatings (TiN/TiBN) to single-layered TiN and TiBN, concluding that the multi-layered coating performed better (*Kainz et al., 2019*). Dai studied Ti-based multi-layered coatings with double periodical structures, reporting that this structure can refine the

growth of Ti-based coatings, improving mechanical properties. The authors also noted that residual stresses could enhance coating adhesion and peel resistance (*Dai et al., 2020*).

Multi-layer coatings exhibit specific growth patterns and interactions between different materials. For example, TiC films grow with a (111) orientation on a (001) TiN layer but then change to a (200) orientation. Meanwhile, the TiN layer transitions to a (001) orientation on the (200) TiC. This unique growth behavior allows the formation of multi-layer structures, contributing to the diverse properties of these coatings (*Sousa & Silva, 2020*). Canovic highlighted the significance of $TiN/Al_2O_3$ multilayer films in enhancing mechanical properties and thermal stability, noting that the hardness of these films can reach up to 50 GPa, compared to 15–20 GPa for a single TiN film. However, TiN's susceptibility to oxidation at temperatures above 600°C during cutting operations poses a significant challenge, necessitating protective coatings (*Canovic et al., 2007*).

García et al. conducted a comprehensive study on the microstructure evolution of multi-layered $Ti(C,N)/Al_2O_3$ CVD coatings, which are widely used in machining applications due to their superior wear resistance and thermal stability (*García et al., 2021*). The study's key findings reveal that the multilayered structure of $Al_2O_3$, TiN, and TiCN (Figure 21) exhibits a remarkable resistance to crack propagation during operation. This enhanced resistance is attributed to the alternating layers, which act as barriers to crack expansion, thereby prolonging the service life of the coatings under harsh conditions (*García et al., 2021*). Despite the importance of multilayer coatings for machining applications, there is still a gap in research on the microstructure of TiN/TiC CVD multi-layered coatings.

The thickness variations in individual CVD layers are influenced by deposition conditions such as temperature, pressure, precursor gas flow rates, and deposition time. Non-uniform precursor gas distribution and variations in reaction kinetics can lead to inconsistencies, while substrate morphology, including surface roughness and crystallographic orientation, affects nucleation behavior and coating thickness. Combining several structures and compositions within one coating achieves various individual physical properties, reduces the mismatch in mechanical and chemical properties between the substrate and the coating (enhancing adhesion), controls residual strain and stress within the coatings, stops cracks during severe conditions, and enhances

hardness and/or toughness by allowing layers to slide over each other under load. Mechanisms for toughening layered coatings include (*Choy, 2003; Liu et al., 2021*):

1. Crack splitting at the boundaries of small-sized grains.
2. Crack deflection at the interface between layers.
3. Reduction of stress concentration by interface opening.
4. Plastic deformation at the interface for energy dissipation.

The flexibility and capabilities of CVD techniques have facilitated the development of advanced multi-component coatings, which are extensively employed in various cutting tools.

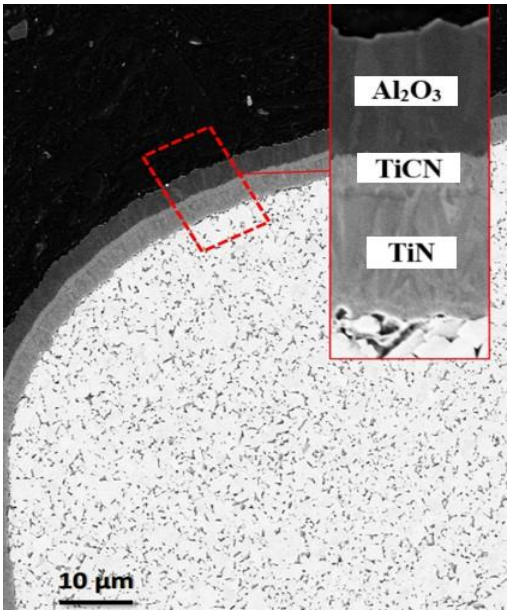


**Figure 21:** SEM image of multi-layered Ti(C,N)/$Al_2O_3$ CVD coatings deposited on WC-Co substrate (*García et al., 2021*).

### 2.3.3 Tribology

Tribology, the science concerning the interaction between solid surfaces in relative motion, is a critical field for understanding and optimizing the performance of CVD-coated cutting tools used in various manufacturing processes. In many applications, achieving low friction values is crucial, as reducing frictional force minimizes energy loss in machine components, thereby improving overall system efficiency (*Tyagi et al., 2019*). Wear, defined as the gradual loss of material due to the relative motion between

two surfaces in contact, causes damage that necessitates the premature replacement of parts, leading to significant costs (*Hutchings & Shipway, 2017*).

Tribological processes are inherently complex and are characterized by specific input and output parameters. Key input data includes the contact geometry at both macroscopic and microscopic scales, the chemical composition and microstructure of the materials, and the environmental conditions. The interaction at the tribological contact induces physical and chemical changes, resulting in energy-related outputs such as friction, wear, and temperature. These processes can be categorized into five distinct types, as shown in Figure 22 (*Rabinowicz, 1995; Hogmark et al., 2000*):

1. **Macro-mechanical changes:** These involve stresses and strains in the contact zone, elastic/plastic deformations, and the dynamics of wear particles.
2. **Micro-mechanical changes:** These include the formation of stresses and strains at the asperity level, crack initiation and propagation, and particle formation.
3. **Tribo-chemical changes:** High local pressures and temperatures favor chemical reactions, altering the chemical composition and mechanical properties of the surface layer.
4. **Material transfer:** This occurs when wear particles re-attach to the surface.
5. **Nano-physical changes:** These are studied to understand friction and wear phenomena at the molecular scale.

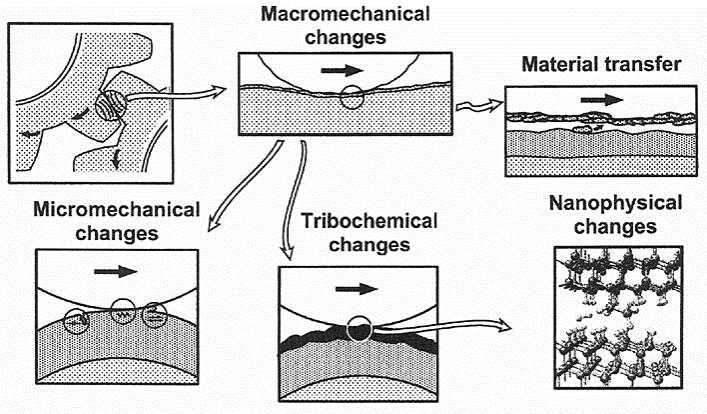


**Figure 22:** Schematic illustration the mechanisms of tribological contact (*Rabinowicz, 1995*).

The application of surface layers presents a viable solution, enabling the tailoring of components with specific tribological properties, such as reduced friction, enhanced wear resistance, or a combination thereof. While the surface layer assumes the

tribological functions, the bulk material can be selected based on different criteria, including stiffness, strength, or cost considerations. Consequently, the application of coatings on tools and machine elements represents an efficient approach to improving the lifetime and productivity of components (*Hogmark et al., 2000*). Cutting tools are subjected to harsh conditions during the operation, which can lead to excessive wear and premature tool failure. To enhance the wear resistance and extend the estimate tool life, various surface coatings have been employed, and among them, titanium nitride (TiN) and titanium carbide (TiC) coatings deposited by chemical vapor deposition (CVD) have gained significant attention. TiN-based coatings known for their excellent tribological properties, including high hardness, wear resistance, and thermal stability (*Kenzhegulov et al., 2022*).

The tribological behavior of TiN based coatings has been studied by many researchers, one of these studies conducted by (*Jen & Jeng, 1994*), they investigated the wear mechanisms of TiN-coated cemented carbide inserts during machining of hardened steel. Their results showed that the TiN coating significantly improved the wear resistance and tool life compared to uncoated tools. However, they also observed the formation of crater wear and coating delamination at higher cutting speeds, indicating the need for further optimization. Another study (*Lim et al., 1999*), evaluated the wear behaviour of CVD TiN coated cemented carbide cutting tool during the turning of AISI 4340 steel. They found that the TiN coating exhibited excellent wear resistance and maintained it stands even after prolonged cutting operations. The authors attributed the superior performance of the TiN coating to its high hardness and resistance to abrasive wear. Further enhance the tribological properties of TiN coatings, researchers have explored the incorporation of additional elements or the formation of multilayer structures. Terek et al. investigated the wear behavior of TiAlN/TiN multilayer coatings deposited on tungsten carbide cutting tools (*Terek et al., 2024*). Their results revealed that the multilayer structure exhibited improved wear resistance compared to single-layer TiN coatings, attributed to the enhanced toughness and resistance to crack propagation. In addition to TiN coatings, TiC coatings have also been extensively studied for their tribological properties in cutting tool applications.

Traditionally, the ball-on-disc method has been utilized to study the wear characteristics and rates of TiN and TiC coatings. Researchers have specifically examined how varying sliding speeds impact the wear rate of TiN coatings, using different linear speeds from

5 to 30 cm/s against both $Al_2O_3$ ceramic balls and steel balls, under loads ranging from 2.5 N to 25 N. This research, conducted by Kim et al. and Aihua et al. also compared the wear performance of TiN and TiC coatings on cermets, which are used as cutting tool inserts (*Kim et al., 2010; Aihua et al., 2012*).

In addition, the wear characteristics of TiN and TiC coatings have been studied at high sliding speeds of approximately 200 cm/s with a normal load of 10 N over a sliding distance of up to 678 m against an SiC ball. Another study assessed the wear behavior of N-rich TiN and C-rich TiC coatings at a sliding speed of 20 cm/s, a normal load of 2.5 N, and a sliding distance of around 1000 m. This was done using a standard ball-on-disc tribometer to compare the tribological properties of TiN and TiC coatings against steel and alumina balls at contact loads between 1 N and 5 N and sliding speeds of 0.1, 0.3, and 0.5 m/s, as reported by (*Yoon et al., 2002*).

These sliding tests, aimed at determining the wear rate, wear behavior, and coefficient of friction of TiN and TiC coatings, typically employ balls made from alumina, silicon carbide, or steel. However, there is a lack of research on the wear behavior of these coatings using zirconia balls ($ZrO_2$) ball. Understanding the friction and wear behaviour of CVD-coated tools is essential for enhance their performance in cutting tools applications. The following sections will discuss the specific context for the information about friction and wear mechanisms for CVD coated tools.

#### 2.3.3.1 The friction

Friction is a fundamental aspect of the tribological behaviour of CVD-coated tools. It is defined as the resistance to movement of a body against another and is of great importance for coated tools used in cutting operations. The Amontons-Coulomb Law, also known as the law of friction, describes the friction coefficient as the relationship between the tangential force $F_T$ (frictional force) and the normal force $F_N$ (load). This law is assumed to be accurate in tribological contacts with ordinary contact pressures and is often referred to as Coulomb friction (*Holmberg & Matthews, 2009*):

$$\mu = F_T / F_N \tag{1.8}$$

During contact, friction is composed of two different components: the adhesive component ($\mu_a$) and the ploughing component ($\mu_p$) (*Holmberg & Matthews, 2009*):

$$\mu = \mu_a + \mu_p \tag{1.9}$$

The adhesive component related to the materials in contact, and it controlled by an adhesive force which acting at the contact areas. The adhesive force originates from the force required to break the inter-surface bonds when the surfaces slide against each other. While, the ploughing component arises from the deformation force acting during the ploughing of the softer material by the surface of the harder material and is related to the surface topography of the contact surfaces. Additionally, wear particles in the interface will act in a ploughing manner (*Engdahl, 2006; Nilsson & Olsson, 2011*).

#### 2.3.3.2 Wear mechanisms

The wear mechanisms that are of particular significance in the context of coatings and metal cutting processes are adhesive wear, abrasive wear, fatigue wear and tribo-chemical wear. It is crucial to note that in most practical scenarios, more than one wear mechanism operates simultaneously, leading to a complex interplay of various wear modes. While there exists an interrelationship between friction and wear, with low friction often associated with reduced wear. There are numerous examples in the literature that demonstrate high wear rates despite low friction conditions (*Holmberg & Matthews, 2009; Weber et al., 2022*). The wear of materials can be broadly categorized into four fundamental mechanisms, each governed by distinct underlying processes and characteristics, as depicted in Figure 23, and as the following (*Jacobson & Hogmark,* 2010*; Rickerby & Matthews, 1991*):

**1. Adhesive wear:** This wear mechanism involves the formation and subsequent fracture of adhesive junctions between the contacting surfaces. When two surfaces are in intimate contact, strong adhesive bonds can form, leading to the transfer of material from one surface to the other. As the surfaces continue to slide relative to each other, these adhesive junctions are subjected to shear forces, resulting in the detachment of material particles or the formation of wear debris.

**2. Abrasive wear:** it occurs when hard particles or asperities on one surface plow or cut into the opposing surface, leading to the removal of material. This wear mechanism is prevalent in situations involving abrasive environments, where hard particles or debris are present between the contacting surfaces, or when one of the surfaces more harder than the other.

**3. Fatigue wear:** it is a result of cyclic loading and unloading of the material, leading to the initiation and propagation of subsurface cracks. Over time, these cracks can propagate to the surface, resulting in the detachment of material particles or the formation of pits or spalls on the surface. This wear mechanism is commonly observed in rolling contact applications, such as bearings and gears.

**4. Corrosive wear:** Chemical wear, also known as tribo-chemical wear, involves chemical reactions between the surfaces and the surrounding environment, often accelerated by the high temperatures and pressures generated during the tribological contact. These reactions can alter the surface chemistry and mechanical properties, leading to the formation of reaction products that can either promote or mitigate wear, depending on their characteristics.

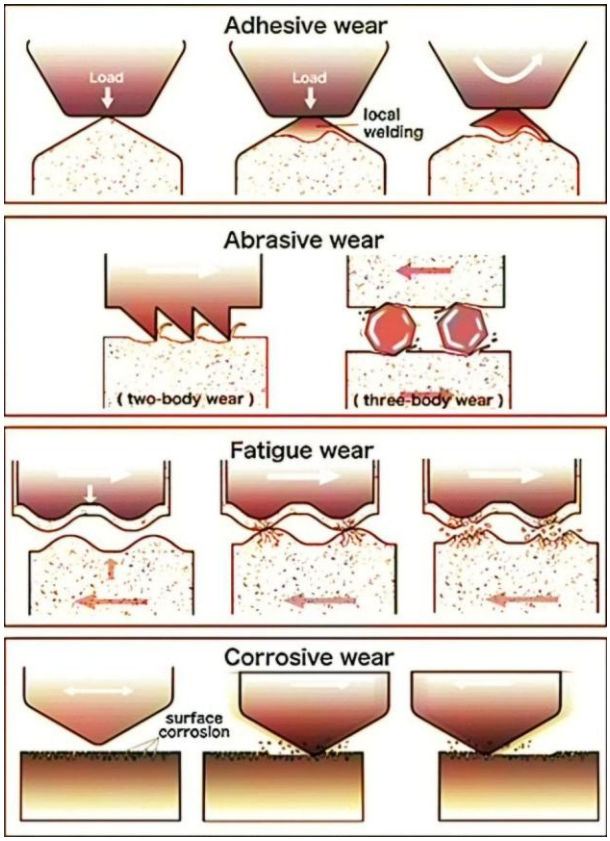


**Figure 23:** Schematic representation of the four basic wear mechanisms (*Tsujimoto et al., 2018*).

In practical applications, wear mechanisms rarely act in isolation; they often interact synergistically, significantly affecting overall wear behavior. For instance, abrasive particles generated during wear can exacerbate adhesive wear by increasing the real area of contact, thereby promoting the formation of adhesive junctions. This interplay not

only intensifies wear but also complicates its prediction and control. Similarly, fatigue wear can be heavily influenced by surface oxides or reaction products formed through tribo-chemical processes. These compounds can alter the material properties and stress distribution, accelerating wear. Understanding these interactions is crucial for designing materials and systems with enhanced durability and performance (*Vasu et al., 2024*).

In the machining operations, the loads on the cutting edge caused by chip formation can reach a fatigue limit, leading to the nucleation of cracks below the surface (Figure 24a). As the load on the cutting-edge increases, these cracks propagate to the cutting-edge surface. The wedge effect of the workpiece material inside the cracks and the traction effect promoted by the adhesion wear mechanism generate a crack network (Figure 24b). Consequently, the cracked regions lose cohesion with the substrate or other coating layers, resulting in delamination. This delamination reduces the bonding strength between the coating layers and between the coating layer and the tool substrate. Subsequently, spalling occurs, exposing the tool substrate (Figure 24c). At this stage, the tool wear mechanism transitions to intense crater wear occurring through diffusion and abrasion, driven by the stronger chemical affinity between the materials. Ultimately, this process leads to the collapse of the cutting edge. So, Understanding the fundamental wear mechanisms and their interrelationships is crucial for developing effective strategies to mitigate wear and enhance the performance and reliability of materials and components in various industrial applications (*Boing et al., 2020*).

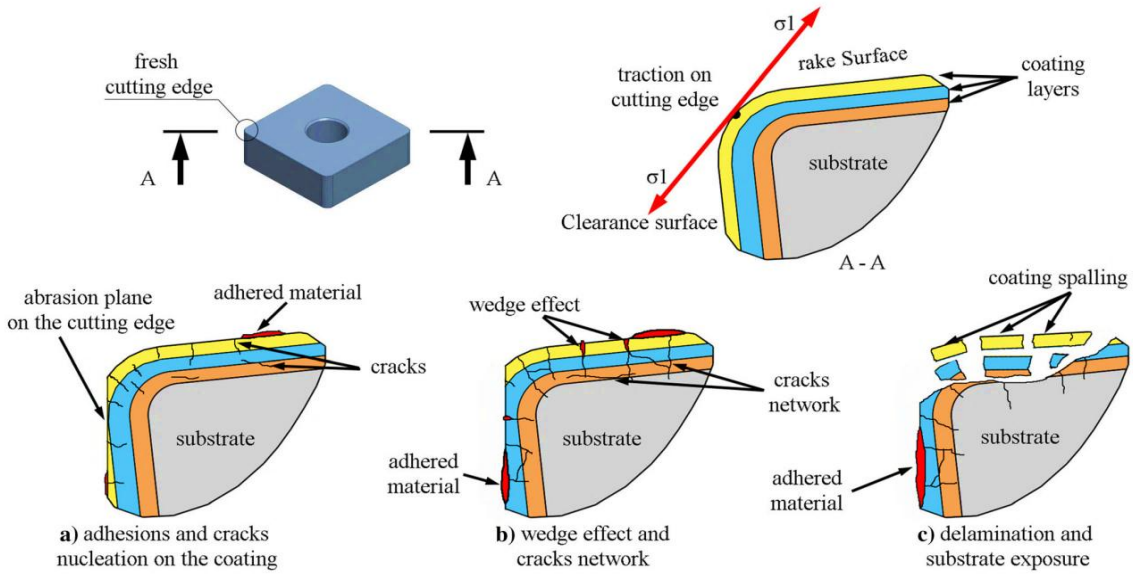


**Figure 24:** Sequence of events leading to the failure of a CVD coated cutting tool (*Boing et al., 2020*).

## 3. Scope and objectives

Figure 25, created by VOSviewer version 1.6.20, presented a visual network map illustrating the relationships between key terminologies in the field of chemical vapor deposition (CVD) coatings, particularly titanium nitride (TiN), titanium carbide (TiC), cermets, morphology, and thin films. The central and prominent node of TiN indicated its importance in the literatures and emphasized its relevance in wear-resistant applications and thermal stability. The term "cermet" was highlighted as a substrate material. The map also showed associations with concepts such as "morphology" and "grain size," which were critical for understanding the structural attributes that influenced coating performance. Moreover, the visualization underscored the significance of "thin film" and "multilayer" of TiCN and $Al_2O_3$, which played a crucial role in extending the lifespan of cutting tools.

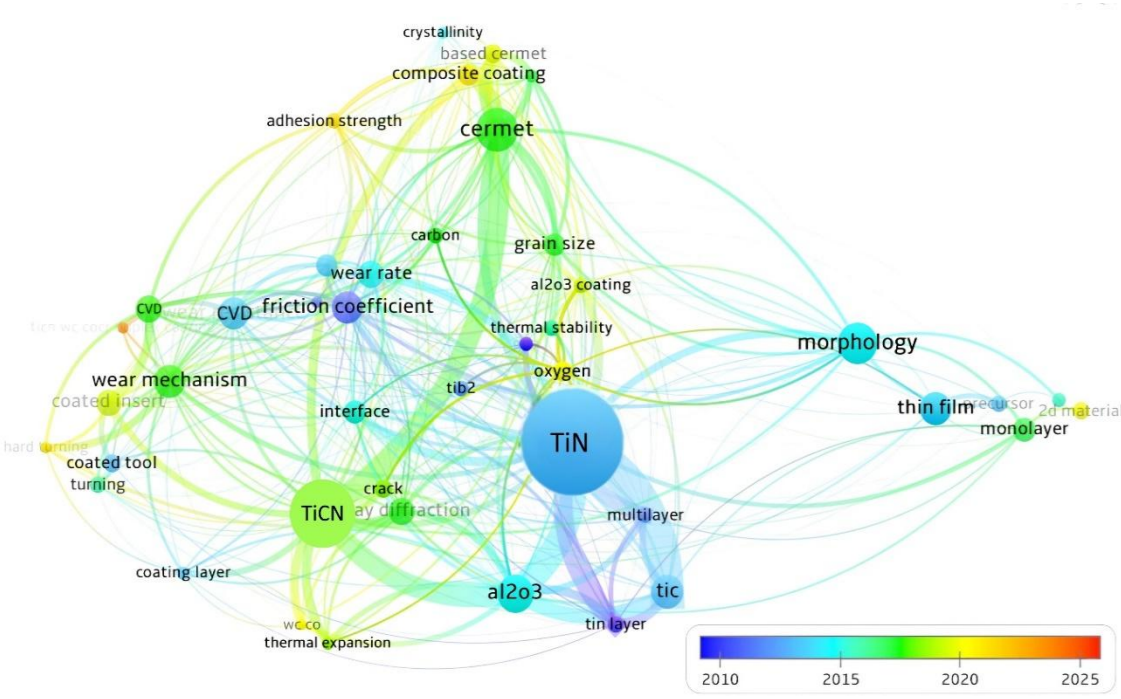


**Figure 25:** Linkage analysis map based on keywords of collected articles.

This dissertation consisted of five main sections, section one presented a general overview of TiN-based coatings, including the theoretical foundations and a literature review relevant to TiN-based CVD coatings, emphasizing their significance in enhancing cutting tool performance. Section two outlined the objectives of the study. Section three provided a detailed description of the methods used to investigate the morphology, characterization, mechanical properties, thermal analyses, and oxidation

behavior of TiN-based CVD coatings. Section four presented the experimental results, including a thorough analysis of the morphological, mechanical, and thermal properties of different TiN-based coatings applied to various substrates. The findings were discussed in depth, covering deposition parameters, number of layers, and coating thickness. Section five summarized the conclusions of the present study.

**Objectives of present study:**

The primary aim of the present study is develop and evaluate the TiN-based CVD coatings that can significantly enhance the performance of cutting tools. The study focuses on the following objectives:

**1. Investigation of mechanical properties:** Assessing the micro-hardness, wear and tribological properties of the CVD coatings.

**2. Characterization of coating structures:** Utilizing advanced techniques such as X-ray diffraction (XRD), scanning electron microscopy (SEM), and energy-dispersive X-ray spectroscopy (EDS) to study the microstructure and composition of the coatings.

**3. Evaluation of oxidation behavior:** Analyzing the oxidation resistance of the coatings at high temperatures to determine their thermal stability and potential for use in the extreme conditions.

**4. Evaluation of coating composition:** Experimenting with different CVD coatings to identify the optimal coating thickness, number of layers, and elemental composition that offer the best performance in terms of durability and resistance to wear and adhesion.

# 4. Experimental

This section outlines the methodologies employed for the comprehensive investigation of the morphology, characterization, mechanical testing, thermal analysis, and oxidation behavior of TiN-based CVD coatings. All tests conducted in this study were performed at the Research Centre of Engineering Sciences, Department of Materials Engineering, University of Pannonia. To enhance readability, images of the equipment used have been included in Appendix-B. By detailing the experimental protocols and instrumentation, this section enables a thorough assessment of the coatings' performance attributes.

## 4.1 Morphological and characterization measurements

Morphological and characterization analyses were conducted to evaluate the structural and elemental properties of the coatings. These analyses are critical for understanding the surface and internal features, providing insights into performance and potential applications.

### 4.1.1. Preparation the samples for measurements

The preparation of samples for scanning electron microscopy and energy-dispersive X-ray spectroscopy involved careful cleaning to ensure optimal imaging quality. Samples were cleaned in an ultrasonic bath containing ethanol and acetone to remove contaminants and enhance resolution for back-scattered electron imaging. Cross-sectional samples were embedded in epoxy resin (NXMET XF40) and polished to achieve a smooth surface, crucial for clear visualization of internal structures. This preparation ensured high-quality images and accurate data, facilitating comprehensive analysis of the CVD coatings.

### 4.1.2 Scanning electron microscopy

SEM and EDS were utilized to investigate the surface morphology, microstructure, and elemental composition of the coatings. The SEM analysis was conducted used a FEI/Thermo Fisher Apreo S scanning electron microscope under high vacuum conditions with an accelerating voltage of 20 kV. SEM utilizes an electron beam with energies between 100 eV and 30 kV, focused on specific points of the sample surface,

causing the emission of various particles. The signals produced by electron-material interactions are detected by different detectors, with the beam moving across the surface to generate a time-varying signal corresponding to the detected signal intensity, producing a grayscale image on the display. Each pixel in the image represents a specific point on the sample.

Depending on the detector used, different material properties can be visualized. Secondary electron (SE) detectors provide surface morphology images, while BSE detectors offer atomic number contrast images. Additionally, EDS detectors allow for local compositional analysis by measured the energy and intensity of characteristic X-rays induced by the electron beam, facilitating both qualitative and quantitative analysis. EDS detectors also enable elemental mapping, determining the composition at each pixel and displaying elements in different colors for visual interpretation. SEM can operate in scanning transmission electron microscopy (STEM) mode to examine samples smaller than 200 nm. This mode, analogous to light microscopy using transmitted light, produces a true magnified image from electrons passing through the sample. The highest resolution achievable with SEM is 1-2 nm (*Jakab, 2023*).

EDS analysis was performed to determine the elemental composition of the coatings used an EDAX AMETEK Octane Elect Plus Energy Dispersive X-ray Analyzer, operating at an accelerating voltage of 20 kV with a data collection time of 180 seconds.

### 4.1.3. Optical microscopy (OM)

Optical light microscopes are the most commonly used instruments for examining the surface microstructure of materials due to their accessibility, ease of use, and the wealth of information they provide. However, traditional light microscopes are limited by their depth of field, which can hinder the detailed analysis of samples with complex topographies. This limitation can be effectively addressed through the use of digital light microscopes. By continuously moving the objective and reconstructing images from sharp image planes, digital light microscopy can achieve high-depth-of-field imaging. This technique allows for the precise examination of surface features and microstructural details that would otherwise be obscured (*Ardebili & Pecht, 2009*).

In this study, optical microscopy (OM) was employed to examine the microstructure and surface features of the CVD-coated samples. The analysis was performed used a

Keyence VHX-2000 digital light microscope, which provides high-resolution images with significant depth of field, allows for detailed observation of the coatings' surface morphology. OM was used in this investigation for several reasons. Firstly, it allowed for the rapid and non-destructive examination of the CVD coatings, providing immediate visual feedback on their quality and uniformity. Secondly, OM served as a complementary technique to scanning electron microscopy (SEM), offering additional insights into the coatings' surface characteristics because OM offers the advantage of viewing the samples in their natural state without the need for extensive sample preparation. Additionally, optical microscopy enables detailed observation of the topographical features, facilitates the identification of surface defects or irregularities, and allows for detection of colour changes in the surface of CVD-coated samples.

### 4.1.4. X-ray diffraction (XRD) measurement

X-ray diffraction (XRD) examinations enable the qualitative and quantitative determination of crystalline phases present in the TiN-based CVD coatings and substrates used in this study. The principle of the method is based on the interference of reflected X-rays, where amplification occurs only in directions where the path length difference of the rays is an integer multiple of the wavelength; in other directions, cancellation is observed.

The measurements were performed using a Philips PW 3710 diffractometer with CuKα radiation (50 kV, 40 mA). The scan rate was set to 0.02° 2θ/s over a range of 10 to 70 degrees 2θ, employing a curved graphite monochromator. Data collection and analysis were facilitated using X'Pert Data Collector software and High Score Plus 5.0 software, respectively. Phase identification and quantitative phase analysis were conducted using the Rietveld method (*Brümmer et al., 1984*), with reference to the 2021 Powder Diffraction Files (PDF-2 2021) from the International Centre for Diffraction Data (ICDD).

## 4.2 Mechanical tests

Mechanical tests were conducted to evaluate the properties of the CVD-coated samples, including microhardness, tribological behavior, adhesion, and surface roughness.

### 4.2.1 Vickers micro-hardness test

Vickers microhardness test is a widely used non-destructive method to determine the hardness of CVD-coated samples. In this study, a diamond pyramid indenter was applied to the sample surface under a predetermined force.

Microhardness was measured for both coated and uncoated (reference) samples by used a Vickers microhardness tester (Wolpert 402 MVD, Fritz Müller GmbH, München, Germany) with a load of 0.2 kgf. The hardness values were averaged from five readings per specimen. The indentation diameter was used to calculate the penetration depth of the diamond pyramid, allowed for the distinction between the hardness of the coating and that of the substrate.

### 4.2.2 Tribological test

The tribological behavior of the coatings was evaluated through dry-sliding experiments conducted by used a TRB3 type tribometer (Anton Paar GmbH, Buchs, Switzerland) in ball-on-disc configuration (Figure 26), based on ASTM standards G99-05 and G133-05. In these tests, the coated samples were evaluated against two different counterface materials: steel, using an Anton Paar 100Cr6 steel ball, and zirconia, using a Fritsch zirconium oxide grinding ball, which complies with the manufacturer's datasheet (composition: $ZrO_2$: ≥ 94.2%, $HfO_2$: ≥ 1.0%, MgO: ≤ 3.5% and other: 1.3%). The diameters of the steel and zirconia balls were 6 mm and 5 mm, respectively. All experiments were conducted at a controlled temperature of 25°C in ambient air with a relative humidity of 46 ± 3%.

The experimental parameters were systematically maintained, with the maximum sliding speed set at 15.71 cm/s, the normal load fixed at 20 N and stroke length about 10mm. Throughout the tests, the coefficient of friction (COF) was continuously recorded in relation to the sliding distance, providing valuable data on the frictional performance of the coatings. After the completion of each test, the wear tracks on the samples were carefully cleaned with alcohol to remove any loose wear debris. Subsequently, wear tracks measured by profilometer to evaluate the extent of wear. Additionally, SEM, EDS, and optical microscopy were used to analyze the wear tracks.

To quantitatively compare the wear resistance of the CVD coatings, the wear volume ($V_P$, $mm^3$) was calculated according to the standards mentioned above, by used the following equations:

$$V_P=(\pi h/6)[3D^2/4 + h^2] \quad (4.1)$$

$$h = R - [R^2 - (D^2/4)^{1/2}] \quad (4.2)$$

Where:

$V_P$: wear volume, or volume loss ($mm^3$).

$h$: height of the removed material from the ball (mm).

$D$: diameter of the wear scar on the ball.

$R$: original ball radius (mm).

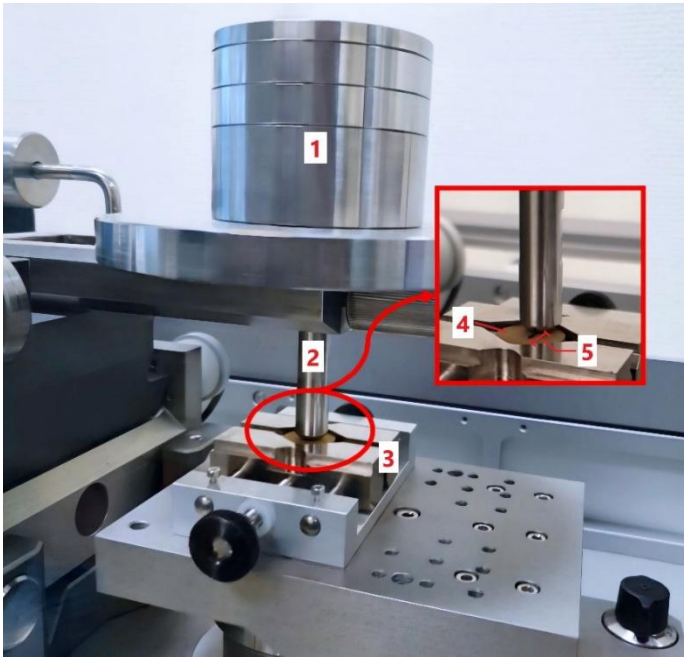


**Figure 26:** Photo of TRB3 tribometer device (ball-on-disk wear test system): (1) loading arrangement (normal force); (2) ball holder; (3) sample holder; (4) coated sample; (5) stroke length (2 strokes = 1 cycle).

### 4.2.3. Surface roughness measurement

Surface roughness measurements were conducted to quantify the surface texture of TiN-based coatings utilized in the present study. The analysis was performed used a Taylor Hobson/AMETEK Surtronic S128 surface profilometer (GmbH, Leicester, England). Surface roughness parameters, including average roughness ($R_a$), root mean square roughness ($R_q$), and maximum peak-to-valley height ($R_z$), were determined to

characterize the topographical features of the coatings. These parameters provide detailed insights into the micro variations in the surface of coated samples.

### 4.2.4. Adhesion test (scratch test)

A modified scratch test was conducted to evaluate the adhesion of the CVD-coated samples (Figure 27). The test was performed by used a TRB3 tribometer (Anton Paar GmbH, Buchs, Switzerland). In contrast to the standard scratch test, where the normal load gradually increased, this modified method applied a constant normal force of 5 N throughout the test. (Different forces (1 N, 2 N, 5 N and 10 N) were initially tested on a CVD-coated sample to determine the optimal load, and 5 N was the most suitable, as will be explained in section 5.6). The stroke length was fixed at 10 mm. The diamond indenter (stylus) marks on the coated surface were examined via a scanning electron microscope to observe coating failures.

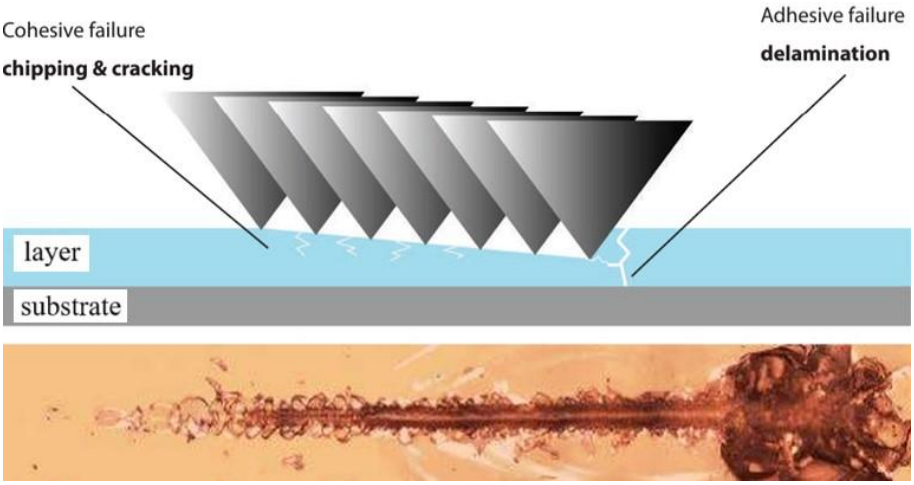


**Figure 27:** Schematic of the scratch test (*Leroux, 2014*).

## 4.3 Thermal analysis measurements

Thermal analysis measurements were carried out to assess the thermal properties of the coatings, including thermal conductivity, temperature distribution during tribological testing, and oxidation behavior.

### 4.3.1 Thermal conductivity measurement

The thermal conductivity of the coated samples was determined by used a CTherm TCi™ device. Measurements were conducted with the heating element set to 150°C,

employed a 3-second heat pulse and a total measurement time of 7 seconds. For each sample, five parallel measurements were performed to ensure accuracy. Distilled water was utilized as the contact agent to facilitate effective thermal transfer during the measurements. This method provided data on the thermal properties of the coatings, which are important for understanding their potential performance under elevated temperatures during machining operations.

### 4.3.2 Thermal camera

A thermal camera (Trotec XC300, Trotec GmbH, Heinsberg, Germany) was used to monitor temperature distribution and capture thermal images of the coated samples during dry-sliding experiments against steel and zirconia balls (Figure 28). Real-time thermal imaging allowed for detailed observation of temperature variations and hotspots on the coating surfaces under frictional conditions.


**Figure 28:** A thermal camera used in the present study.

### 4.3.3 Oxidation tests

The cyclic oxidation experiment was performed under ambient atmospheric conditions. The samples were entered into a specified furnace (Ivoclar Programat P80) after the temperature inside the furnace reached to 800°C (thermal-shock), the procedure of oxidation process was as the following:

- During first five cycles, oxidation time was 2 minutes per a cycle.
- The sixth cycle had an oxidation time of 10 minutes.
- Finally, the seventh cycle was 20 minutes.

The cumulative duration of the oxidation process was 40 minutes. Post-cooling, the oxygen content of the samples determined by used energy-dispersive X-ray spectroscopy (EDS) after every single oxidation cycle. Also, the elemental composition changes for every element of the oxidized surface samples was measured. The thermal shock in this study aimed to model the thermal effects in the cutting tool coated via CVD method during machining operations such as turning or drilling steel workpieces. In these severe operational scenarios, temperatures at the coated tool can rapidly reach about 600-800°C within seconds (*Pang et al., 2022*). Therefore, the test specimens were placed in a preheated furnace at 800°C and removed them after specific periods, which called oxidation time. This approach allowed to model the effect of temperature on the microstructure, composition, and mechanical properties of the tools.

# 5. Results and discussion

This section presents the comprehensive analysis of microstructural characteristics, elemental composition, and performance evaluation of titanium nitride-based coatings prepared by chemical vapor deposition. Samples of the present study fabricated under varying conditions to compare their surface morphology, microhardness, surface roughness, thermal conductivity, tribological and oxidation behaviours. Detailed assessments were conducted to understand the influence of deposition parameters on coating properties, such as layer thickness, crystal structure, and elemental composition. Subsequent tests, including oxidation tests and tribological evaluations, provided insights into the performance of these coatings under different conditions. The findings elucidate the critical role of deposition parameters in determining the efficacy and durability of CVD coatings in the industrial applications.

## 5.1 Materials used

All samples presented in the study were produced by Büttner Ltd. (Nagyatád, Hungary) in a newly developed reactor located at their site. Tungsten carbide-cobalt composite and alloy steel were used as substrates for the coatings.

The process involved the use of precursors such as titanium tetrachloride ($TiCl_4$), nitrogen ($N_2$), hydrogen ($H_2$), and argon (Ar). Table 2 details the manufacturing parameters for bilayer TiN/TiC CVD-coated samples. These samples were categorized into two groups: sample A and sample B. For sample A, the conditions included a lower temperature and double the pressure relative to sample B. The flow rate of precursor gases was kept nearly constant in standard liters per minute (SLM), and the TiC layer was deposited under the same parameters for both samples.

**Table 2:** Manufacturing parameters for bilayer TiN/TiC CVD-coated samples.

| Samples | Layers | Time (h) | Temperature (°C) | Pressure (mbar) | SLM $H_2$ | SLM $CH_4$ | SLM $N_2$ | SLM $TCl_4$ |
|---|---|---|---|---|---|---|---|---|
| **A** | **TiN** | 3.00 | 980 | 100 | 4.10 | | 4.10 | 8.20 |
| | **TiC** | 2.00 | 1000 | 80 | 9.24 | 1.00 | | 8.22 |
| **B** | **TiN** | 3.00 | 1020 | 50 | 3.50 | | 4.50 | 8.00 |
| | **TiC** | 2.00 | 1000 | 80 | 9.24 | 1.00 | | 8.22 |

### 5.2. The characteristics of bilayer TiN/TiC coatings

The microstructure of the coatings on identical substrates is displayed in Figure 29. The image highlighted in red features backscattered electron images from cross-sectional polished samples, where the layer thickness was assessed. On the surface of sample A (Figure 29a), TiN appears in a more crystallized form, while sample B (Figure 29b) predominantly exhibits rounded shapes. The pronounced crystals in sample A may be significant for tribological applications, as they have the potential to remove material from the surface of the counterpart more effectively.

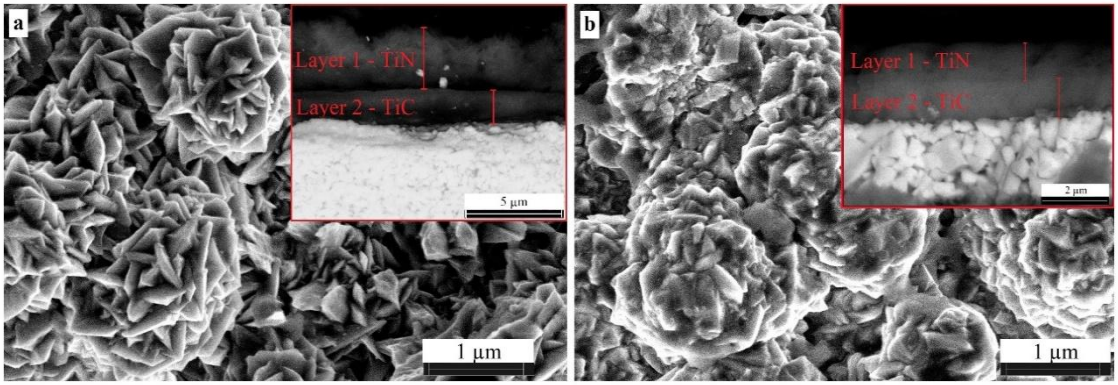


**Figure 29:** Surface morphology and cross-sectional images of the coated samples: (a) sample A; (b) sample B.

The thicknesses of the different layers are summarized in Table 3. The values shown in the table are based on the results of five parallel measurements. In both samples, the thickness of the TiC layer formed is nearly identical. However, for sample A, the thickness of the top layer is twice that of sample B. This difference is likely due to the pressure applied during the process, which may explain the presence of a several sharp crystals on the surface of sample A, in greater thickness.

**Table 3.** Coating thickness of TiN/TiC CVD-coated samples.

| Layers thickness (µm) | TiC | TiN | Total |
|---|---|---|---|
| **A** | 1.64 | 3.19 | 4.83 |
| **B** | 1.32 | 1.55 | 2.87 |

The elemental composition of the different coatings is summarized in Table 4. Measurements were conducted on cross-sectional samples. The composition of the titanium-based coatings is nearly stoichiometric, with the Ti and Ti ratios being approximately 1:1 in each case.

**Table 4.** The elemental composition (at.%) of the substrate and TiN/TiC CVD-coated samples.

| Sample | | Ti | N | C | W | Co |
|---|---|---|---|---|---|---|
| **Substrate** | | - | - | 55.59 | 35.76 | 8.66 |
| **A** | Layer 1 | 51.68 | 48.32 | - | - | - |
| | Layer 2 | 52.32 | - | 45.63 | - | 2.05 |
| **B** | Layer 1 | 45.07 | 54.93 | - | - | - |
| | Layer 2 | 55.84 | - | 44.16 | - | - |

Figure 30 illustrates the phase composition of the substrate and the coatings formed on it. Characteristic reflections of tungsten carbide and cobalt are visible on the substrate. For sample B, the reflections from the deposited coating are also present but with much lower intensity compared to sample A. As observed in SEM, the TiN coating on sample A is in a more crystallized form, with its characteristic reflections being significantly more intense.

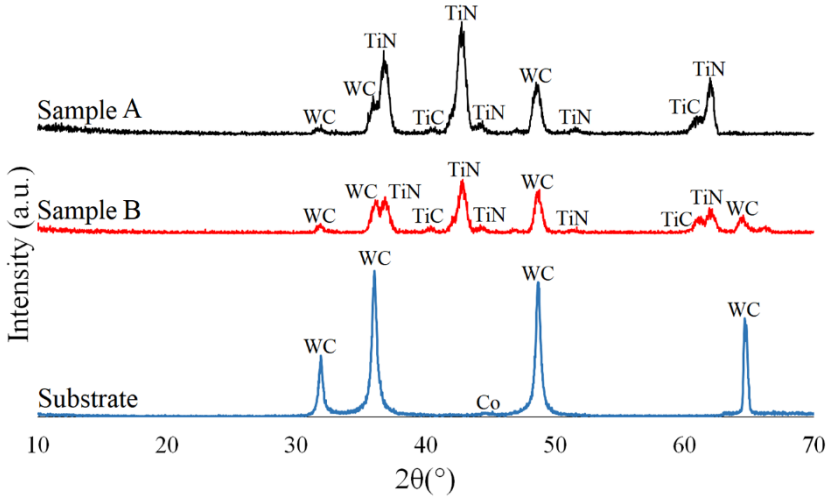


**Figure 30:** Phase composition of the substrate and coated samples.

### 5.3. Vickers-hardness analysis of bilayer TiN/TiC coatings

The microhardness test is a widely recognized method for assessing the mechanical properties of hard CVD coatings. Vickers hardness is a key attribute that influences the wear resistance and lifespan of cutting tools. In Table 5, the Vickers hardness test results are presented for both coated and uncoated samples. It is evident that the coated sample exhibits a significantly higher hardness value compared to the uncoated sample. This enhancement in hardness is attributed to the CVD technique, which is specifically designed to improve the hardness of the coating layer. The increase in hardness (HV0.2) from 1895 to over 2461 underscores the efficacy of the CVD process in enhancing the

mechanical properties of the coating layer. It is also noteworthy that the hardness values of the coated samples are affected by the manufacturing conditions, particularly the pressure and temperature, as detailed in Table 2. Variations in these conditions result in different hardness values between the samples, with higher deposition temperatures and pressures yielding harder coatings. This occurs because elevated temperatures and pressures facilitate more vigorous and effective reactions among the precursor gases, resulting in denser and more robustly bonded coatings. Figure 31 presents a cross-sectional schematic illustrating the penetration depth calculation during the hardness test of the bilayer TiN/TiC coatings.

**Table 5.** Vickers microhardness measurements of the bilayer TiN/TiC CVD-coated samples and the underlying substrate.

| **HV0.2** | **sample A** | **sample B** | **substrate** |
|---|---|---|---|
| **AV** | 2461 | 2158 | 1895 |
| **SD** | 327 | 313 | 79 |
| **PD** (μm) | 5.24 | 5.58 | 5.94 |

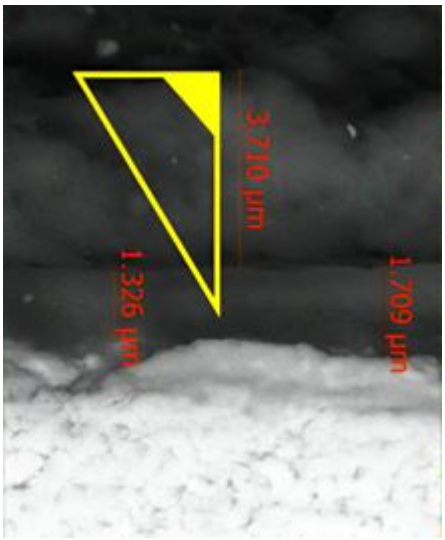


**Figure 31:** Cross-sectional schematic illustrating the calculation of penetration depth during the microhardness test.

### 5.4. Tribological analysis of bilayer TiN/TiC coatings

Figure 32 presents the influence of sliding duration on the friction coefficient of CVD-coated samples against steel and zirconia balls. The charts reveal similar initial behavior against the steel ball, characterized by a slight rise in the friction coefficient due to

interaction between the CVD-coated surface and the steel ball. This is followed by a stabilization of the friction coefficient, attributed to the adherence and accumulation of steel on the sample surface, as verified by SEM analyses showing high levels of iron and carbon. The friction coefficients reach a steady state, as indicated by the blue lines in Figures 31a and 32c. For sample A, the friction coefficient stabilizes at around 20 seconds, whereas for sample B, it takes about 60 seconds. This variation is linked to the more crystallized and sharply grained coating of sample A, which erodes the steel ball quicker than sample B's coating. Additionally, sample A exhibited a higher hardness value than sample B. The adhesion of steel to sample A after 20 seconds is depicted in Figure 32e.

Also, this study investigated the tribological behavior of these CVD-coated samples against zirconia balls, comparing it to their performance against steel balls. Initial observations showed a different friction coefficient behavior over time with zirconia balls, typically lower as demonstrated in Figure 32b. However, as sliding continued, the friction coefficient marginally rose due to the non-adherent detached particles creating an abrasive interaction between the surfaces, leading to surface wear. The coefficient first increased and then significantly dropped, as illustrated in Figure 32d. This pattern is linked to the lesser adhesion and reduced coating thickness on sample B, leading to the complete wear-off of the TiN coating after about 2500 seconds (marked by a green line where the coating detached). As the zirconia ball also experienced wear, the interaction eventually occurred between smoother surfaces, resulting in the lowest friction coefficient ($\mu \approx 0.10$). Figure 32f displays the secondary electron image of sample B's polished surface, highlighting the worn-off coating and the exposed polished WC-Co substrate.

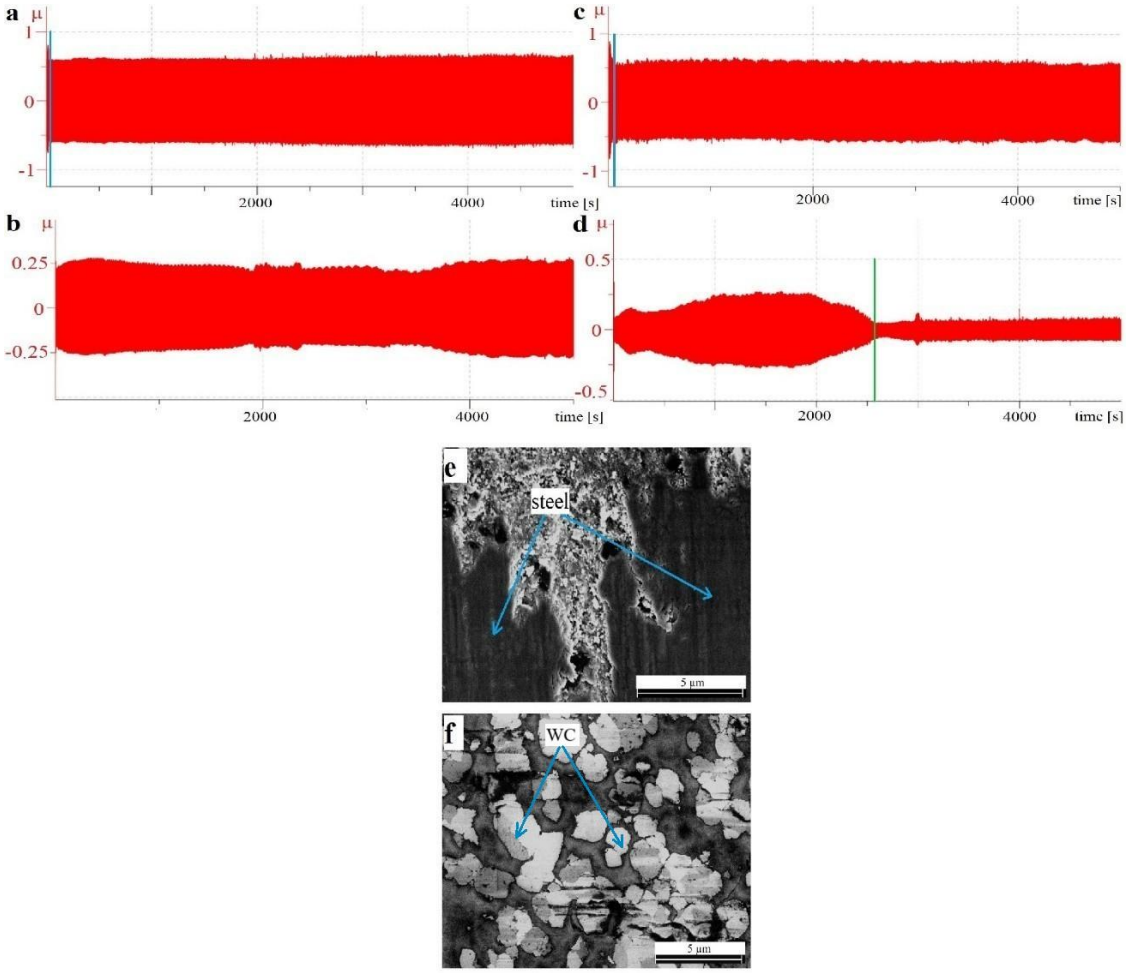


**Figure 32:** Illustrates the changes in the coefficient of friction over time for different samples and ball combinations: (a) sample A versus steel ball; (b) sample A against a $ZrO_2$ (zirconia) static partner; (c) sample B versus steel ball; (d) sample B against zirconia, and the surface morphology of sample A after tribological test against steel ball (e) and against zirconia (f).

These results are crucial as they shed light on how the type of ball affects the tribological performance of coated CVD samples. The reduction in the friction coefficient with zirconia balls can be linked to the distinct properties of the balls used. The observed minor increase in friction might result from the development of wear lines and surface roughening, which are typical during sliding wear tests. The stability in the friction coefficient's average values post-operation phase indicates that the TiN/TiC CVD-coated samples managed to endure the sliding conditions with minimal degradation.

Additionally, it is significant that the frictional heat generated between the CVD-coated samples and the zirconia ball is considerably lower compared to that with the steel ball. Figure 33, which shows the temperature profiles of the CVD-coated samples captured

by an infrared camera during the dry sliding tests, underscores the benefits of using zirconia balls, as they produce less heat during these tests.

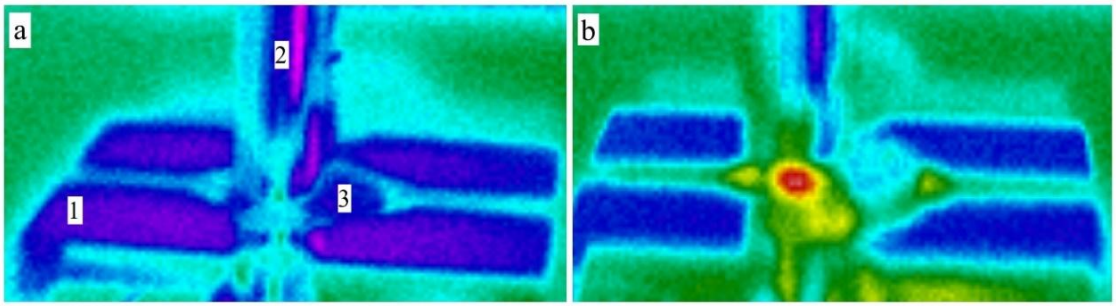


**Figure 33:** Displays the temperature profiles of CVD-coated specimens during dry sliding tests, as captured by an infrared camera: (a) against a zirconia ball, and (b) against a steel ball. The figure annotations include 'number 1' marking the sample holder, while 'number 2' and 'number 3' indicate the static partner and the sample, respectively.

Table 6 summarizes the outcomes of dry sliding tests on CVD-coated samples utilizing steel and zirconia balls, after covering a sliding distance of 500 m. The results reveal that the wear values for steel balls with sample A and sample B are approximately $6.07 \cdot 10^7$ $\mu m^3$ and $5.02 \cdot 10^7$ $\mu m^3$, respectively. Conversely, the wear volumes for samples using zirconia balls are considerably less, at $1.42 \cdot 10^5$ $\mu m^3$ and $2.04 \cdot 10^5$ $\mu m^3$, respectively. This notable decrease in wear volume loss when using zirconia versus steel balls is attributed to the superior hardness of zirconia. Furthermore, SEM analysis shows that zirconia balls do not adhere to the sample surface, which leads to reduced friction and heat during the tests.

The disparity in wear-volume loss among the coated samples can be traced back to variations in preparation parameters, such as pressure and temperature, as detailed in Table 1. The hardness of sample B is 14% greater than that of sample A, as indicated in Table 4, and the thickness of sample B's coating layers is about 68% thicker than those of sample A. These factors collectively contribute to a lower wear rate for sample B, which is about 21% less than sample A with steel balls, and 43% less with zirconia balls. These findings are crucial for understanding the tribological behavior of CVD-coated samples and suggest that zirconia balls may be preferable for such tests due to their high hardness and non-adhesive properties, enhancing the accuracy and reliability of the results.

**Table 6.** Volume loss of the steel and zirconia balls after the sliding test.

| Sample | D (μm) | h (μm) | $V_P$ (μm$^3$) |
|---|---|---|---|
| **Sample A against steel** | 1648.00 | 56.85 | $6.07 \cdot 10^7$ |
| **Sample A against $ZrO_2$** | 397.00 | 3.28 | $2.04 \cdot 10^5$ |
| **Sample B against steel** | 1572.00 | 51.67 | $5.02 \cdot 10^7$ |
| **Sample B against $ZrO_2$** | 362.00 | 2.73 | $1.42 \cdot 10^5$ |

### 5.5. Surface morphology and roughness analysis

The current study examines the tribological behavior of bilayer TiN/TiC CVD-coated samples when subjected to tests using both steel and zirconia balls, complemented by microstructural and compositional analyses through EDS. Figures 34 and 35 show the EDS line scan results after tribological testing over a 500 m sliding distance, where the y-axis displays the atomic percentage distribution and the x-axis represents distance. The element analysis conducted along a red line depicted in Figures 34 and 35, using backscattered electron imaging. Prior to EDS testing, steel particles adhered to the coating surface were removed using an 18 vol.% hydrochloric acid solution, and samples were cleaned in an ultrasonic bath with ethanol.

The line scan for sample A, depicted in Figure 34a, shows the presence of C, Ti, and N in the coating, indicated by pink, yellow, and green colors respectively. Wear traces begin at 400 μm and extend to 800 μm, with the coating still intact and no exposure of the substrate (W) observed. The results indicate a reduction in Ti and N along the wear path, while C content increases, suggesting that the top TiN layer was worn away during the 500 m tribotest. A similar pattern is noted in the zirconium oxide test of sample A, displayed in Figure 34b, where only a narrow section of the top layer shows wear around the 600 μm mark. The findings affirm the excellent wear resistance of sample A against both steel and zirconia.

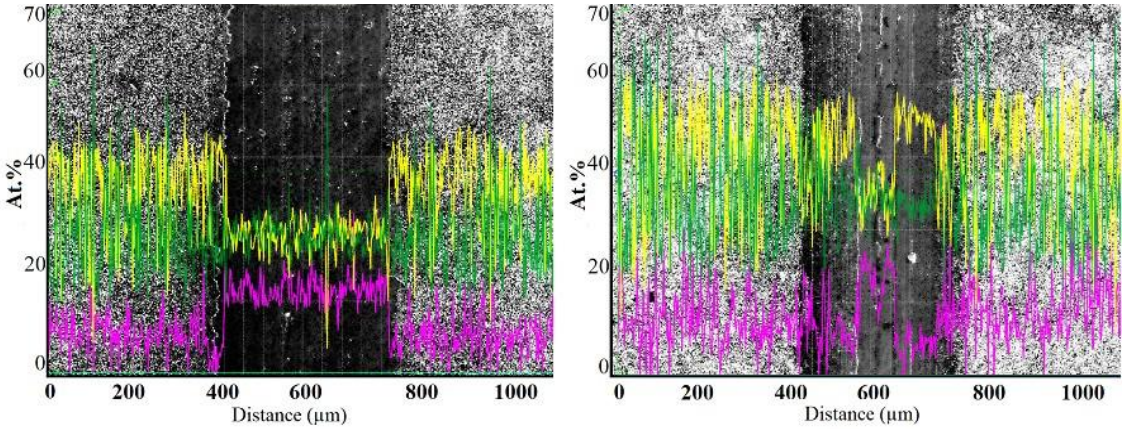


**Figure 34:** Elemental distribution along the wear track: (a) sample A tested against steel; (b) sample A tested against zirconia, with Ti marked in yellow, N in green, and C in pink.

Notably, the noise in Figure 34 indicates minimal wear, as seen in Figure 34b, where a slight fluctuation in carbon content at 600 µm suggests the TiN coating detached within a narrow 50 µm width. In contrast, greater wear in other sample results in a smoother, less noisy image (Figure 34a).

The wear characteristics of sample B were analyzed during tribological tests using steel and zirconia balls, as depicted in Figure 35a and Figure 35b. In the test involving a steel counterpart, the TiN and TiC layers of sample B completely detached from the substrate at approximately 300 µm of sliding distance. This flake-like detachment suggests that the adhesion between the steel deposited on the coated layer and the layer itself was stronger than that between the TiC coating and the substrate. Along the wear track, the atomic percentage of tungsten (W) in the substrate was close to 50%.

In the test with the zirconium counterpart, the TiN layer of sample B almost completely detached, while the TiC layer only partially detached from the surface. These observations are corroborated by changes in the friction coefficient, as illustrated in Figures 32b and 32f. At a sliding distance of 400-600 µm, the presence of the substrate is indicated by the blue color.

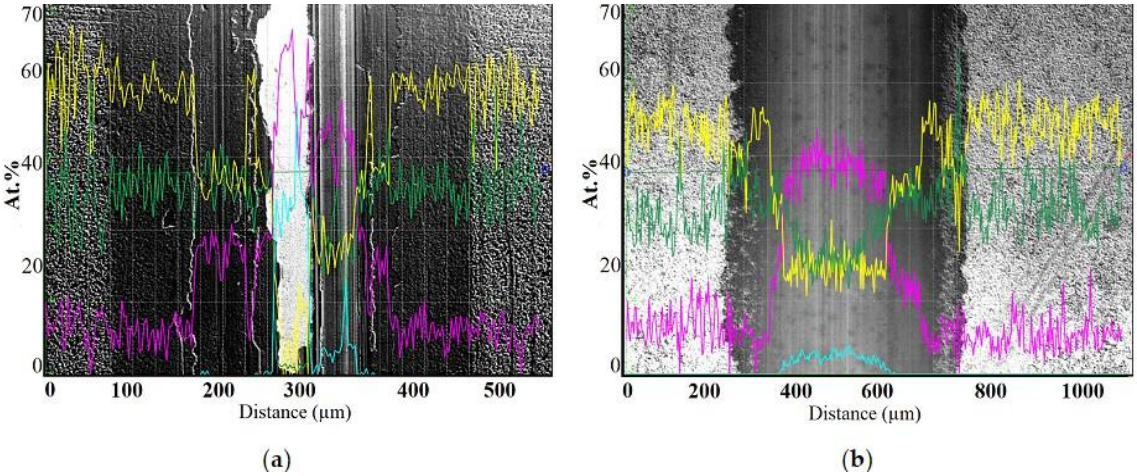


**Figure 35:** Elemental distribution after the sliding test: (a) sample B against steel; (b) sample B against $ZrO_2$, with Ti marked in yellow, N in green, C in pink, and W in blue.

In the case of sample A, where the TiC coating remained intact during a 500 m tribological test, a longer 1550 m test was conducted using a zirconium static counterpart. The volume loss values measured at various distances 50 m, 150 m, 350 m, 750 m, and 1550 m are detailed in Figure 36. The results show that a significant amount of zirconium detached from the ball's contact surface following the 50 m test, a result of the TiN layer being composed of numerous small crystals with sharp edges. The wear amount decreased sharply up to 750 m, then saw a slight increase from 750 to 1550 m. By this stage, the partial detachment of the TiC coating may have begun, and the abrasive wear processes involving the particles on the contact surface continued to wear down the zirconium ball.

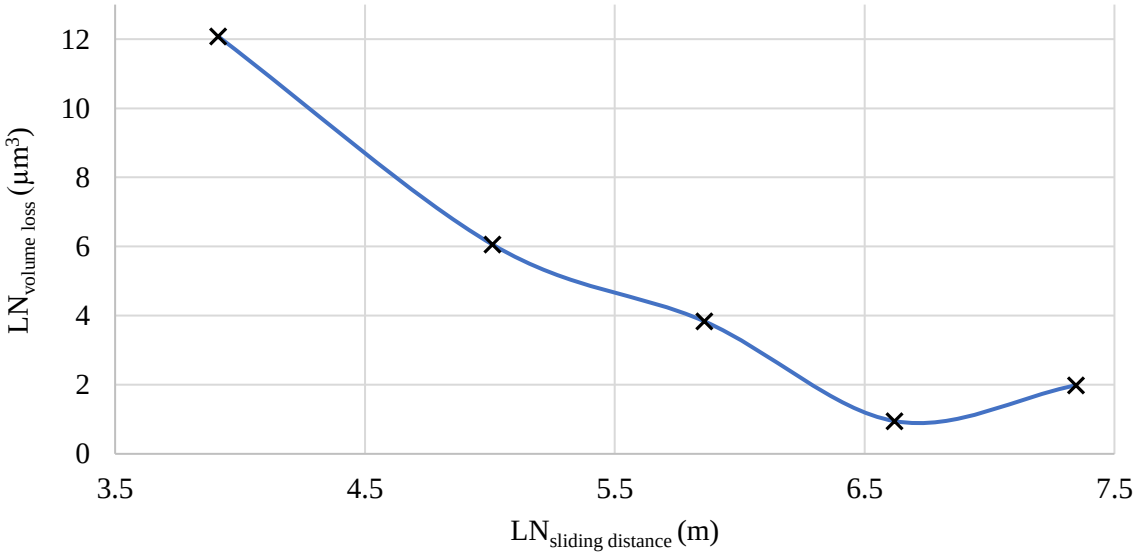


**Figure 36:** Wear rate of the zirconia ball plotted as a function of sliding distance**.**

After the 1550 m wear test, the results of the line scan analysis are displayed in Figure 37. The wear track can be observed between 200 µm and 1000 µm. In the region around 800 µm, both the TiN and TiC layers were completely removed from the surface, as evidenced by the presence of the blue color representing tungsten (W).

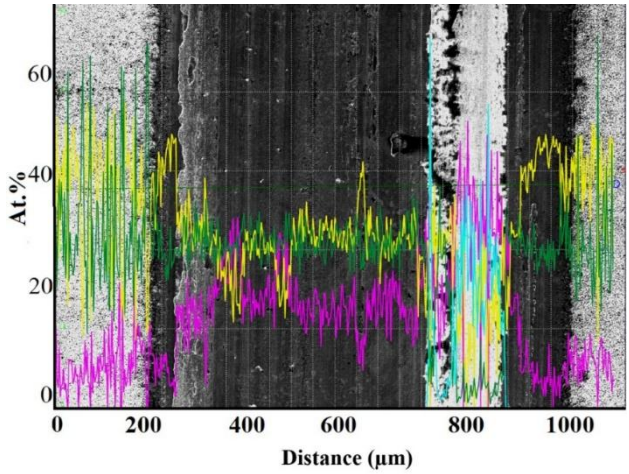


**Figure 37:** Elemental distribution along the wear track of sample A after a 1550 m sliding test, with Ti marked in yellow, N in green, C in pink, and W in blue.

Surface roughness is a crucial factor that influences the tribological properties of CVD coatings, such as their wear resistance and friction coefficient. The data in Table 7 offer valuable insights into the effects of using steel and zirconia balls on the tribological testing of CVD-coated samples. For samples A and B, the average surface roughness increased after the wear tests. Specifically, sample A showed a slight rise in roughness, particularly after tests with the zirconium counterpart, indicating that small, hard particles from the zirconium created deeper grooves despite the TiC coating remaining attached to the substrate. In contrast, sample B exhibited higher roughness values after testing with the steel counterpart, likely due to the coating peeling off in a flake-like manner. The initial $R_p/R_z$ values of each sample were below 0.50, signifying a tribologically favorable surface; these values increased following the wear tests, indicating rougher surfaces characterized by more pronounced peaks.

Moreover, Table 7 reveals that the surface roughness of sample A against zirconia increased to 0.73 after a sliding distance of 1550 m. These findings suggest a direct relationship between sliding distance and surface roughness, implying that the TiN and TiC coatings did not delaminate uniformly across the surface. The original surface roughness measurement data, included all recorded values, are provided in Appendix C.

**Table 7.** Changes in surface roughness values following wear tests.

| Sample | Ra | Rz | Rp | Rp/Rz |
|---|---|---|---|---|
| **Sample A** | 0.19 | 1.74 | 0.84 | 0.48 |
| **Sample B** | 0.15 | 1.65 | 0.81 | 0.49 |
| **Sample A against steel** | 0.29 | 2.41 | 1.23 | 0.51 |
| **Sample A against $ZrO_2$** | 0.42 | 2.58 | 1.37 | 0.53 |
| **Sample B against steel** | 0.40 | 2.55 | 1.28 | 0.50 |
| **Sample B against $ZrO_2$** | 0.35 | 3.06 | 1.57 | 0.51 |
| **Sample A against $ZrO_2$ after 1550 m** | 0.73 | 4.57 | 2.39 | 0.52 |

### 5.6. Adhesion test of bilayer TiN/TiC coatings

The scratch test is a widely used and standardized method for evaluate the scratch resistance and adhesion strength of CVD-coated samples. In this test, a diamond stylus drawn across on the coating surface under a normal load, continuing until coating failure occurs. In this study, 5 N load was selected after extensive trials with loads of 1 N, 2 N, 5 N, and 10 N, as illustrated in Figure 38. The tests were performed of CVD-coated samples consisting of TiN/$Al_2O_3$/TiC layers on a cermet substrate, for determine the optimal load for reliable evaluation.

SEM images in Figures 38(a) and 38(b) showed that, the 1 N and 2 N loads were insufficient to penetrate the CVD coatings, as the substrate remained unexposed. In contrast, Figure 38(c) showed that, the 5 N load fully penetrated of the coating layers, revealed the cermet substrate. Figure 38(d) demonstrated that, the 10 N load removed the coating layers, exposed the substrate more aggressively. So, the 5 N load was more appropriate for this test. Additionally, Figure 39 presented the chemical analysis by used EDS, where (N) represented in yellow, indicated of TiN layer; (Al), shown in red, corresponded to $Al_2O_3$ layer; (C), depicted in purple, represented TiC layer; and (W), shown in blue, confirmed exposure of the substrate.

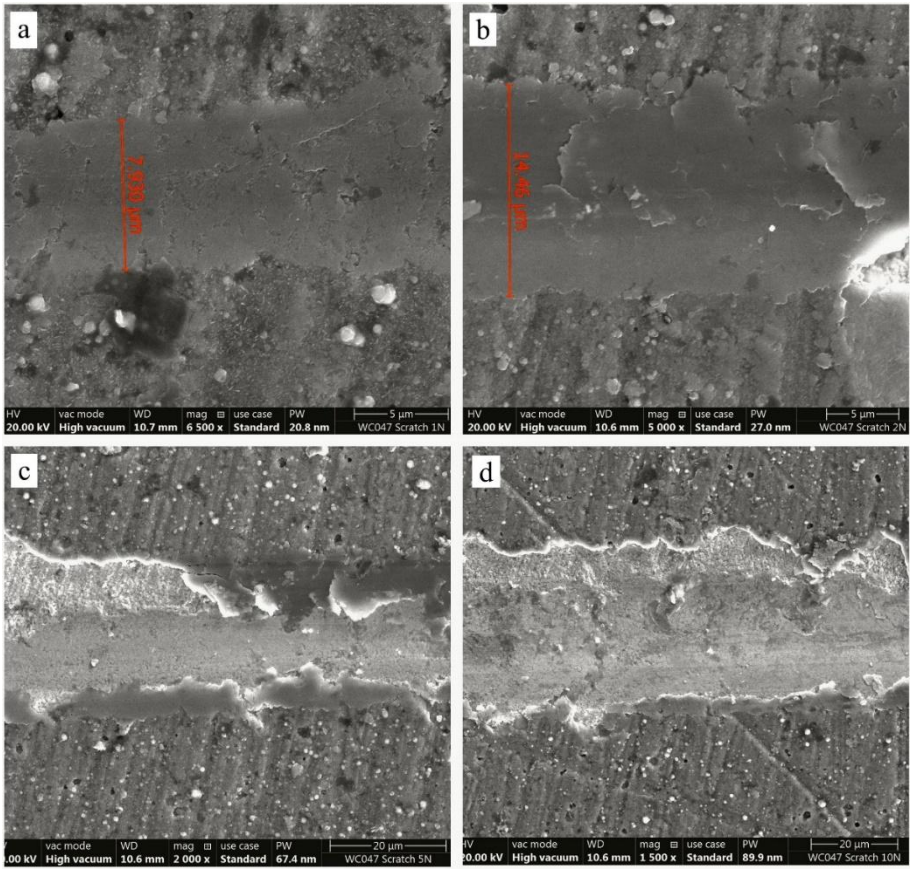


**Figure 38:** SEM images of CVD-coated samples after the adhesion test: (a-b) show partial penetration under 1 N and 2 N loads, respectively; (c) complete penetration under a 5 N load; and (d) extensive penetration under a 10 N load.

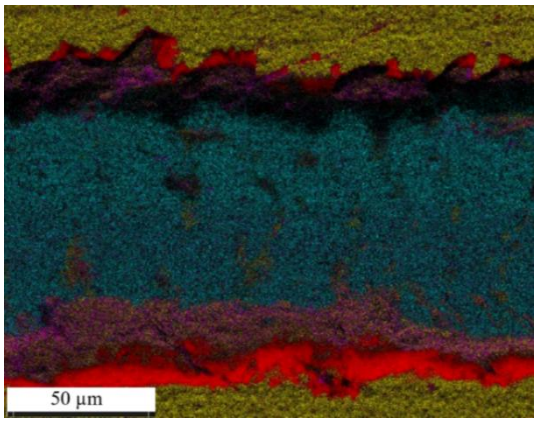


**Figure 39:** Elemental map of the scratched regions, where yellow: N; red: Al; purple: C; and blue: W.

Also, the study analyzed the scratch channel areas of CVD-coated samples during the scratch indentation test, with results illustrated in Figure 40. These images depict the progression of the scratch for both coated samples A and B, focusing on the presence or

absence of micro-cracks, spallation, or delamination. Figure 40(a) highlights the superior performance of sample A regarding adhesion strength and scratch resistance. The irregular shape of the scratch mark and the lack of fine cracks indicate a strong bond between the coating layer and the substrate. Conversely, Figure 40(b) shows the scratch channel of sample B during the test, where the coating smeared rather than detached cleanly, suggesting weaker adhesion to the substrate. This smearing indicates that the diamond stylus easily penetrated and moved across the coating layers, reflecting lower scratch resistance and adhesion strength in sample B compared to sample A. This disparity is attributed to the different manufacturing conditions noted in Table 2. Additionally, the coating layers on sample A are characterized by greater hardness, increased thickness, and enhanced wear resistance, all contributing to its notably better performance.

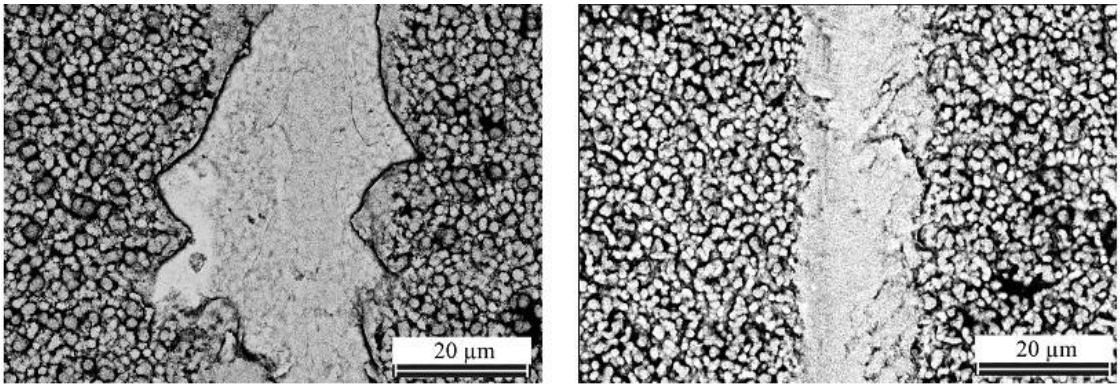


**Figure 40:** Pressure channel formed after the scratch test: (a) sample A; (b) sample B.

### 5.7. The effect of high-temperature heat shock on the composition of CVD coatings

A novel approach was employed to investigate the oxidation characteristics of CVD TiN/TiC coating layers. Due to the minimal thickness of these layers, ranging from 1.3 to 3.2 μm, accurately measuring changes in the mass of the coatings before and after oxidation cycles using conventional scales is challenging. Therefore, EDS was applied to measure the atomic percentage of oxygen in the coated samples before and after the oxidation tests, as well as to evaluate the atomic percentage of other constituent elements (C, N, Ti). This method is more accurate than measuring changes in mass, as it specifically focuses on measuring the oxidation in the coatings and excludes the possible of oxidation in the substrate.

Figure 41 illustrates the variations in the elemental composition (in atomic percentage) of oxygen (O), titanium (Ti), carbon (C), and nitrogen (N) over the oxidation time of sample A at a constant temperature of 800°C. The average standard deviation (SD) values for O, Ti, N, and C are 0.28, 0.12, 0.20, and 0.29, respectively. During the initial cycle (oxidation time of 2 min), the oxygen content increased from 25.54 to 53.30 at.% due to its interactions with titanium, leading to the formation of titanium dioxide (rutile, $TiO_2$). Concurrently, the carbon content decreased from 17.10 to 3.51 at.% due to its interactions with oxygen, resulting in the formation of gaseous CO and $CO_2$. This observation is in good agreement with the findings of Zhu et al., who investigated the oxidation behavior of Ti(C,N) and reported comparable interactions between titanium and oxygen under oxidation conditions. Their study further highlighted the generation of gaseous by-products, which contributed to the increased formation of cracks on the surface of the CVD-coated samples (*Zhu et al., 2016*). Additionally, the nitrogen content decreased from around 27.62 to 14.84 at.% as a consequence of oxygen interacting with titanium, releasing nitrogen atoms which subsequently combined to form gaseous nitrogen ($N_2$). This behaviour persisted throughout all subsequent oxidation cycles. In the final cycle, the oxygen content increased to 68.82 at.%, accompanied by a decrease in carbon content to 3.90 at.% after 40 min, while nitrogen progressively diminished, reaching 0.00 at.% after only 20 min of oxidation. This indicates the complete transformation of the hard-TiN coating layer into titanium oxide, resulting in the collapse of the structural integrity of the initial coating layer. Notably, the oxidation behaviour of the titanium element remained relatively constant, exhibiting a slight decrease from 29.83 to 26.20 at.% when comparing the pre- and post-oxidation states.

The oxidation behaviour of sample B exhibited behaviour nearly identical to that of sample A, as illustrated in Figure 42. The average SD values were 0.92, 0.37, 0.66, and 0.46 for oxygen (O), titanium (Ti), nitrogen (N), and carbon (C), respectively. During the oxidation test, the oxygen content increased to 68.70 at.%, while the atomic percentages of carbon (C) and titanium (Ti) decreased to 4.94 at.% and 24.65 at.%, respectively. Additionally, Figure 40 indicated that by the end of the sixth cycle, the nitrogen content was depleted, indicating the complete conversion of the entire TiN layer into titanium dioxide.

Finally, it is observed from Figure 41. and Figure 42 that the atomic percentage content of all elements, particularly oxygen, has stabilized. This suggests that the oxidation

activity has ceased and reached a steady state after 40 min of the oxidation test for both CVD coated samples. It is also important to mention that the TiN/TiC coating showed good oxidation resistance compared to other similar coatings in the literature. For instance, Koller reported significant increases in oxygen levels and the production of a thick, porous oxide layer exceeding 1 µm, with complete nitrogen depletion in bilayer TiAlN/TaAlN coatings (*Koller et al., 2014*). Fan et al. observed that, the oxidation resistance of single TiAlN coating with 3 µm was considerably poorer compared to bilayer Ti-based coatings (*Fan et al., 2024*). Danek improved the oxidation resistance of the TiAlN coating by adding Cr, but this resulted in a significant decrease in hardness to less than 17 GPa for the TiAlCrN coating (*Danek et al., 2017*). Rovere reported a decrease in oxidation resistance and a significant increase in mass gain during the initial stages of the oxidation test for the CrAlN coating (*Rovere et al., 2008*). Finally, Bouzakis et al. observed a significant decrease in adhesion strength and tool life for the TiSiN coating with increasing temperatures (*Bouzakis et al., 2009*).

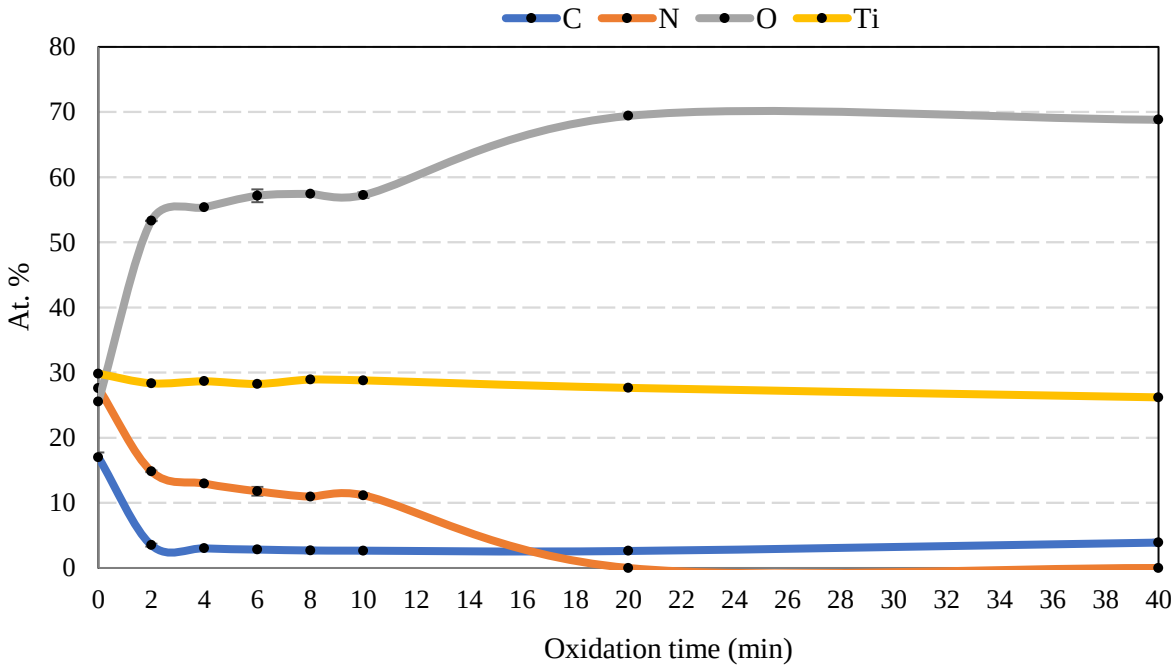


**Figure 41:** Changes in the elemental composition (At. %) of oxygen (O), titanium (Ti), carbon (C), and nitrogen (N) with the oxidation time of sample A during the oxidation test.

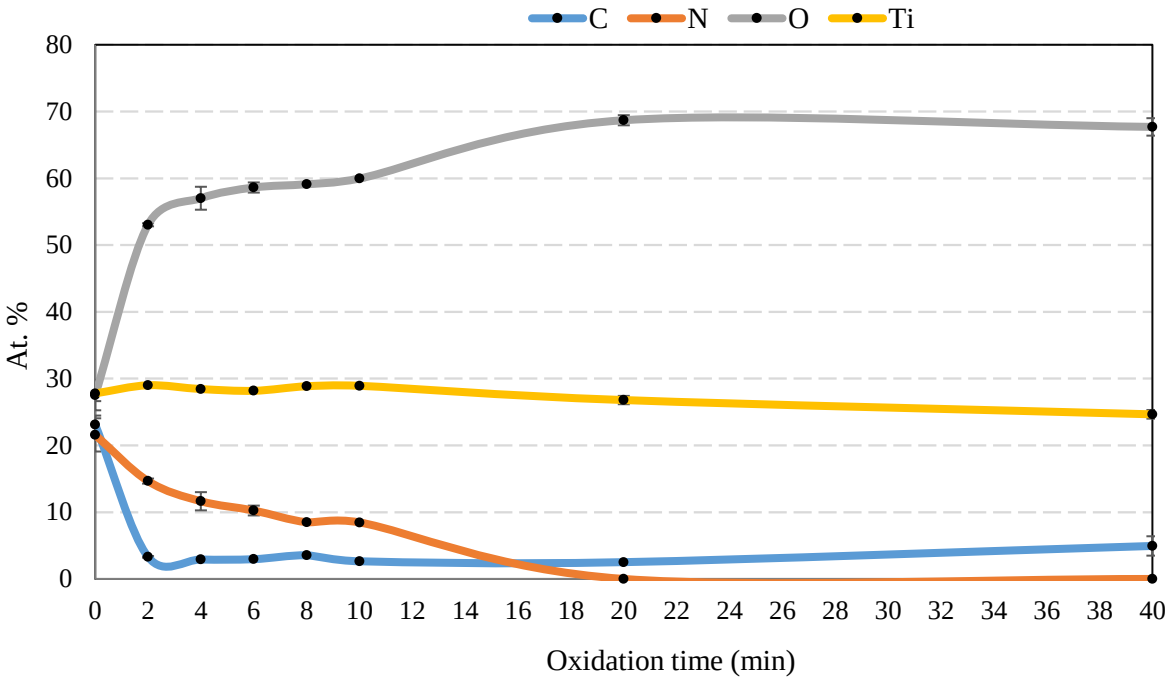


**Figure 42:** Changes in the elemental composition (At. %) of oxygen (O), titanium (Ti), carbon (C), and nitrogen (N) with the oxidation time of sample B during the oxidation test.

### 5.8. X-ray diffraction analysis of oxidized coatings

Figure 43 summarizes the diffractograms obtained during X-ray diffraction phase composition measurement. The substrate marked in blue shows the reflections of tungsten carbide grains (JCPDS: 01-085-4359). The phase compositions of sample A and B are represented by dark green and darker yellow colours, respectively, before oxidative corrosion testing. In addition to the substrate material (WC), the characteristic reflection peaks of titanium nitride (JCPDS: 01-074-8388) and titanium carbide (JCPDS: 01-071-6256) also appear in these samples. Following heat treatment, both sample A and B showed crystalline phases of titanium dioxide (JCPDS: 00-021-1276) and cobalt oxide (01-075-0418). As seen in the atomic percentage composition results, the quantities of C and N significantly decreased compared to the initial quantities. This shows a good correlation with the results obtained during phase analysis, where the TiN and a portion of TiC phases disappeared from the system and the $TiO_2$ phase formed due to heat treatment. The reflections of the cobalt(II)-oxide phase indicate that during heat treatment, the binder material of the substrate, partially diffused onto the surface.

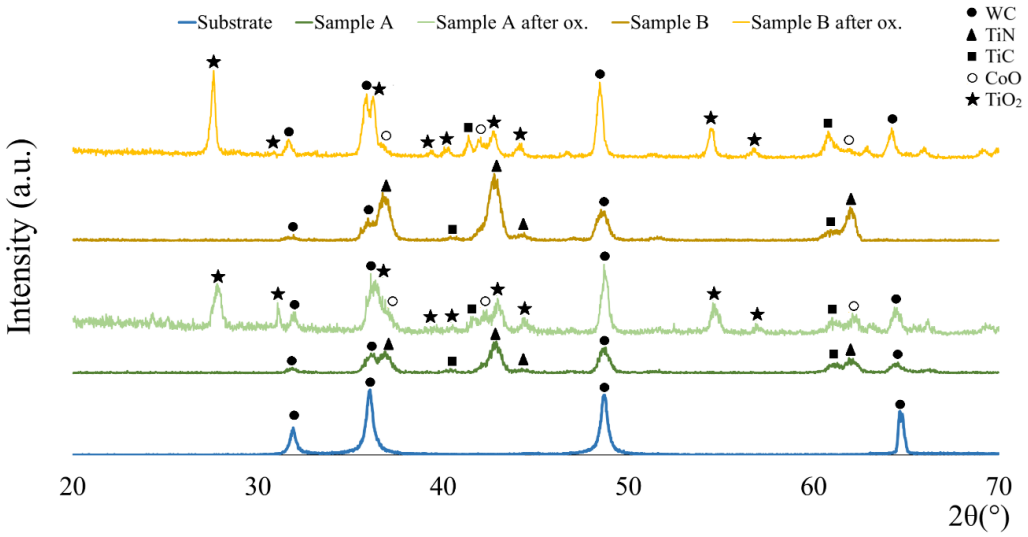


**Figure 43:** X-ray diffraction patterns of the substrate and the coated samples, before and after oxidation test.

### 5.9. Surface morphology analysis of TiN/TiC coatings during oxidation process

Figure 44 and Figure 45 depict the surface morphology of TiN/TiC coatings for samples A and B after each oxidation cycle. During the oxidation test, the release of $CO_2$ and $N_2$ gases tends to escape into the air, leading to the creation and formation of defects and cracks within the coating layers. It is noteworthy that throughout the progression of the oxidation cycles, the TiN/TiC coating layers undergo expansion, attributable to the density differential between TiN/TiC coatings and $TiO_2$ (where the density of $TiO_2$ ranges from 3.84 to 4.26 g/cm³, while the density of TiCN is about 5.18 g/cm³) (*H. Wang et al., 2015*). Additionally, the mismatch in thermal expansion coefficients between the substrate (WC-Co), TiCN, and $TiO_2$ (the coefficient of thermal expansion (CTE) for the WC-Co substrate is $6.24 \cdot 10^{-6}$ 1/K, while the CTE for $TiO_2$, TiC, and TiN are $9.10 \cdot 10^{-6}$ 1/K, $8.31 \cdot 10^{-6}$ 1/K, and $9.29 \cdot 10^{-6}$ 1/K, respectively) (*Huang et al., 2023*), contributes to the formation of initial thermal cracks. Consequently, the progression of the oxidation process leads to the formation of more defects, which increase with the oxidation period. Thus, the results demonstrate that as the oxidation test progresses, the propagation and formation of cracks, allowing the entry of oxygen atoms into the coating layers, thereby accelerating of the oxidation corrosion. Therefore, based on scanning electron microscopy examinations of both sample A and sample B, minor changes were observed in the microstructure after the first oxidation cycle, despite significant changes in the composition of the coating. However,

major cracks appeared after just the 4 min cycle, enabling the gases produced during the reaction to escape.

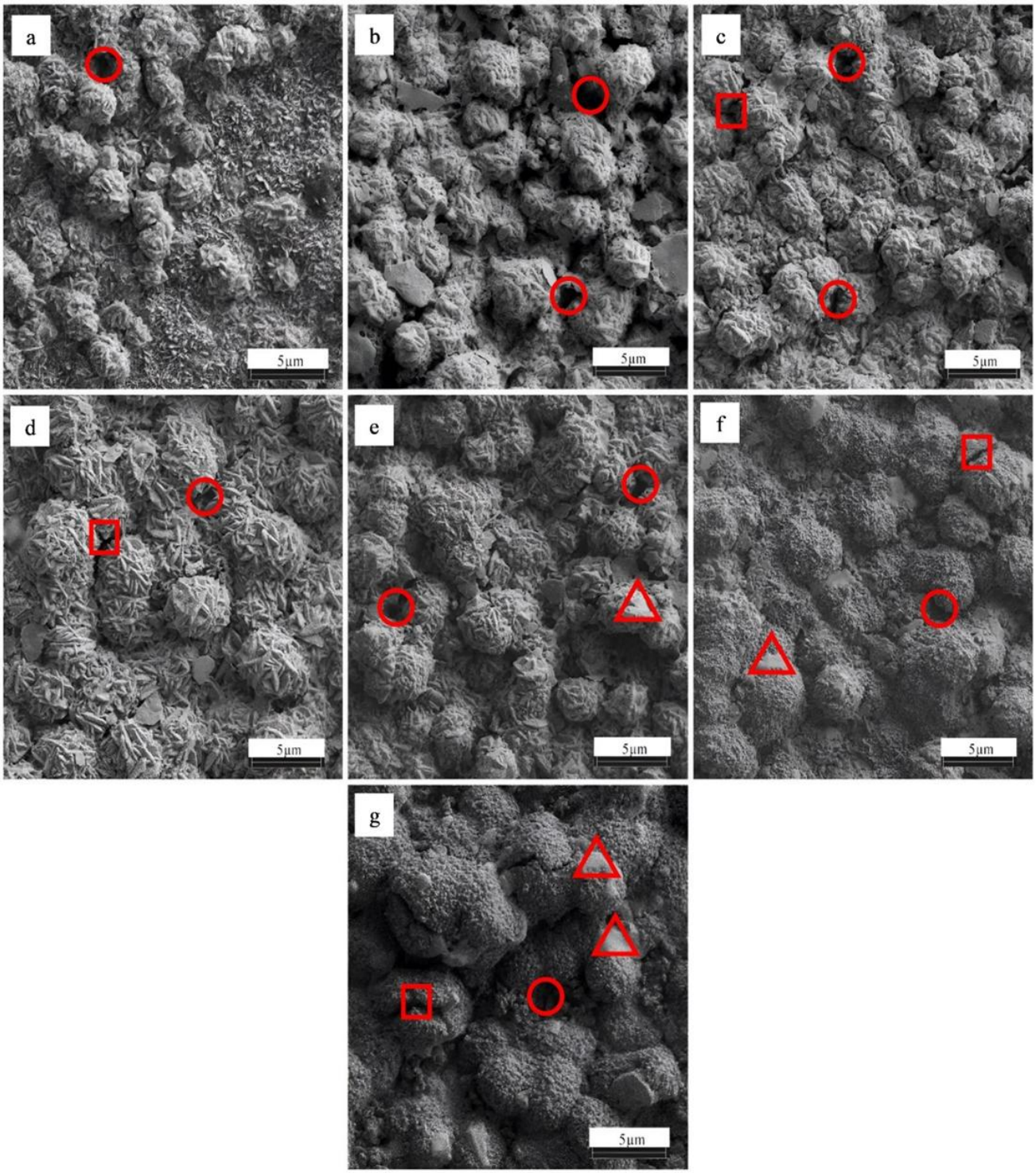


**Figure 44:** SEM images of surface morphology of TiN/TiC coatings for sample A after each oxidation cycle: The circle represents to porosity, square represents to crack and triangle denotes melted zone: (a) after the first; (b) second; (c) third; (d) fourth, (e) fifth; (f) sixth; and (g) seventh, oxidation cycle.

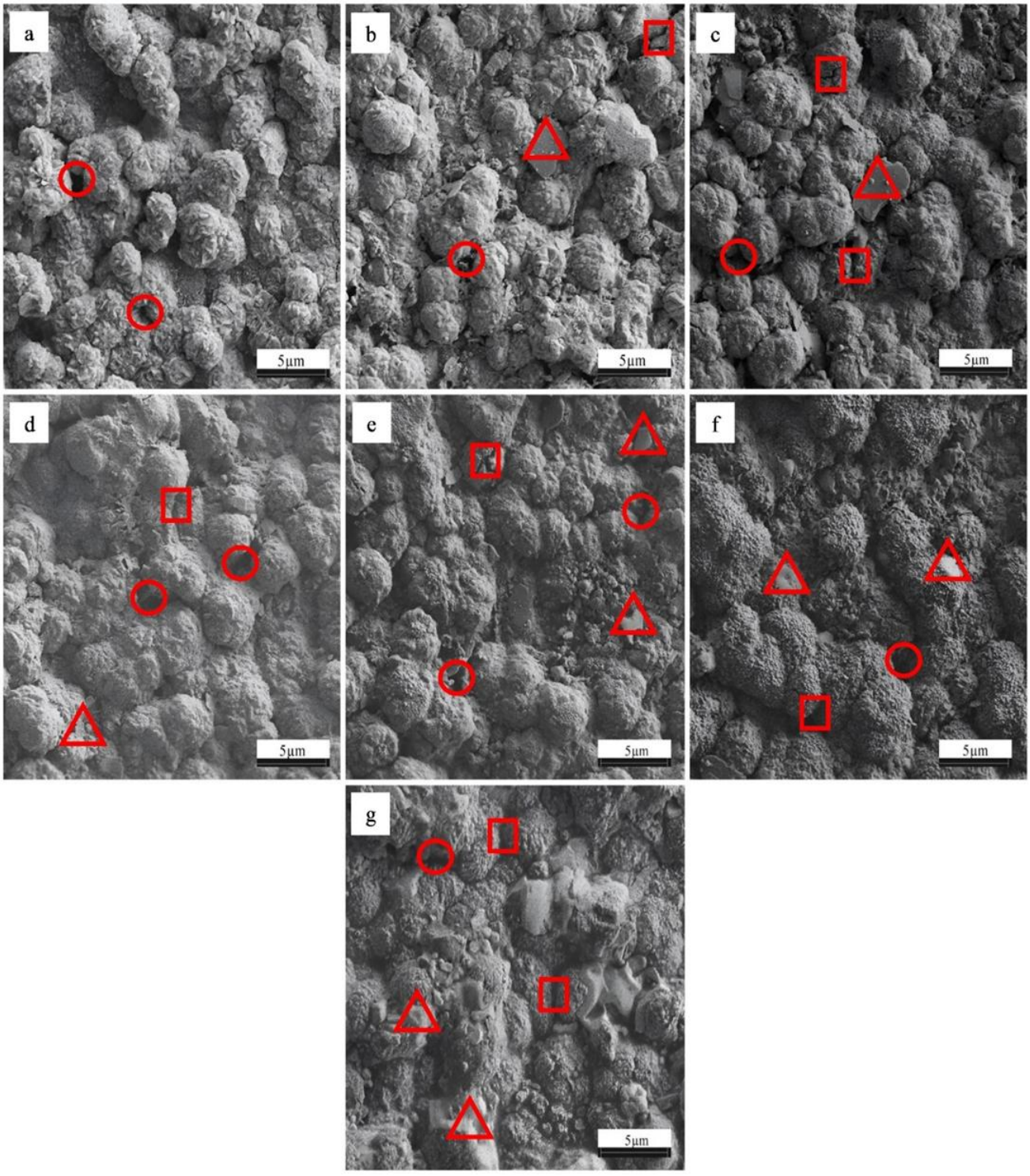


**Figure 45:** SEM images of surface morphology of TiN/TiC coatings for sample B after each oxidation cycle: The circle represents to porosity, square represents to crack and triangle denotes melted zone: (a) after the first; (b) second; (c) third; (d) fourth, (e) fifth; (f) sixth; and (g) seventh, oxidation cycle.

### 5.10. Impact of oxidation on microhardness of CVD coated samples

Vickers hardness test, was employed to comprehensively evaluate the mechanical properties of hard chemical vapor deposition (CVD) coatings. Microhardness plays a significant role in influencing the performance and service life of coated cutting tools. The results presented in Figure 46, illustrate the outcomes of the Vickers hardness test conducted on the top surface of the samples after each oxidation cycle. The error bars in Figure 46 represent the standard deviation calculated from three parallel measurements, ensuring the reliability of the reported values.

Sample A exhibited a reduction in microhardness of approximately 78.15%, while sample B demonstrated a decrease in hardness of about 57.80% after undergoing a 40 min oxidation process at a temperature of 800°C. This reduction in hardness is attributed to the influence of high-temperature oxygen, which actively targets and attacks the protective thin layers, particularly interacting with the titanium element due to its inherent reactivity with oxygen. Consequently, the hard-TiN surface coating (initial thin film layer) completely transformed into titanium oxide (rutile-$TiO_2$), as confirmed by XRD results after the oxidation test.

Significantly, these resultant oxides exhibited reduced microhardness values compared to the hardness of the TiN/TiC coatings before the oxidation test, confirming the adverse impact of oxidation on the hardness properties of the coated samples. Moreover, the significant decrease in the microhardness of the coatings can be attributed to the formation and development of numerous pores and cracks. These defects appeared as a consequence of the escape of gaseous by-products such as $N_2$, CO, and $CO_2$ during the oxidation process, as explained by the scanning electron microscopy (SEM) micrographs.

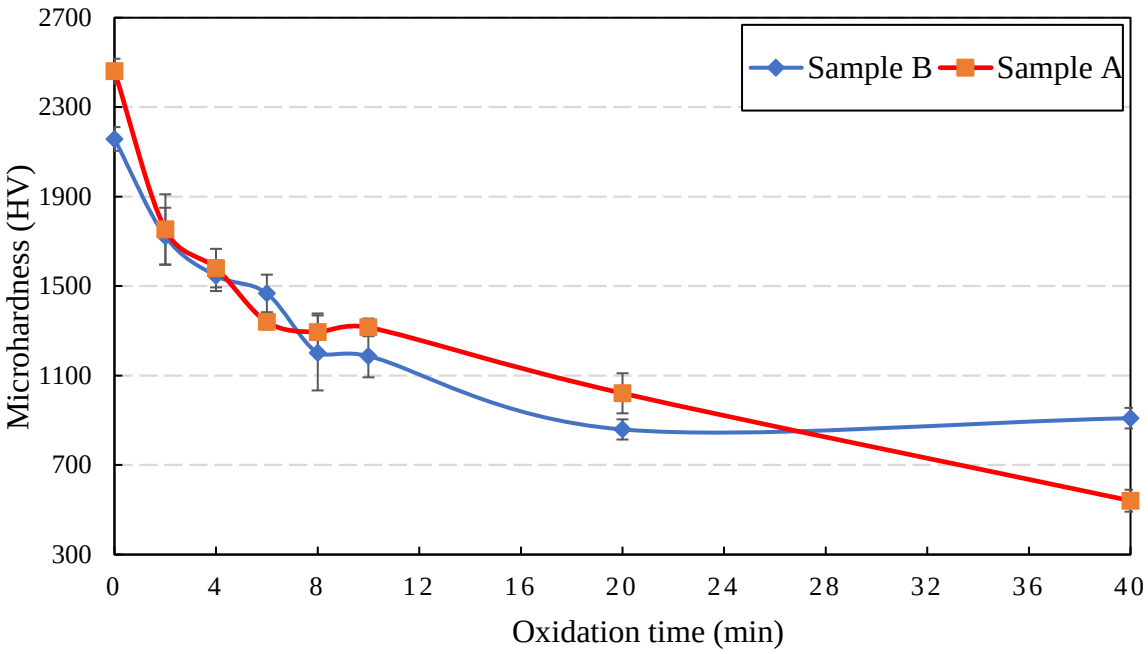


**Figure 46:** Variation of Vickers microhardness with oxidation time.

### 5.11. The wear and friction behaviour of the oxidized coatings

Figure 47 illustrates the influence of sliding duration in the coefficient of friction for oxidized coated samples when subjected to zirconia ball, with oxidation time of 20 min and an oxidation temperature of 800°C. The graphical representation in Figure 47 shows the deviation from the initial static position of the counterpart. This evaluation was conducted under a linearly alternating motion model, with total displacement of 10 mm. In the starting position (0 mm), denoted by $\mu = 0$, the specimen achieves maximum velocity with zero acceleration. Conversely, at positions of +5 mm (indicating a positive μ value) and -5 mm (indicating a negative μ value), the counterpart velocity was zero while the acceleration was maximum. The mean coefficient of friction ($\mu_{av}$) and standard-deviation (SD) found through this test are detailed in legend of Figure 47.

At the onset of the sliding test for sample A, a notable initial peak in the coefficient of friction (μ) is observed, commonly attributed to the initiation of movement between the zirconia ball and the sample surface. Subsequently, fluctuations in the coefficient of friction increase due to the heightened abrasive-wear effect of particles removed from the oxidized coating layers during the test. This can be seen within the region demarcated by the green and yellow lines Figure 47a. Following this, the coefficient of friction stabilizes and reaches

a steady-state condition, as all coating layers are removed, as indicated by the yellow line (Figure 47a).

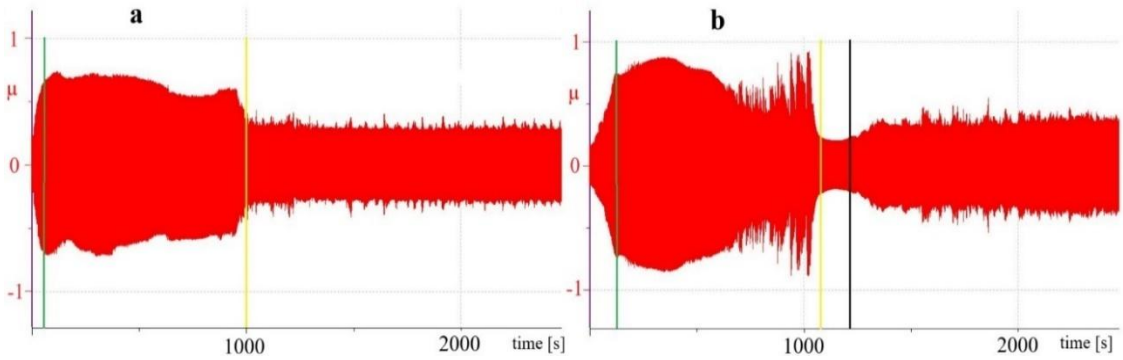


**Figure 47:** Displays the change of coefficient of friction values with sliding time for oxidized coated samples against zirconia ball: (a) sample A, with ($\mu_{av}$) is 0.02 and (sd) of 0.29, (b) sample B, with ($\mu_{av}$) is 0.01 and (sd) of 0.33.

The friction behaviour of sample B exhibits a more pronounced initial peak in the coefficient of friction, followed by a higher unstable value compared to sample A (Fig. 47b). Despite an average coefficient of friction of approximately 0.01, sample B displays a larger standard deviation of 0.33, indicating greater variability in the friction response. Moreover, sample B demonstrates more frequent and higher amplitude fluctuations in the friction coefficient throughout the sliding test, as evidenced within the region delineated by the green and yellow marks (Fig. 47b). These fluctuations may be attributed to the increased removal of particles or debris from oxide layers.

Subsequently, the TiC/TiN coating layers completely wear off from the substrate, appearing as a localized small region bounded by the yellow and black lines (Fig. 47b). This region exhibits the lowest coefficient of friction value observed in the tribological test ($\mu \approx 0.20$). This is attributed to the friction and wear mechanism, where both the zirconia ball and the oxidized sample wear to a similar extent, resulting in continued measurements between surfaces with low surface roughness, thus yielding the lowest coefficient of friction.

As the sliding progresses, the coefficient of friction slightly increases again due to detached particles generating an abrasive effect between the two surfaces of the zirconia ball and the substrate. Figure 48 displays scanning electron microscope (SEM) images of the worn surfaces of sample A and sample B after the tribological test. It is evident that the coating has worn off from the surfaces, and mostly $ZrO_2$ particles can be observed on the surface of the substrate, which was exposed to wear stress. The $ZrO_2$ particles were identified by

Energy-Dispersive Spectroscopy (EDS) analysis, zirconium peaks confirmed it, as detailed in Appendix-D.

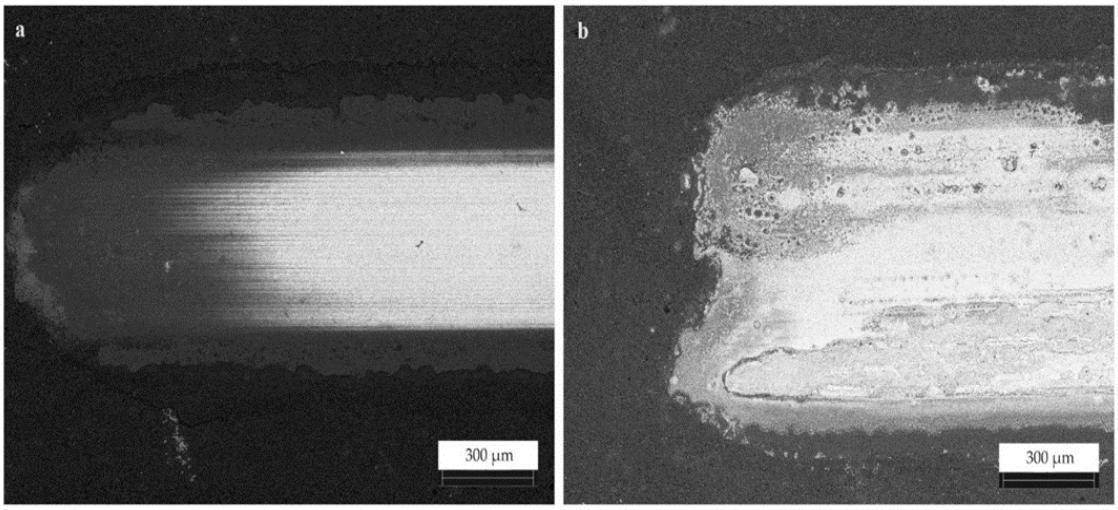


**Figure 48:** Scanning electron micrographs represent the worn surfaces and wear traces for: (a) sample A, and (b) sample B, after the tribological test at a sliding distance of 500 m, and 20 min of oxidation time.

Table 8 presents the tribological responses of CVD coated samples following oxidation tests conducted at an oxidation temperature of approximately 800°C for a duration of 20 min. These samples were subjected to dry sliding tests against a zirconia counterpart, with a sliding distance of 500 m. The experimental data indicate that the oxidation process had a detrimental effect on the tribological behaviour of the CVD coated samples in comparison to the untreated counterparts. Specifically, the volume loss ($V_p$) measurements observed after the oxidation test increased significantly. For sample A, the volume loss increased from $2.04 \cdot 10^5$ to $4.15 \cdot 10^5$, while for sample B, it increased from $1.42 \cdot 10^5$ to $7.31 \cdot 10^5$ during the dry sliding test, as depicted in Table 8 (as mention in section 5.4 tribological analysis of bilayer TiN/TiC coatings).

Overall, the disparity in wear-volume loss observed in oxidized CVD-coated samples, along with the distinct friction behavior of samples A and B, can be attributed to variations in coating properties. The wear loss of sample B increased because its coating underwent greater oxidation compared to sample A, leading to the generation of more wear debris between the ball and the coating surface. This abrasive effect resulted in significantly higher wear loss in sample B. Additionally, factors such as coating thickness, hardness, and surface characteristics played a significant role in influence of the tribological performance.

**Table 8.** Illustrates volume loss ($V_p$) of zirconia ball during the tribology test after/before the oxidation tests.

| Status | Sample | D (µm) | $V_p$ (µm$^3$) |
|---|---|---|---|
| **After oxidation** | **A** | 381.00 | $4.15 \cdot 10^5$ |
| | **B** | 439.00 | $7.31 \cdot 10^5$ |
| **Before oxidation** | **A** | 397.00 | $2.04 \cdot 10^5$ |
| | **B** | 362.00 | $1.42 \cdot 10^5$ |

### 5.12. Change in colour of the test specimen due to the applied thermal shock

Figure 49 illustrates the colour changes on the surface of TiN/TiC coatings at an oxidation temperature of 800°C, with oxidation durations ranging from 2 to 20 min for both samples A and B. The surfaces of the TiN/TiC coatings displayed varying colours after each oxidation cycle. As depicted in Figure 49, the colours observed followed a chromatic scale ranging from gold, light yellow/dark green, brown, to grey-black.

Initially, at 0 min of oxidation time (prior to the oxidation test), the colour on the surface of the coated specimens was gold (Fig. 49a and Fig. 49b). After 2 min of oxidation, light yellow and dark green hues were observed on the samples (Fig. 49c. and Fig. 49d.) respectively. With an increase in oxidation time to 4 min, the colour of the oxidized surface transitioned to brown, as illustrated in (Fig. 49e, Fig. 49f). It is noteworthy that a mixture of yellow and brown hues entirely covered the surface at an oxidation time of 8 min (Fig. 49g and Fig. 49h). Ultimately, a grey-black colour developed on the surfaces of the samples at an oxidation time of approximately 20 min, as depicted in (Fig. 49i and Fig. 49j).

This phenomenon can be utilized for visually evaluating the oxidation stage and identifying oxidation damage when using cutting tools coated with TiCN coatings of the same chemical composition as those used in the present study.

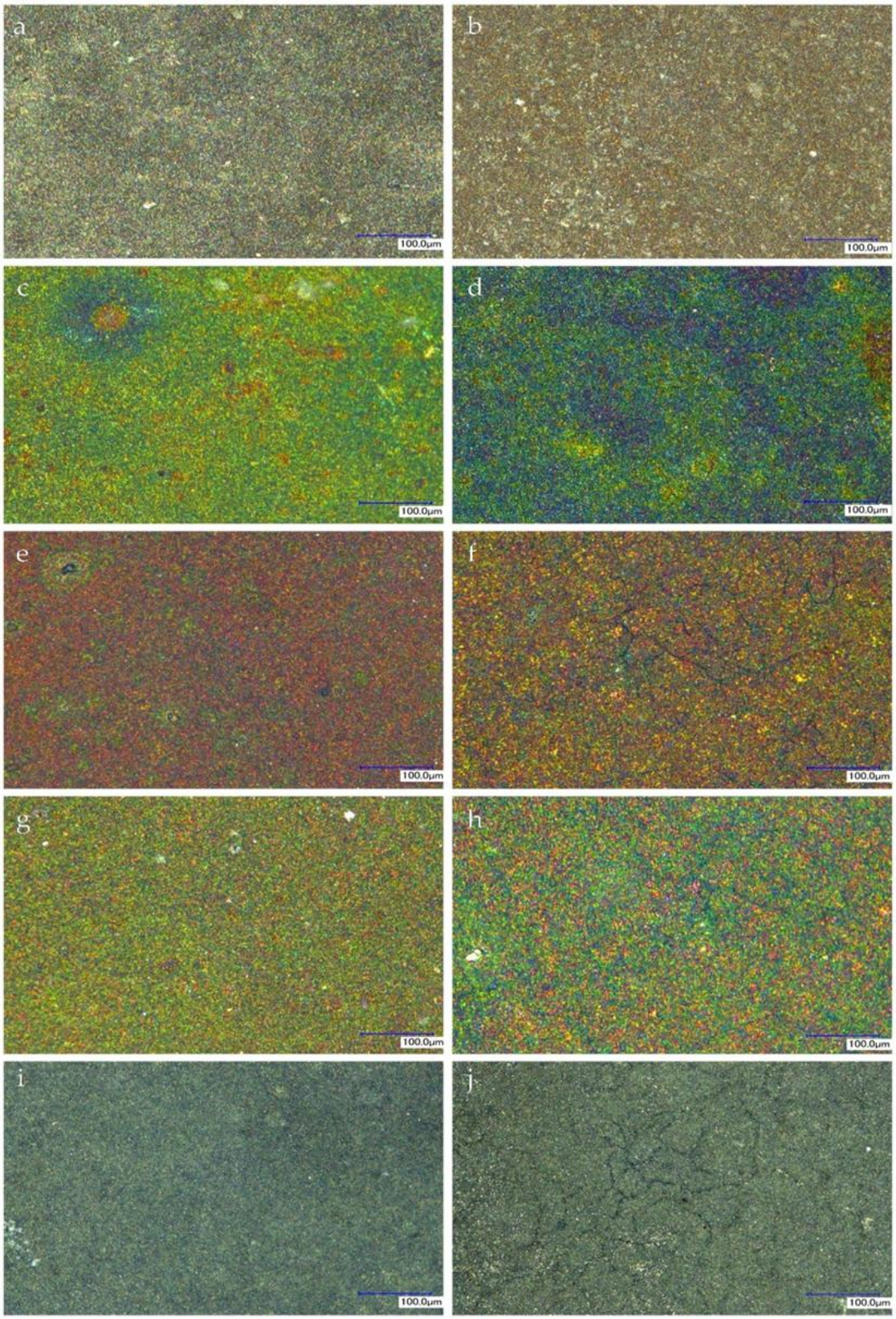


**Figure 49:** Surface color changes of TiN/TiC coatings during oxidation test at 800°C with different periods: (a) and (b) before oxidation test (0 min), (c) and (d) after 2 min, (e) and (f) after 4 min, (g) and (h) after 8 min, and (i) and (j) after 20 min for samples A and B, respectively.

## 6. Comparative analysis of another TiN-based CVD coatings

Table 9 summarizes the samples examined during the experimental work and their abbreviations. The titanium nitride-based coatings were produced with varying manufacturing parameters, including the volumetric flow rate of precursors, temperature, and pressure. Tungsten carbide cobalt cermet and steel were used as substrates for the coatings. One of the most important parameters in this experiment is the thickness of the deposited layers. To determine the layer structure, the samples were embedded in epoxy resin and polished with various grades of abrasive papers. The final polishing step was performed with a suspension containing 3 μm diamond particles. After polishing, the layer thicknesses were measured using scanning electron microscopy.

Nine different samples of titanium nitride-based coatings were examined during the work, with thicknesses ranging from 0.3 to 8.6 μm. For the WC-Co substrate coated with titanium carbide and titanium nitride layers, the main goal was to study the effect of the titanium carbide layer on tool life, similar to the sample containing the aluminum oxide support layer. The purpose of examining the steel sample was to study the tribological properties of the coating with sub-micrometer thickness.

**Table 9.** The abbreviations and the type of other TiN-based coatings.

| Sample | Layer type | Substrate | Thickness (μm) | | |
|---|---|---|---|---|---|
| | | | Layer 1 | Layer 2 | Layer 3 |
| **TiN1** | single layer | WC | 0.3-0.6 | | |
| **TiN2** | single layer | WC | 0.7-0.9 | | |
| **TiN3** | single layer | WC | 1.8-2.8 | | |
| **TiN4** | single layer | WC | 2.9-3.8 | | |
| **TiN5** | single layer | WC | 5.8-7.2 | | |
| **TiN6** | single layer | WC | 6.3-7.8 | | |
| **TiC/TiN** | two-layer | WC | 1.2-1.4 | 1.5-3.1 | |
| **TiCN/Al/TiN** | multi-layer | WC | 8.1-8.6 | 2.2-3.1 | 0.9-1.1 |
| **TiCN** | single layer | ST | 0.5-0.7 | | |

### 6.1. Microstructure and composition of TiN-based coatings

The average elemental composition of the surfaces is summarized in Table 10. Before examination via energy-dispersive X-ray analysis, the samples were cleaned in an

ultrasonic bath with acetone for 5 minutes and then wiped with lint-free cloths. The elemental composition of the WC-labeled substrate shows that, in addition to the WC-based crystalline phases, it contains chromium and cobalt binders. The steel-based substrate primarily consists of iron with small amounts of alloying elements such as carbon, manganese, and chromium, indicating that the substrate is a wear-resistant steel alloy.

The elemental composition of the titanium nitride-based coatings reveals that they mainly contain titanium and nitrogen, with varying atomic percentage ratios depending on the production parameters. However, for the TiN1-TiN4 samples, characteristic X-ray peaks indicative of the substrate also observed in the energy-dispersive spectra. This suggests that the excitation (information) volume depth caused by the electron beam is greater than the coating thickness. The TiN1 and TiN3 samples show relatively high cobalt concentrations, implying that cobalt diffused to the surface due to the high temperatures used during coating deposition (*Cabral et al., 2005*). This diffusion could affect the coating's structure as well as its wear and friction properties. When the coating thickness exceeds 5 μm, elements indicative of the substrate no longer detectable in the composition.

The results from the X-ray diffraction analysis of the coatings are summarized in Table 11. Similar to the findings from the elemental composition analysis, reflections characteristic of the different substrate types observed alongside the reflections from the crystalline phases of the coating. For the titanium nitride-based coatings, the primary crystalline phase is TiN in all cases. However, depending on the production parameters, the TiN1, TiN2, and TiN4 samples also show reflections characteristic of the Ti-O crystalline phase. This indicates that the vacuum or the flow-rate of the precursors, during production was not perfect, causing partial oxidation of the coating at high temperatures, which adversely affects the desired coating quality. For the two-layer coating, it is evident that one of the main components is the TiN crystalline phase, while the other layer comprises TiCN crystalline phases. In the case of the coating reinforced with an aluminum oxide phase, reflections characteristic of $Al_2O_3$ are present. For the steel-based sample, reflections corresponding to the crystalline phases typical of steel are observed. For clarity, only the main crystalline phases are listed in Table 11, while the complete XRD spectra, including low-intensity reflections, are provided in Appendix E.

Figure 50 illustrates the microstructure of various types of coatings. It is evident that the TiN crystalline phases in the TiN1 (Fig. 50a), TiN2 (Fig. 50b), TiN3 (Fig. 50c), and TiN4 samples exhibit a predominantly spherical morphology. In these cases, the layer thickness is less than 4 μm. The TiN1, TiN3, and TiN4 samples have spherical crystals of similar size, although these crystals are much more densely packed on the surface of the TiN4 sample. The crystals in the TiN2 sample are smaller compared to the others. Previous studies indicate that these spherical crystals form when the coating temperature is below 990 °C. In the TiN3 sample, the spherical crystals appear slightly elongated, likely due to cobalt diffusion. TiN5 and TiN6 samples display star-shaped and lenticular-like crystals, which form at reaction temperatures above 1050 °C. The TiN/TiC sample shows star-shaped and rounded particles on its surface, which typically form around 990 °C (*Garcia et al., 2010*). The multi-layered sample also exhibits spherical and lenticular-like crystals, whereas the coating on the steel substrate does not show distinctive crystal shapes, only a few spherical crystals on the surface.

**Table 10**. The elemental composition of substrates and the different types of coatings.

| | WC | ST | TiN1 | TiN2 | TiN3 | TiN4 | TiN5 | TiN6 | TiC/TiN | TiCN/Al/TiN | TiCN |
|---|---|---|---|---|---|---|---|---|---|---|---|
| **W** | 30.5±1.1 | _ | 0.2±0.1 | 0.5±0.1 | 3.7±0.2 | 0.8±0.2 | | | 0.8±0.2 | _ | _ |
| **Co** | 8.6±0.5 | _ | 0.27±0.1 | _ | 10.4±0.3 | 1.9±0.1 | | | 0.7±0.2 | _ | _ |
| **C** | 55.6±5.9 | 0.8±0.2 | _ | | | | | | 33.1±1.2 | _ | 21.6±2.1 |
| **O** | 4.7±0.7 | _ | 2.1±0.2 | 0.8±0.1 | | 1.2±0.1 | | | _ | 6.3±0.6 | _ |
| **Ti** | _ | | 62.1±0.7 | 50.6±0.7 | 31.6±0.6 | 53.7±0.2 | 59.1±0.8 | 54.5±0.8 | 30.9±0.4 | 34.8±0.6 | 8.85±0.2 |
| **N** | _ | _ | 33.5±2.1 | 48.1±3.7 | 54.3±4.1 | 42.5±0.8 | 40.9±2.5 | 45.5±2.6 | 36.4±1.3 | 49.8±3.5 | 24.1±2.2 |
| **Fe** | _ | 98.6±1.9 | | | | | | | _ | _ | 45.1±0.9 |
| **Mn** | _ | 0.3±0.1 | | | | | | | _ | _ | 0.2±0.1 |
| **Cr** | 0.6±0.2 | 0.3±0.2 | | | | | | | 0.88±0.2 | _ | 0.2±0.1 |
| **Al** | _ | | | | | | | | _ | 9.2±0.6 | _ |

**Table 11.** The phase composition of the substrates and the coatings.

| JCPDS card number | Phase | WC | ST | TiN1 | TiN2 | TiN3 | TiN4 | TiN5 | TiN6 | TiC/TiN | TiCN/Al/TiN | TiCN |
|---|---|---|---|---|---|---|---|---|---|---|---|---|
| **01-085-4359** | **WC** | x | | x | x | x | x | x | x | x | x | |
| **01-089-7373** | **Co** | x | | x | | x | x | x | x | x | x | |
| **01-089-2005** | **$Fe_3C$** | | x | | | | | | | | | x |
| **00-006-0696** | **Fe** | | x | | | | | | | | | x |
| **00-051-0997** | **$Fe_5C_2$** | | x | | | | | | | | | x |
| **01-074-8388** | **TiN** | | | x | x | x | x | x | x | x | x | |
| **03-065-9875** | **$TiC_{0.496}N_{0.502}$** | | | | | | | | | x | | x |
| **00-008-0117** | **TiO** | | | x | x | | x | | | | x | |
| **00-023-1455** | **$Ti_2N$** | | | | x | | | | | | | |
| **03-065-4761** | **$W_5N4$** | | | x | | | | | | x | | |
| **00-026-0031** | **$Al_2O_3$** | | | | | | | | | | x | |

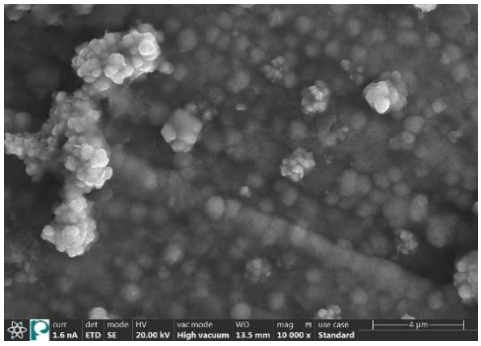

a) TiN1

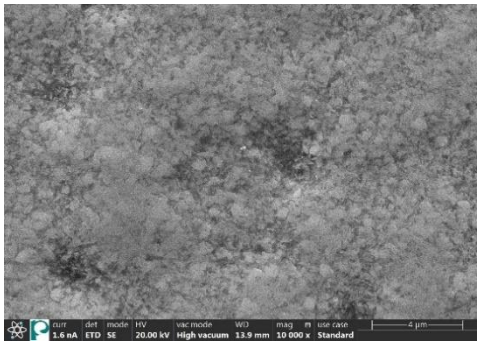

b) TiN2

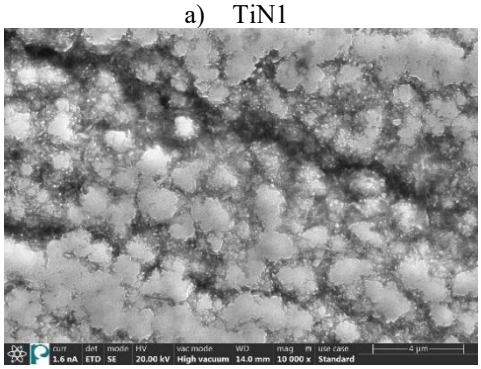

c) TiN3

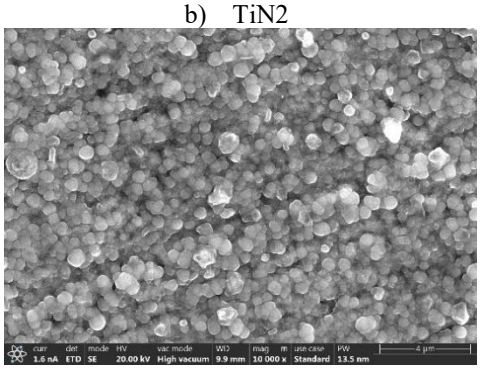

d) TiN4

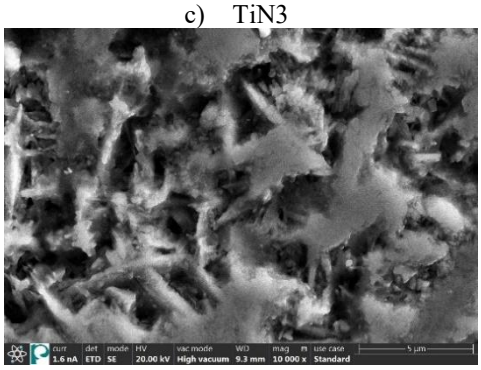

e) TiN5

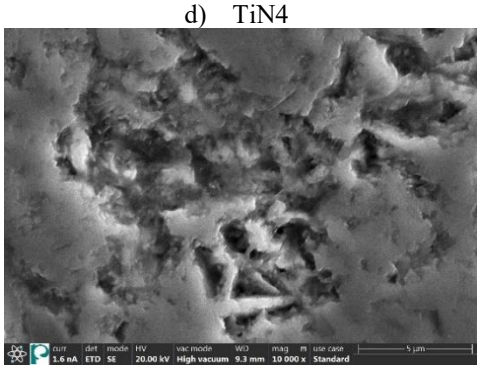

f) TiN6

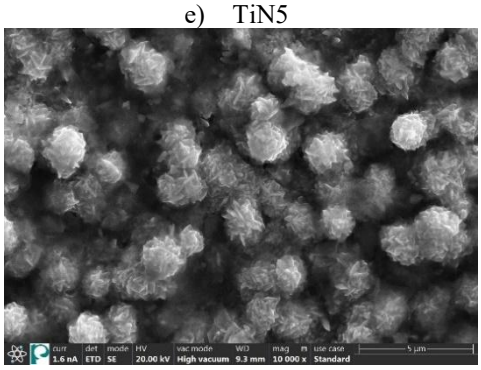

g) TiN/TiC

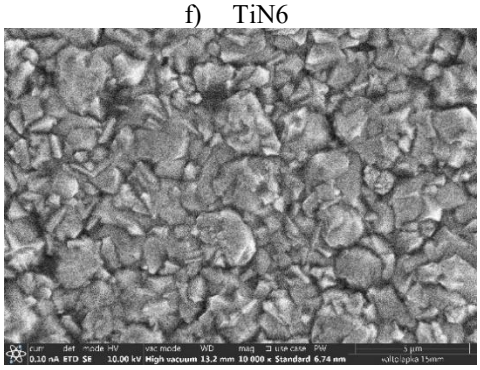

h) TiCN/Al/TiN

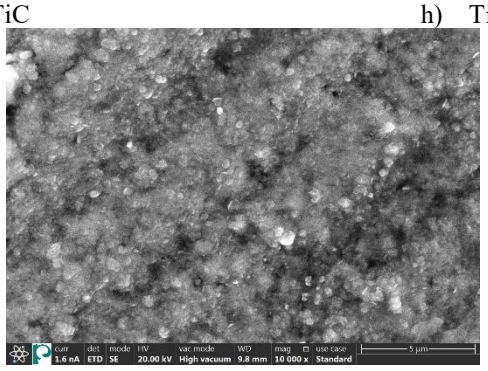

i) TiCN

**Figure 50:** The microstructure of the different types of coatings.

The hardness of the coatings and the penetration depth of the diamond pyramid are summarized in Table 12. The results show that the coatings on the WC substrate generally increased the hardness of the test specimens. However, a decrease in hardness is observed for the TiN5 and TiN6 samples. As seen in the scanning electron microscopy images (Figure 50), these coatings consist of plate-like crystals that fill the available area less effectively, resulting in higher porosity and lower hardness values.

For the TiN1-TiN4 and TiCN samples, the penetration depth exceeds the coating thickness, so this phenomenon must be considered when interpreting the data. Nonetheless, the SEM images clearly show that the spherical and star-shaped crystals cover the surface more uniformly compared to the lenticular-like crystals. The effect of the CVD deposited coating on the hardness of the steel substrate could not be measured, as the coating thickness is less than 1 μm, and the penetration depth on the relatively soft steel is greater than 10 μm. Consequently, the measured hardness value essentially reflects the hardness of the steel itself. In all cases, the hardness of the coatings was measured on the surface, rather than on cross-sectional polished samples. The GPa values presented in Table 12 were numerically calculated from the HV values, following common characterization practices in the literature (*Hovorun et al., 2021*). The conversion was performed by used the standard relationship between Vickers hardness (HV) and GPa, as given by the following equation (*Fischer, 2007*):

$$\text{Hardness (GPa)} = 0.0098 \cdot \text{HV} \tag{5.1}$$

Where, HV is Vickers microhardness and (0.0098) is an empirical constant.

The thermal conductivity of various types of coatings is summarized in Figure 51. The tungsten carbide-cobalt (WC-Co) samples show fundamentally lower thermal conductivity compared to the values measured for steel. For the test specimens coated with TiN and TiC/TiN, the coating thickness was nearly identical, but there was a slight increase in thermal conductivity compared to the reference values. The coating that included a corundum layer exhibited the highest thermal conductivity among the WC-Co samples. For the steel-based test specimen, the highest measured value was 51.2 W/mK. When interpreting the results, the measurement error due to surface irregularities of the test specimens must be considered. As observed in the scanning electron microscopy images, air gaps between the spherical surface particles can affect the measured thermal conductivity of the coated products.

**Table 12.** The hardness of the different coated samples.

| | WC | ST | TiN1 | TiN2 | TiN3 | TiN4 | TiN5 | TiN6 | TiC/TiN | TiCN/Al/TiN | TiCN |
|---|---|---|---|---|---|---|---|---|---|---|---|
| **Value 1 (HV0.2)** | 1801 | 226 | 2027 | 1850 | 2119 | 2250 | 1709 | 1810 | 1875 | 3093 | 238 |
| **Value 2 (HV0.2)** | 1900 | 238 | 2246 | 2189 | 2181 | 2119 | 1668 | 1790 | 1983 | 3203 | 162 |
| **Value 3 (HV0.2)** | 2122 | 130 | 1874 | 1983 | 1889 | 2092 | 1862 | 1785 | 2249 | 2889 | 170 |
| **Av.** | 1941 | 198 | 2049 | 2007 | 2063 | 2153 | 1746 | 1795 | 2035 | 3061 | 190 |
| **Sd.** | 164 | 59 | 187 | 170 | 153 | 84 | 102 | 13 | 192 | 159 | 41 |
| **Hardness (GPa)** | 19.0 | 1.9 | 20.1 | 19.7 | 20.2 | 21.1 | 17.1 | 17.6 | 20.0 | 30.0 | 1.9 |
| **Pd. (µm)** | | | 2.1 | 2.4 | 2.7 | 5.1 | 2.9 | 4.0 | 2.4 | 2.0 | 10.4 |

Based on the thermal conductivity values, it can be concluded that using WC-Co composites as machining tools is advisable, as these typically have lower thermal conductivity, thereby heating up less machining.

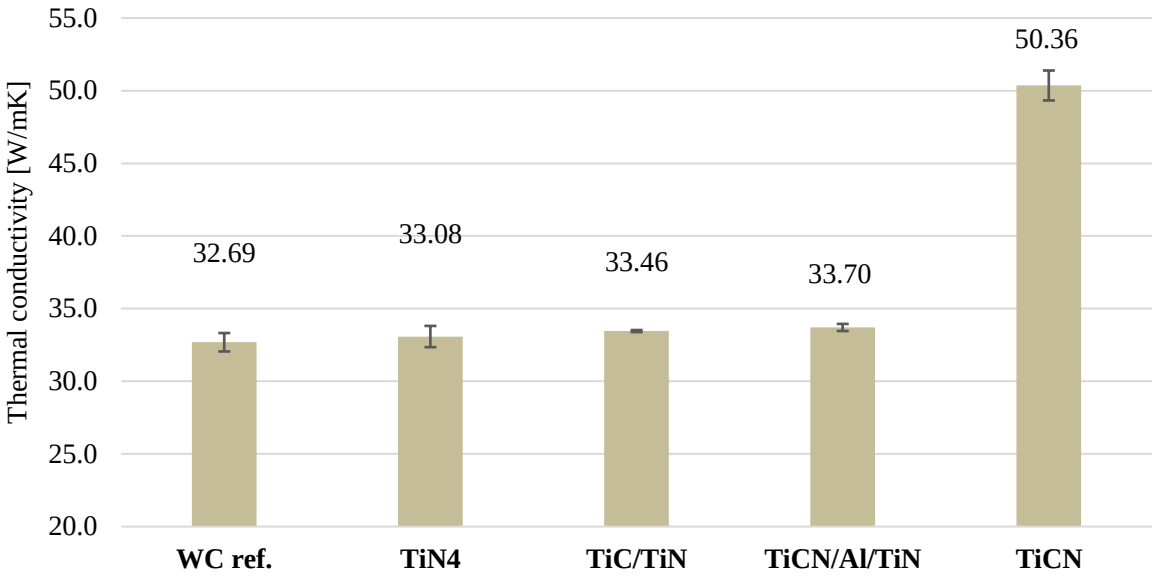


**Figure 51:** The thermal conductivity of the different types of coatings.

### 6.2 Tribological behaviour of another TiN-based coatings systems

This section focuses on the tribological behavior of another TiN-based CVD coatings (TiN, TiC/TiN, TiCN/Al/TiN, TiCN) with different substrates and thicknesses for provide additional insights into their tribological properties. To determine the experimental parameters for the tribological model tests, a test specimen with a TiCN/Al/TiN composite coating was used. The layer structure is illustrated in the elemental map in Figure 52. The figure clearly shows that the layer closest to the substrate contains both nitrogen and carbon, indicating the TiCN layer. This is followed by an aluminum-containing support layer, and then an upper titanium nitride layer. According to the previously presented results (Table 9), the thickness of the upper titanium nitride layer is approximately 1 µm.

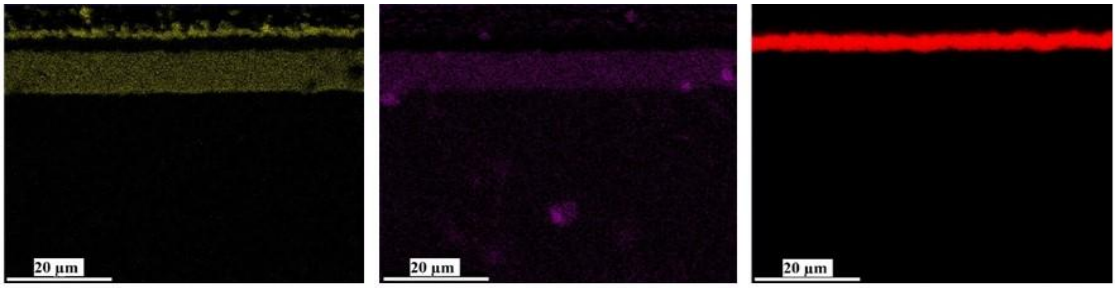


a) b) c)

**Figure 52:** Elemental map of the cross-section of the TiCN/Al/TiN sample, where yellow indicates nitrogen (a), purple indicates carbon (b), and red indicates aluminum (c).

In the first step of the tribological investigations, 6 mm diameter steel ball was used as the static counterpart. During the measurement, the displacement length was 10 mm, the maximum speed of the coated sample was 15.71 cm/s, and the total distance covered was 500 m. Throughout the experimental series, the normal compressive force applied was 10 N, 20 N, and 60 N. In the measurement conducted with a loading force of 10 N, it was observed that the steel used as the static counterpart smeared onto the surface, and after a certain time, the wear and friction mechanism became uninterpretable. This phenomenon indicates that over time, wear surfaces of steel-on-steel were formed, and not the wear of the coating was measured. The experiment was repeated with higher normal compressive forces (20 N and 60 N), but similarly to the previous attempts, the wear surface was not evaluable (Figure 53a). Subsequently, the surface was washed with an 18 vol.% hydrochloric acid solution to remove the smeared steel layer (Figure 53b). It is evident from the figure that the wear surfaces are virtually identical, and despite increasing the normal compressive force, the approximately 1 µm thick TiN coating was not removed even after the 500 m test.

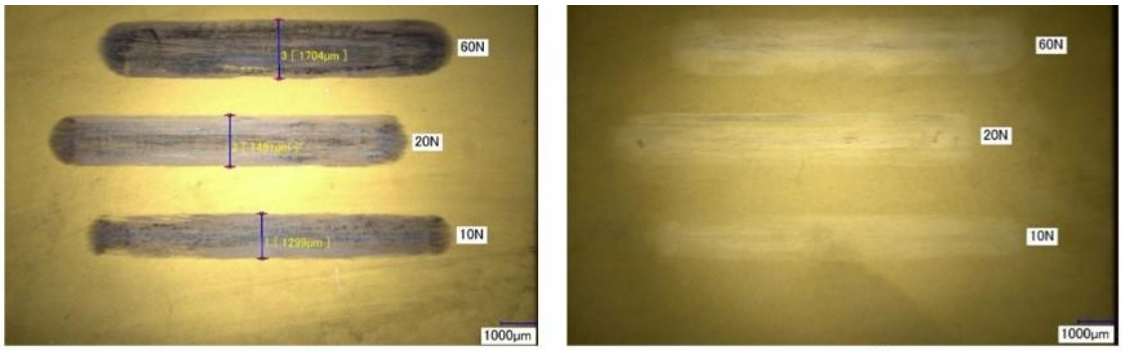


a) b)

**Figure 53:** LM images after the experiments conducted with the steel test specimen, where (a) shows the smeared steel, while (b) shows the surface of the sample after the hydrochloric acid cleaning.

The experiments conducted with a steel static counterpart confirmed that using a material system with hardness comparable to the coating under investigation is advantageous for tribological analysis of titanium nitride and titanium carbide-based coatings (*Badisch et al., 2004*). However, in contrast to earlier studies, where steel was used, the study employed yttrium-stabilized zirconium dioxide balls, which have a hardness of 13-14 GPa (*Candido et al., 2014*). Although the hardness of the $ZrO_2$ balls is slightly lower than that of the coatings, this choice offers several advantages. Zirconia has a high hardness that makes it less prone to wear, and it does not adhere to the surface of the coated sample. This reduces friction and minimizes heat generation during the sliding process, ensuring more stable testing conditions.

Additionally, the use of $ZrO_2$ allowed for detailed examination of the wear track on the coating surface and the volume of material removed from the contact surface of the ball. Further investigations were carried out with $ZrO_2$ based static counterparts, keeping the previously described measurement parameters unchanged. In each test, a normal compressive force of 20 N was applied.

To interpret the wear and friction conditions, the diameter (D) of the circular cross-section wear track formed on the bottom of the $ZrO_2$ ball contact surface due to wear was measured using a light microscope. From this diameter, the wear volume ($V_p$) of material removed from the ball during the tribological test can be calculated using equations (4.1) and (4.2). The results obtained during the measurement are summarized in Table 13.

The last column of the table shows the average surface roughness value specific to each sample. Surface roughness and the crystalline structure formed on the surface also have a significant impact on tribological properties. The friction coefficient value was continuously recorded over time during the measurement using the AntonPaar TRB3 Version 9.0.16. software. If the friction coefficient increases during the measurement, it can be inferred that abrasive particles have entered between the contact surfaces, causing abrasion to both the zirconium oxide ball used for measurement and the sample surface. The first moment of appearance of the abrasive wear effect was considered when the friction coefficient value reached 0.5. From the known measurement time and speed, the distance traveled can be calculated, after which it is presumed that the coating has likely detached from the sample surface.

To confirm the detachment of the surface layer in the wear track, energy-dispersive X-ray analysis was performed. According to the analysis results, the sample with the smallest surface roughness and wear volume is the TiN2 sample with a layer thickness of 0.7-0.9 μm.

**Table 13:** The wear volume loss and average surface roughness values.

| Sample | D (μm) | h (μm) | $V_p$ (μm$^3$) | $R_a$ (μm) |
|---|---|---|---|---|
| **TiN1** | 440.00 | 4.84 | $3.68 \cdot 10^5$ | 0.61 |
| **TiN2** | 268.00 | 1.80 | $5.07 \cdot 10^4$ | 0.16 |
| **TiN3** | 567.00 | 8.04 | $1.02 \cdot 10^6$ | 0.25 |
| **TiN4** | 470.00 | 5.53 | $4.79 \cdot 10^5$ | 0.56 |
| **TiN5** | 505.00 | 6.38 | $6.39 \cdot 10^5$ | 0.36 |
| **TiN6** | 498.00 | 6.20 | $6.04 \cdot 10^5$ | 0.34 |
| **TiC/TiN** | 389.00 | 3.78 | $2.25 \cdot 10^5$ | 0.39 |
| **TiCN/Al/TiN** | 609.00 | 9.28 | $1.35 \cdot 10^6$ | 0.33 |
| **TiCN** | 541.00 | 7.32 | $8.42 \cdot 10^5$ | 0.74 |

In this case, based on the EDS results, the coating did not wear off during the test. Although the friction coefficient value exceeded μ=0.5 after 30.0 m, the abrasive particles did not abrade the surface. Similar results were observed for the TiC/TiN, two-layered sample as well. The average surface roughness in this case is more than double that measured for the TiN2 sample, and the wear volume is nearly an order of magnitude higher. As seen in the first figure, the surface of this sample consists of sharp TiN layer crystals, which have a particularly good abrasive effect. However, during the elemental composition measurement, it was observed that the coating did not detach from the surface. In this case, signs of abrasion appeared on the time-friction coefficient diagram after 4.7 m. The friction coefficient value continued to monotonically increase throughout the remaining measurement time, yet no further layer detachment was observed. For the TiN4 sample, the friction coefficient exceeded the 0.5 value after 204.9 m. Based on the EDS results, in this case, the 2.9-3.8 μm thick coating did not wear off during the tests. The TiN5 and TiN6 samples behaved similarly during the tribological tests. The first detachment of abrasive particles was noticeable after 7.2 m and 7.8 m of travel, respectively. The friction coefficient value remained constant throughout the experiment ($\mu_{max}$=0.95). For the TiCN/Al/TiN sample, signs of detachment of the top layer were visible after 7.1 m. Based on the EDS results, only the upper ~1 μm thick TiN partially detached, while the underlying aluminum oxide layer remained intact. However, the wear volume value was the highest in this case, indicating

that although the TiN layer partially wore off the surface, the coating's abrasive effect continued to prevail during the test. In the case of the TiN1 and TiN3 samples, the coating completely wore off during the measurement. For the TiN1 sample, with a coating thickness below 1.0 μm, it fully detached from the surface after 1.3 m. For the TiN3 sample, the coating likely detached after 150 m according to the tribological test.

The steel substrate coated with a TiCN layer had the highest surface roughness value, but the coating wore off the surface after 15.4 m. Subsequently, the friction coefficient value remained constant throughout the test, indicating that the zirconium oxide ball only abraded the steel substrate.

The effect of surface roughness and microhardness on wear volume is illustrated in Figures 54 and 55. From the figures, it is evident that in the case of stable coatings (where the coating did not wear off), the friction coefficient and wear volume values change analogously. However, there is no similar parallel observed in hardness values. A good example of this is seen in the TiN2 and TiCN/Al/TiN samples, where the surface roughness is the lowest among the samples examined, yet there is a significant difference in wear volume. Thus, from a tribological perspective, in TiN-based systems, it is advantageous for the coating to be fairly dense, have low porosity, and have surface roughness and hardness significantly greater than that of the applied counterpart or the tools in the case of the test specimen being machined. In terms of tribology, apart from wear and friction conditions, the adhesion of the coating to the surface is crucial. For this purpose, a custom-developed scratch test was employed. During the measurement, a diamond stylus with a geometry similar to that used for Vickers hardness testing was drawn along the surface of the test samples for a length of 10.0 mm, with a normal load of 2 N applied over the entire measurement length.

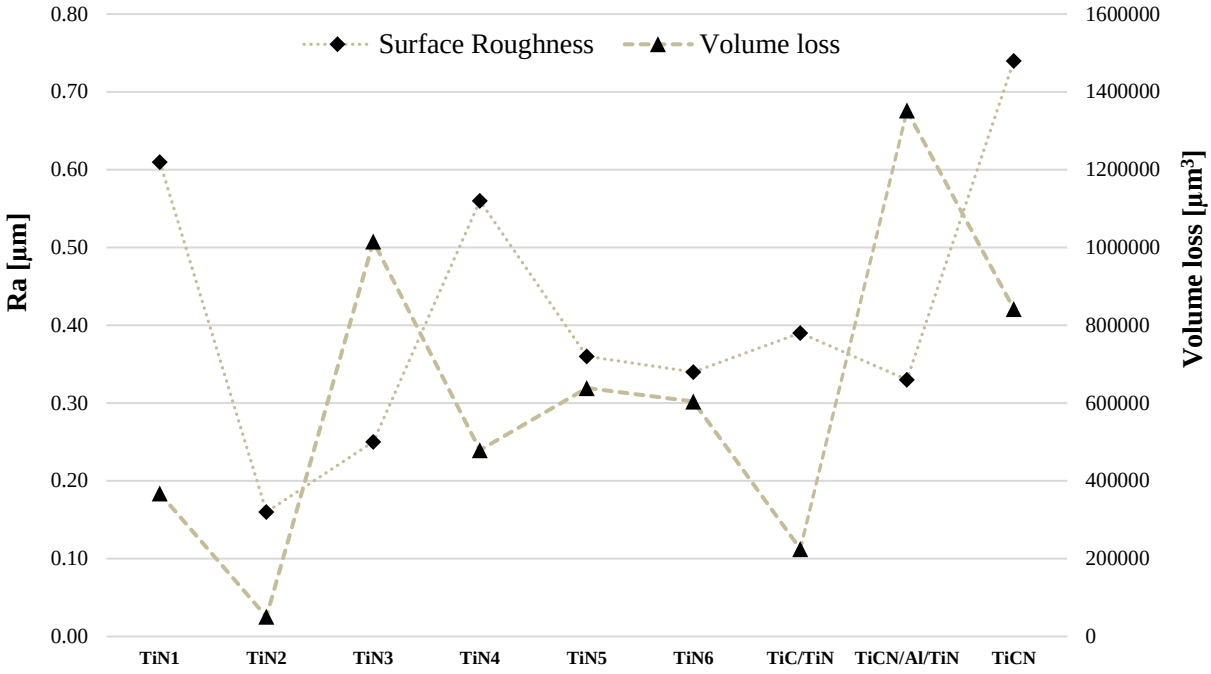


**Figure 54:** The effect of average surface roughness on wear volume.

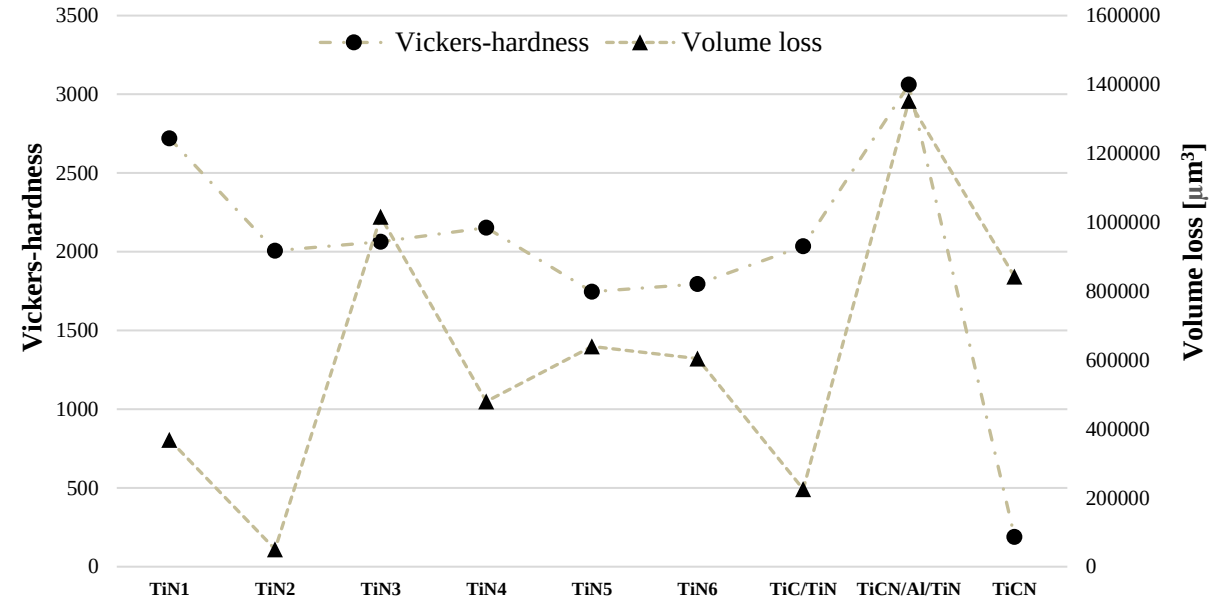


**Figure 55:** The effect of microhardness on wear volume.

As depicted in the Figure 56, for the TiN1 and TiC/TiN samples, the coating flakes off along the scratch line, indicating poor adhesion of the coating to the surface. This is significant in the case of the bilayer coating, as it exhibited favorable properties during tribological tests; however, the adhesion of the layer is weak. The least amount of deformation is observed in the TiN2 and TiCN/Al/TiN coatings. In this case, as evident from the scratch diameter, the stylus did not penetrate deeply into the surface, and there

are no signs of detachment or cracking along the scratch line. Similarly, for the TiN4, TiN5, and TiN6 samples, although the width of the scratch is quite large, there are no signs of detachment. However, in the case of the TiN3 sample, as seen in the backscattered electron image, traces of WC substrate particles are visible along the scratch line, indicating that the coating detached from the surface due to scratching. Figure 56i shows an image of the steel-based coated product after the scratch test, at a lower magnification compared to the other images. In this case, the penetration depth was too high, and the stylus progressed practically without resistance on the surface, easily detaching the coating.

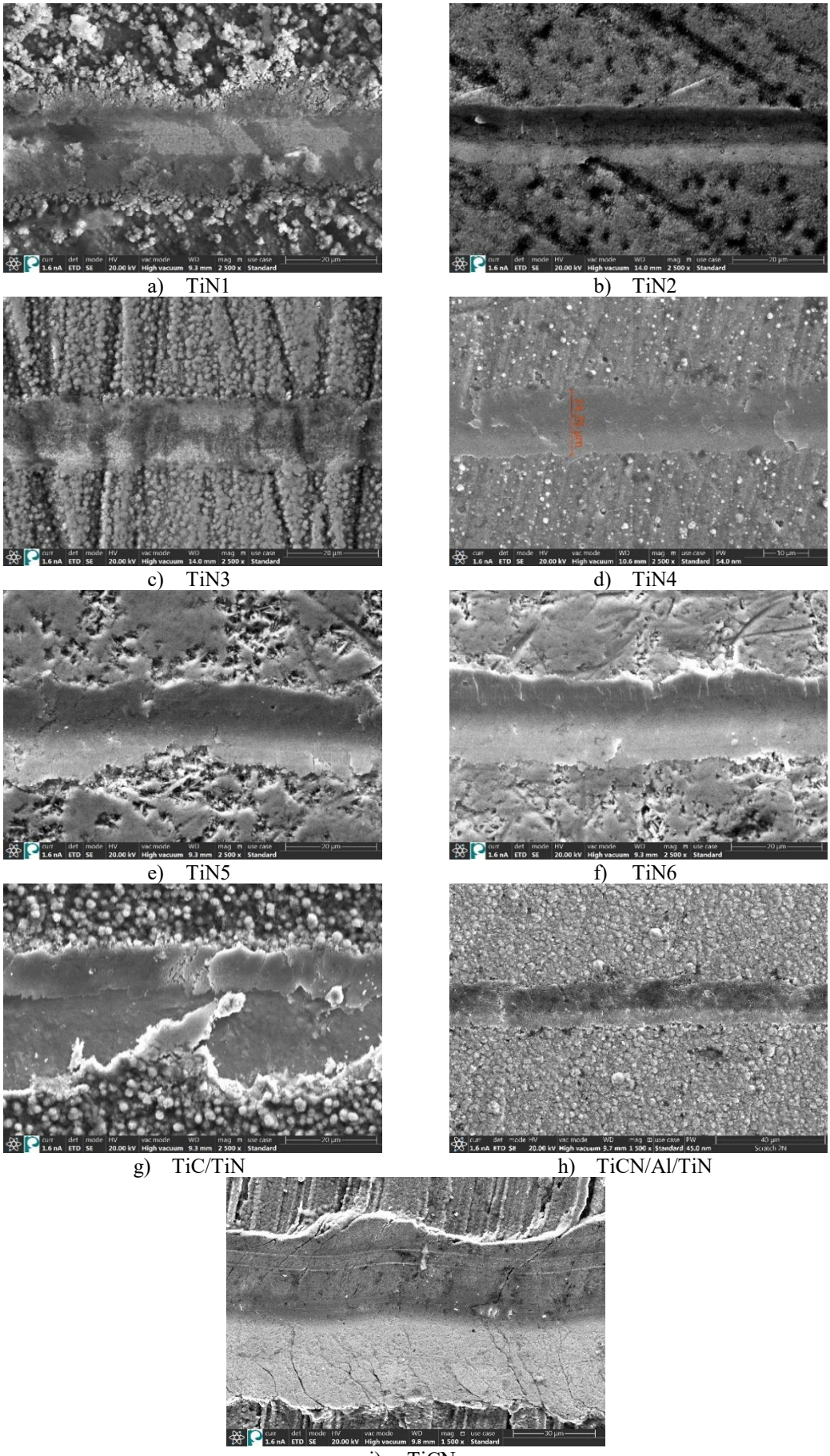

a) TiN1 b) TiN2

c) TiN3 d) TiN4

e) TiN5 f) TiN6

g) TiC/TiN h) TiCN/Al/TiN

i) TiCN

**Figure 56:** Scratch tracks on the surfaces of the test samples.

# 7. Conclusion

This dissertation has investigated the tribological behavior, oxidation resistance, and wear properties of TiN-based coatings produced by chemical vapor deposition (CVD) technology under various conditions on different substrates. The main results focussed on the tribological behavior of CVD bilayer TiN/TiC coatings against zirconia and steel counterparts, their oxidation behavior under high temperatures, and a comparative analysis of other types of TiN-based coatings with different elemental composition and layers thickness, as the following:

## 7.1. Tribological behavior of CVD bilayer TiN/TiC coatings

The investigation into the wear and friction properties of CVD bilayer TiN/TiC coatings produced with different manufacturing parameters on cermet (WC-Co) substrate, revealed several key insights:

1. **Performance against counterparts:** TiN and TiC coatings were tested for wear resistance using steel and zirconia counterparts, revealing that zirconium oxide counterparts are more suitable for the ball-on-disc method, regardless of coating thickness and hardness.
2. **Coefficient of friction observations:** Steel adheres to the coating surface within the first 20-60 seconds, making it unsuitable for wear tests of CVD coatings. In contrast, zirconia does not cause adhesion or surface heating during tests.
3. **Advantages of using zirconia and analysis techniques:** Since the microhardness of the tested coating and zirconium oxide is nearly identical, it is advantageous to use cermet substrate coatings for examination. By applying zirconia balls to the surface and no by-products adhere. Additionally, using the coefficient of friction and EDS line analysis, any potential coating detachment and various wear mechanisms can be excellently traced. Another important point when processing similar material system, the heating of components, which can also be overcome by using zirconium.

## 7.2. Oxidation behavior and mechanical properties

The novel approach to investigating the oxidation behavior and mechanical properties of CVD bilayer TiN/TiC coatings showed critical findings:

1. **Oxidation at high temperatures:** Oxidation tests conducted at 800°C revealed a significant increase in the oxygen content of the coatings, with atomic percentages reaching more than 68 % after 40 minutes of oxidation.
2. **Elemental changes:** Carbon and nitrogen contents decreased substantially due to interactions with oxygen, forming gaseous by-products like CO, $CO_2$, and $N_2$. XRD analysis confirmed the transformation of the TiN coating into titanium oxide (rutile-$TiO_2$) after 20 minutes of oxidation due to nitrogen depletion.
3. **Impact on mechanical properties:** The oxidation process had a detrimental-effect on the mechanical properties of the coatings. The Vickers microhardness of sample A decreased by 78.15%, while sample B reduced about 57.80% after the 40 min of the oxidation test. This significant decrease in hardness was attributed to the formation of oxides and the development of numerous pores and cracks due to the escape of gaseous by products. Also, the tribological tests revealed that the oxidation process adversely affected on the wear and friction behaviour of the CVD coated samples. The volume loss during dry sliding tests against a zirconia counterpart increased significantly after the oxidation test, with sample A exhibited an increased from $2.04 \cdot 10^5$ to $4.15 \cdot 10^5$ $\mu m^3$, and sample B an increased from $1.42 \cdot 10^5$ to $7.31 \cdot 10^5$ $\mu m^3$.
4. **Visual evaluation of oxidation damage:** The study observed that the color of the TiN/TiC coatings changed from gold to grayish-black during oxidation, which can serve as a visual indicator for assessing oxidation stages and identifying damage in coated cutting tools.

### 7.3. Comparative analysis of TiN, TiC/TiN, TiCN/Al/TiN and TiCN coatings

The comparative study of various CVD TiN-based coatings, with thicknesses ranging from 0.3 to 8.6 μm and different elementals composition ranging (TiN, TiC/TiN, TiCN/Al/TiN and TiCN) for WC-Co and steel substrates, provided additional insights into their tribological and mechanical properties:

1. For tribological model testing of TiN-based coatings, it is necessary to select a static counterpart with a hardness close to that of the test specimen, as inadequate hardness can result in the coating not being damaged even with increased normal loading.
2. In terms of tribology, the average surface roughness of the test specimens has a greater impact on the wear volume than their hardness.

3. The stability of coatings is not dependent on their thickness but rather on their surface roughness and hardness.
4. From a tribological and micro-machining perspective, it is much more advantageous to use tools coated with a CVD process that results in sharp, lenticular-like crystals on the surface.
5. For long-term usage, it is advisable to develop a coating that includes a support layer between the titanium-based layers.
6. Tribological model tests do not always adequately reflect the adhesion of the respective coatings to the surface; therefore, it is advisable to conduct supplementary scratch tests.

## 8. New scientific results: thesis statements of the doctoral dissertation

**1.)** I have experimentally demonstrated that steel counterparts exhibit significant adhesion to the coating surface within a critical time of 20–60 seconds during ball-on-disc test, while zirconia counterparts show no adhesion effects. Moreover, I have established that using zirconium oxide effectively eliminates the heating of components when processing similar material systems (*Jakab et al., 2023*).

**2.)** Through a novel approach, I have analyzed the oxidation behavior of CVD bilayer TiN/TiC coatings at 800°C, quantitatively demonstrate that the oxygen content increases to over 68% after 40 minutes, accompanied by a significant decrease in carbon and nitrogen due to their interaction with oxygen. XRD analysis confirmed the transformation of TiN into rutile-$TiO_2$ after 20 minutes (*Ali et al., 2024*).

**3.)** The oxidation process significantly affected the mechanical properties of CVD bilayer TiN/TiC coatings, particularly in terms of hardness degradation and volume loss, as detailed below:

Statement 3a:

Oxidation at 800 °C led to a reduction in Vickers-microhardness, decreasing by 78.15% and 57.80% for sample A and sample B, respectively, after 40 minutes. This decline is attributed to oxide formation, increased porosity, and crack development caused by the release of gaseous by-products (*Ali et al., 2024*).

Statement 3b:

Tribological performance was similarly affected. Dry sliding tests conducted using a zirconia counterpart at a sliding speed of 15.71 cm/s and an applied normal load of 20 N revealed a significant increase in volume loss. Specifically, the volume loss increased from $2.04 \cdot 10^5$ to $4.15 \cdot 10^5$ µm³ for sample A, and from $1.42 \cdot 10^5$ to $7.31 \cdot 10^5$ µm³ for sample B (*Ali et al., 2024*).

**4.)** Through observation of the oxidized surfaces of CVD TiN/TiC coatings, I have demonstrated a color change from gold/yellow to greyish-black during oxidation process. This color transition can serve as a visual indicator for evaluate the oxidation stages and identify the damage in coated cutting tools with same elemental composition (*Ali et al., 2024*).

**5.)** Through comparative analysis, I have established that the stability of TiN-based CVD coatings—defined by their structural integrity and wear resistance—is primarily dominated by surface roughness and hardness. These factors play a more significant influence on wear volume than coating thickness (*Osamah Ali et al., 2024*).

## 9. Recommendations and future work

The results presented in this dissertation significantly contribute to the understanding of TiN-based CVD coatings and their application in cutting tools. Based on these findings, the following recommendations and future research directions are proposed:

1. **Standardization of tribological tests**: This dissertation has experimentally demonstrated the superiority of zirconia counterparts over steel in the tribological evaluation of TiN-based CVD coatings. Therefore, it is recommended to assess other CVD coatings, such as $Al_2O_3$ and SiC, by use zirconia as preferred counterpart material in ball-on-disc tests.
2. **Enhancement of oxidation resistance**: To address the observed degradation in mechanical properties during the oxidation processes, it is recommended to investigate the incorporation of oxidation-resistant elements (such as: Al, Cr, Si) into TiN-based coating system, and study the diffusion mechanisms during the oxidation for better understand and control the degradation process.
3. **Chromatic evaluation of oxidation**: The observed color change in the oxidized TiN/TiC coatings from gold/yellow to greyish-black during oxidation provides a visual indicator for evaluating the oxidation damage progression. It is recommended to employ color analysis methods such as CIELAB color space evaluation, RGB or HSV image processing for numerical analysis of color transformations during the oxidation. Standardized color charts could be developed to correlate specific chromatic shifts with the oxidation levels.
4. **Cross-sectional hardness profile**: For more comprehensive evaluation of mechanical performance, it is recommended to conduct cross-sectional hardness profile, which enables measurement of individual layers, interfaces between coating layers, and the coating–substrate interface, as well as the hardness gradients across the coating thickness. This methodology would provide enhanced understand of how multilayer construction and oxidation effect on local mechanical properties.
5. **Investigation of intermediate support layers**: Based on the findings that a support layer between titanium-based coatings is beneficial for long-term applications, future research should focus on systematic investigation of various intermediate layer materials (such as: $SiO_2$, CrN or HfN) between titanium-based layers and optimization of intermediate layer thickness for maximum adhesion and wear resistance.

## 10. Bibliography


1. **Abadias, G.,** Chason, E., Keckes, J., Sebastiani, M., Thompson, G. B., Barthel, E., Doll, G. L., Murray, C. E., Stoessel, C. H., & Martinu, L. (2018). Review Article: Stress in thin films and coatings: Current status, challenges, and prospects. *Journal of Vacuum Science & Technology A: Vacuum, Surfaces, and Films*, *36*(2), 020801. https://doi.org /10.1116/1.5011790

2. **Abu-Thabit, Y.,** & Makhlouf, A. S. H. (2020). Chapter 1—Fundamental of smart coatings and thin films: Synthesis, deposition methods, and industrial applications. In A. S. H. Makhlouf & N. Y. Abu-Thabit (Eds.), *Advances in Smart Coatings and Thin Films for Future Industrial and Biomedical Engineering Applications* (pp. 3–35). Elsevier. https://doi.org/10.1016/B978-0-12-849870-5.00001-X

3. **Acosta, E.** (2021). Thin Films: Properties and Applications. In *Thin Films*. Intech Open. https://doi.org/10.5772/intechopen.95527

4. **Aihua, L.,** Jianxin, D., Haibing, C., Yangyang, C., & Jun, Z. (2012). Friction and wear properties of TiN, TiAlN, AlTiN and CrAlN PVD nitride coatings. *International Journal of Refractory Metals and Hard Materials*, *31*, 82–88. https://doi.org/ 10.1016/j.ijrmhm.2011.09.010

5. **Akgün, M.,** Özlü, B., & Kara, F. (2023). Effect of PVD-TiN and CVD-$Al_2O_3$ Coatings on Cutting Force, Surface Roughness, Cutting Power, and Temperature in Hard Turning of AISI H13 Steel. *Journal of Materials Engineering and Performance*, *32*(3), 1390–1401. https://doi.org/10.1007/s11665-022-07190-9

6. **Alcántara, V.** (2020). Coated Tungsten Carbide Inserts-Efects on Machinability in turning AISI1020 steel. *International Journal of Recent Technology and Engineering*, *9*. https://doi.org/10.35940/ijrte.D5026.119420

7. **Alvaredo, P.,** Tsipas, S., & Gordo, E. (2013). Influence of carbon content on the sinterability of an FeCr matrix cermet reinforced with TiCN. *International Journal of Refractory Metals and Hard Materials*, *36*, 283. https://doi.org/10.1016/ j.ijrmhm. 2012.10.007

8. **Ali, O.,** & Gyurika, I. (2024). Oxidation Behaviour of TiC/TiN Coatings Deposited by Chemical Vapor Deposition (CVD): Mechanisms, Structures, and Properties. Archives of Advanced Engineering Science, 1–12. https://doi.org/10.47852/bonview AAES42022613

9. **Ardebili, H.,** & Pecht, M. G. (2009). Chapter 6—Defect and Failure Analysis Techniques for Encapsulated Microelectronics. In H. Ardebili & M. G. Pecht (Eds.), *Encapsulation Technologies for Electronic Applications* (pp. 287–350). https://doi.org/ 10.1016/B978-0-8155-1576-0.50010-3

10. **ASTM G99-05;** Standard Test Method for Wear Testing with a Pin-on-Disk Apparatus. ASTM International: West Conshohocken, PA, USA, 2010.

11. **ASTM G133-05;** Standard Test Method for Linearly Reciprocating Ball-on-Flat Sliding Wear. ASTM International: West Conshohocken, PA, USA, 2010.

12. **Azadi, M.** (2018). Deposition of TiN, TiC, and DLC coatings by PACVD. In *Production, Properties, and Applications of High Temperature Coatings*. https://doi.org/10.4018/978-1-5225-4194-3.ch014

13. **Azadi, M.,** Sabour Rouh Aghdam, A., Ahangarani, S., Mofidi, H., & Valiei, M. (2014). Mechanical behavior and properties of TiN/TiC coating using PACVD. *Advanced Materials Research*, *829*, 476. https://doi.org/10.4028/www.scientific.net/AMR.829.476

14. **Badisch, E.,** Fontalvo, G. A., & Mitterer, C. (2004). The response of PACVD TiN coatings to tribological tests with different counterparts. *Wear*, *256*(1), 95–99. https://doi.org/10.1016/S0043-1648(03)00391-0

15. **Bagnall, C.,** Capo, J., & Moorhead, W. J. (2018). Oxidation Behavior of Tungsten Carbide-6% Cobalt Cemented Carbide. *Metallography, Microstructure, and Analysis*, *7*(6), 661–679. https://doi.org/10.1007/s13632-018-0493-7

16. **Banapurmath, R.,** Tungal, M. R., Hallad, S. A., Kaladagi, K. S., Angadi, N. B., & Shettar, A. S. (2018). Tribological studies on bearings coated with titanium carbo-nitride (TiCN) using chemical vapour deposition (Cvd) method. *Journal of Applied Research and Technology*, *16*(4), 312–319.

17. **Bejjani, R.,** Odelros, S., Öhman, S., & Collin, M. (2021). Shift of wear balance acting on CVD textured coatings and relation to workpiece materials. *Proceedings of the Institution of Mechanical Engineers, Part J: Journal of Engineering Tribology*, *235*(1), 114–128. https://doi.org/10.1177/1350650120926781

18. **Bjerke, A.,** Lenrick, F., Norgren, S., Larsson, H., Markström, A., M'Saoubi, R., Petrusha, I., & Bushlya, V. (2022). Understanding wear and interaction between CVD α-$Al_2O_3$ coated tools, steel, and non-metallic inclusions in machining. *Surface and Coatings Technology*, *450*, 128997. https://doi.org/10.1016/j.surfcoat.2022.128997

19. **Boing, D.,** De Oliveira, A. J., & Schroeter, R. B. (2020). Evaluation of wear mechanisms of PVD and CVD coatings deposited on cemented carbide substrates applied to hard turning. *The International Journal of Advanced Manufacturing Technology*, *106*(11–12), 5441–5451. https://doi.org/10.1007/s00170-020-05000-x

20. **Bonetti, S.,** Wiprächtiger, H., & Mohn, E. (1990). CVD of titanium carbonitride at moderate temperature: Properties and applications. *Metal Powder Report*, *45*(12), 837–840. https://doi.org/10.1016/0026-0657(90)90575-2

21. **Bouzakis, K.,** Skordaris, G., Gerardis, S., Katirtzoglou, G., Makrimallakis, S., Pappa, M., & Saoubi, R. (2009). Ambient and elevated temperature properties of TiN, TiAlN and TiSiN PVD films and their impact on the cutting performance of coated carbide tools. *Surface and Coatings Technology*, *204*(6), 1061–1065. https://doi.org/10.1016/j.surfcoat.2009.07.001

22. **Brümmer, O.,** Giber, J., Csanády, A., Szőkefalvi-Nagy, Z., Kövér, L., Kálmán, A., Menyhárd, M., Szász, A., Pozsgai, I. (1984). *Szilárd testek vizsgálata elektronokkal, ionokkal és röntgensugarakkal*. Műszaki Könyvkiadó. ISBN: 963-10-5521-3

23. **Bull, S.,** Rickerby, D., Matthews, A., Leyland, A., Pace, A., & Valli, J. (1988). The use of scratch adhesion testing for the determination of interfacial adhesion: The importance of frictional drag. *Surface & Coatings Technology*, *36*(1–2), 503–517. https:// doi.org/ 10.1016/0257-8972(88)90178-8

24. **Cabral, G.,** Ali, N., Titus, E., & Gracio, J. (2005). Cobalt diffusion in different microstructured WC-Co substrates during diamond chemical vapor deposition. *Journal of Phase Equilibria and Diffusion*, *26*(5), 411–416. https://doi.org/10.1007/s11669-005-0027-2

25. **Çalışkan, H.,** Panjan, P., & Kurbanoglu, C. (2017). Hard Coatings on Cutting Tools and Surface Finish. In *Reference Module in Materials Science and Materials Engineering* (pp. 230–242). https://doi.org/10.1016/B978-0-12-803581-8.09178-5

26. **Candido, L.,** Fais, L., Reis, J., & Pinelli, L. (2014). Surface roughness and hardness of yttria stabilized zirconia (Y-TZP) after 10 years of simulated brushing. *Rev Odontol UNESP*, *43*, 379–383. https://doi.org/10.1590/1807-2577.1049

27. **Canovic, S.,** Ruppi, S., Rohrer, J., Vojvodic, A., Ruberto, C., Hyldgaard, P., & Halvarsson, M. (2007). TEM and DFT investigation of CVD TiN/κ–Al2O3 multilayer coatings. *Surface and Coatings Technology*, *202*(3), 522–531. https://doi.org/10.1016/ j.surfcoat.2007.06.022

28. **Carlsson, J.** (1985). Processes in interfacial zones during chemical vapour deposition: Aspects of kinetics, mechanisms, adhesion and substrate atom transport. *Thin Solid Films*, *130*(3), 261–282. https://doi.org/10.1016/0040-6090(85)90358-X

29. **Carlsson, J.,** & Martin, P. M. (2010). Chemical Vapor Deposition. In *Handbook of Deposition Technologies for Films and Coatings* (pp. 314–363). Elsevier. https://doi.org/10.1016/B978-0-8155-2031-3.00007-7

30. **Chandra, G.,** Prasad Sahoo, S., Kumari, S., & Datta, S. (2023). Study on wear morphology of uncoated and MT-CVD TiCN-$Al_2O_3$ coated carbide inserts during dry machining of Inconel 825 superalloy. *Materials Today: Proceedings*. https://doi.org/ 10.1016/j.matpr.2023.02.013

31. **Chen, H.,** Wang, Y., Jiao, J., Zhou, C., Tan, Z., Zhong, Z., Huang, L., & Peng, Y. (2024). Influence of different wet-blasting pressure on the surface integrity and tool cutting performance of hybrid CVD-TiN/TiCN/α-$Al_2O_3$/TiN coated tools. *Wear*, 546–547, 205327. https://doi.org/10.1016/j.wear.2024.205327

32. **Chen, H.,** & Lu, F.-H. (2005). Oxidation behavior of titanium nitride films. *Journal of Vacuum Science & Technology A: Vacuum, Surfaces, and Films*, *23*(4), 1006–1009. https://doi.org/10.1116/1.1914815

33. **Chen, X.,** Liu, H., Guo, Q., & Sun, S. (2012). Oxidation behavior of WC–Co hard metal with designed multilayer coatings by CVD. *International Journal of Refractory Metals and Hard Materials*, *31*, 171–178. https://doi.org/10.1016/j.ijrmhm.2011.10.012

34. **Cheng, W.,** Wang, J., Ma, X., Liu, P., Liaw, P. K., & Li, W. (2023). A review on microstructures and mechanical properties of protective nano-multilayered films or

coatings. *Journal of Materials Research and Technology*, 27, 2413–2442. https://doi.org/10.1016/j.jmrt.2023.10.012

35. **Cheng, Y.,** Browne, T., Heckerman, B., & Meletis, E. I. (2010). Mechanical and tribological properties of nanocomposite TiSiN coatings. *Surface and Coatings Technology*, *204*(14), 2123–2129. https://doi.org/10.1016/j.surfcoat.2009.11.034

36. **Chowdhury, S.,** Barra, E., & Laugier, M. T. (2005). Hardness measurement of CVD diamond coatings on SiC substrates. *Surface and Coatings Technology*, *193*(1), 200–205. https://doi.org/10.1016/j.surfcoat.2004.08.131

37. **Choy, K.** (2003). Chemical vapour deposition of coatings. *Progress in Materials Science*, *48*(2), 57–170. https://doi.org/10.1016/S0079-6425(01)00009-3

38. **Christian, W.** (2002). Chapter 13—Growth From The Vapour Phase. In J. W. Christian (Ed.), *The Theory of Transformations in Metals and Alloys* (pp. 553–622). Pergamon. https://doi.org/10.1016/B978-008044019-4/50018-0

39. **Dadashi, Z.,** Azadi, M., & Hafazeh, A. (2024). Electrochemical characteristics of nano-structure TiCN coatings on the tool steel deposited by PACVD in various solutions. *Results in Chemistry*, *7*, 101531. https://doi.org/10.1016/j.rechem.2024.101531

40. **Dai, W.,** Li, X., & Wang, Q. (2020). Microstructure and properties of TiB2/Cr multilayered coatings with double periodical structures. *Surface and Coatings Technology*, *382*, 125150. https://doi.org/10.1016/j.surfcoat.2019.125150

41. **Danek, M.,** Fernandes, F., Cavaleiro, A., & Polcar, T. (2017). Influence of Cr additions on the structure and oxidation resistance of multilayered TiAlCrN films. *Surface and Coatings Technology*, *313*, 158–167. https://doi.org/10.1016/j.surfcoat.2017.01.053

42. **Das, S.,** Guha, S., Das, P. P., & Ghadai, R. K. (2020). Analysis of morphological, microstructural, electrochemical and nano mechanical characteristics of TiCN coatings prepared under $N_2$ gas flow rate by chemical vapour deposition (CVD) process at higher temperature. *Ceramics International*, *46*(8, Part A), 10292–10298. https://doi.org/10.1016/j.ceramint.2020.01.023

43. **Das, S.,** Guha, S., Ghadai, R., & Sharma, A. (2021). Influence of nitrogen gas over microstructural, vibrational and mechanical properties of CVD Titanium nitride (TiN) thin film coating. *Ceramics International*, *47*(12), 16809–16819. https://doi.org/10.1016/j.ceramint.2021.02.254

44. **Derakhshandeh, R.,** Eshraghi, M. J., & Razavi, M. (2023). Recent developments in the new generation of hard coatings applied on cemented carbide cutting tools. *International Journal of Refractory Metals and Hard Materials*, *111*, 106077. https://doi.org/10.1016/j.ijrmhm.2022.106077

45. **Din, H.,** Shah, M. A., & Sheikh, N. A. (2018). Tribological Performance of Titanium Alloy Ti–6Al–4V via CVD–diamond Coatings. *Journal of Superhard Materials*, *40*(1), 26–39. https://doi.org/10.3103/S1063457618010057

46. **Du, L.,** Wang, S., Du, Y., Qiu, L., Chen, Z., Chen, X., Liu, Z.-K., & Cong, Z. (2018). Deposition of CVD-TiCN and TiAlN coatings guided with thermodynamic calculations. *International Journal of Materials Research, 109*. https://doi.org/10.3139/146.111613

47. **El Azhari, I.,** García, J., Zamanzade, M., Soldera, F., Pauly, C., Motz, C., Llanes, L., & Mücklich, F. (2020). Micromechanical investigations of CVD coated WC-Co cemented carbide by micropillar compression. *Materials & Design, 186,* 108283. https://doi.org/10.1016/j.matdes.2019.108283

48. **Engdahl, C.** (2006). *CVD Diamond Coated Rotating Tools for Composite Machining*. 2006-01–3153. https://doi.org/10.4271/2006-01-3153

49. **Fan, J.,** Xu, Y. X., Geng, D., Chen, L., & Wang, Q. (2024). Improving the oxidation resistance of TiAlN/CrAlO coatings through CrAlON interlayer. *Surface and Coatings Technology, 479,* 130545. https://doi.org/10.1016/j.surfcoat.2024.130545

50. **Fischer Cripps,** (2007). *Introduction to contact mechanics* (Vol. 101). New York: Springer. ISBN 9780387681887

51. **Gao, J.,** Li, C., Wang, N., & Du, Z. (2008). Thermodynamic analysis of the Ti-Al-N system. *Journal of University of Science and Technology Beijing, Mineral, Metallurgy, Material, 15*(4), 420–424. https://doi.org/10.1016/S1005-8850(08)60079-1

52. **Gao, J.,** & Zhang, Y.-W. (2017). Chapter 8—Theoretical Studies on the Growth Mechanism of Chemical Vapor Deposition of Graphene on Metal Surface. In G. Zhang (Ed.), *Thermal Transport in Carbon-Based Nanomaterials* (pp. 205–241). Elsevier. https://doi.org/10.1016/B978-0-32-346240-2.00008-X

53. **García, J.,** Moreno, M., Wan, W., Apel, D., Pinto, H., Meixner, M., Klaus, M., & Genzel, C. (2021). In Situ Investigations on Stress and Microstructure Evolution in Polycrystalline Ti(C,N)/α-$Al_2O_3$ CVD Coatings under Thermal Cycling Loads. *Crystals*, *11*, 158. https://doi.org/10.3390/cryst11020158

54. **Garcia, J.,** Pitonak, R., Weissenbacher, R., & Köpf, A. (2010). Production and characterization of wear resistant Ti(C,N) coatings manufactured by modified chemical vapor deposition process. *Surface and Coatings Technology*, *205*(7), 2322–2327. https://doi.org/10.1016/j.surfcoat.2010.09.013

55. **Gissler, W.,** & Jehn, H. A. (1992). *Advanced Techniques for Surface Engineering*. Springer Science & Business Media, Volume 1. ISBN 978-90-481-4214-9

56. **Gupta, P.,** & Meletis, E. I. (2004). Tribological behavior of plasma-enhanced CVD a-C:H films. Part II: multinanolayers. *Tribology International*, *37*(11), 1031–1038. https://doi.org/10.1016/j.triboint.2004.07.021

57. **Hamedi, J.,** Torkamany, M. J., & Sabbaghzadeh, J. (2011). Effect of pulsed laser parameters on in-situ TiC synthesis in laser surface treatment. *Optics and Lasers in Engineering, 49*(4), 557–563. https://doi.org/10.1016/j.optlaseng.2010.12.002

58. **Han, G.,** Nam, K. H., & Choi, I. S. (1998). The shear impact wear behavior of Ti compound coatings. *Wear, 214*(1), 91–97. https://doi.org/10.1016/S0043-1648(97)00205-6

59. **Hayward, P.,** Singer, I. L., & Seitzman, L. E. (1992). Effect of roughness on the friction of diamond on cvd diamond coatings. *Wear*, *157*(2), 215–227. https://doi.org/10.1016/0043-1648(92)90063-E

60. **Herzler, J.,** & Roth, P. (2002). High-temperature decomposition of TiCl4 based on Cl-concentration measurements. *Proceedings of the Combustion Institute*, *29*(1), 1353–1359. https://doi.org/10.1016/S1540-7489(02)80166-3

61. **Hitchman, M.,** & Jensen, K. (1993). *Chemical vapor deposition: Principles and applications.* Academic Press. ISBN: 978-0123496706

62. **Hogmark, S.,** Jacobson, S., & Larsson, M. (2000). Design and evaluation of tribological coatings. *Wear*, *246*(1), 20–33. https://doi.org/10.1016/S0043-1648(00)00505-6

63. **Holmberg, K.,** & Matthews, A. (2009). *Coatings tribology: Properties, mechanisms, techniques and applications in surface engineering* (2 ed). Elsevier Science. IBSN: 9780444527509

64. **Hou, M.,** Ouyang, M., Chen, H. F., Liu, W. M., Xue, Z. Q., Wu, Q. D., Zhang, H. X., Gao, H. J., & Pang, S. J. (1998). Fractal structure in the silver oxide thin film. *Thin Solid Films*, *315*(1), 322–326. https://doi.org/10.1016/S0040-6090(97)00713-X

65. **Hovorun, T.,** Khaniukov, K., Varakin, V., Pererva, V., Vorobiov, S., Burlaka, A., & Khvostenko, R. (2021). Improvement of the Physical and Mechanical Properties of the Cutting Tool by Applying Wear-resistant Coatings Based on Ti, Al, Si, and N. Journal of Engineering Sciences, 8. https://doi.org/10.21272/jes.2021.8(2).c3

66. **Hsieh, H.,** Tan, A. L. K., & Zeng, X. T. (2006). Oxidation and wear behaviors of Ti-based thin films. *Surface and Coatings Technology*, *201*(7), 4094–4098. https://doi.org/10.1016/j.surfcoat.2006.08.026

67. **Huang, Y.,** Zhu, L., Liu, Z., & Bian, Y. (2023). The effect of WC-Co substrates on TiN/TiCN/$Al_2O_3$ /TiCNO multilayer coatings. *Surface Engineering*, *39*(6), 722–737. https://doi.org/10.1080/02670844.2023.2252660

68. **Hutchings, I.,** & Shipway, P. (2017). Tribology: Friction and wear of engineering materials: Second Edition. In *Tribology: Friction and Wear of Engineering Materials: Second Edition* (p. 388).

69. **Jacobson, S.,** & Hogmark, S. (2010). *Tribofilms – On the crucial importance of tribologically induced surface modifications*. ISBN: 978-81-308-0377-7

70. **Jakab M.** (2023). *Biomorf hidroxiapatit kerámiák és üvegkerámiák előállítása* [Phd, Pannon Egyetem]. https://doi.org/10.18136/PE.2023.835

71. **Jen Fin Lin** & Jeng Haur Horng. (1994). Analysis of the tribological behaviour and wear mechanisms of titanium nitride coating. *Wear*, *171*(1), 59–69. https://doi.org/10.1016/0043-1648(94)90348-4

72. **Jin, N.,** Yang, Y., Luo, X., & Xia, Z. (2013). Development of CVD Ti-containing films. *Progress in Materials Science*, *58*(8), 1490–1533. https://doi.org/10.1016/j.pmatsci.2013.07.001

73. **Jing, K.,** Guo, Z., Hua, T., Xiong, J., Liao, J., Liang, L., Yang, S., Yi, J., & Zhang, H. (2022). Strengthening mechanism of cemented carbide containing Re. *Materials Science and Engineering: A*, *838*, 142803. https://doi.org/10.1016/j.msea.2022.142803

74. **Juarez, F.,** Monceau, D., Tetard, D., Pieraggi, B., & Vahlas, C. (2003). Chemical vapor deposition of ruthenium on NiCoCrAlYTa powders followed by thermal oxidation of the sintered coupons. Surface and Coatings Technology, 163–164, 44–49. https://doi.org/10.1016/S0257-8972(02)00592-3

75. **Kafizas, A.,** Carmalt, C., & Parkin, I. (2013). CVD and precursor chemistry of transition metal nitrides. *Coordination Chemistry Reviews*, *257*, 2073–2119. https://doi.org/10.1016/j.ccr.2012.12.004

76. **Kainz, C.,** Schalk, N., Tkadletz, M., Mitterer, C., & Czettl, C. (2019). Microstructure and mechanical properties of CVD TiN/TiBN multilayer coatings. *Surface and Coatings Technology*, *370*, 311–319. https://doi.org/10.1016/j.surfcoat.2019.04.086

77. **Kajikawa, Y.** (2008). Roughness evolution during chemical vapor deposition. *Materials Chemistry and Physics*, *112*(2), 311–318. https://doi.org/10.1016/j.matchemphys.2008.06.008

78. **Kenzhegulov, A.,** Mamaeva, A., Panichkin, A., Alibekov, Z., Kshibekova, B., Bakhytuly, N., & Wieleba, W. (2022). Comparative Study of Tribological and Corrosion Characteristics of TiCN, TiCrCN, and TiZrCN Coatings. *Coatings*, *12*(5), Article 5. https://doi.org/10.3390/coatings12050564

79. **Kim, H.,** Kim**,** C. Y., Kim, D. W., Lee, I. S., Lee, G. H., Park, J. C., Lee, S. J., & Lee, K. Y. (2010). Wear performance of self-mating contact pairs of TiN and TiAlN coatings on orthopedic grade Ti-6Al-4V. *Biomedical Materials (Bristol, England)*, *5*(4), 044108. https://doi.org/10.1088/1748-6041/5/4/044108

80. **Kimura, A.,** Murakami, T., Yamada, K., & Suzuki, T. (2001). Hot-pressed Ti-Al targets for synthesizing Ti1−xAlxN films by the arc ion plating method. *Thin Solid Films*, *382*(1), 101–105. https://doi.org/10.1016/S0040-6090(00)01692-8

81. **Koller, C. M.,** Hollerweger, R., Sabitzer, C., Rachbauer, R., Kolozsvári, S., Paulitsch, J., & Mayrhofer, P. H. (2014). Thermal stability and oxidation resistance of arc evaporated TiAlN, TaAlN, TiAlTaN, and TiAlN/TaAlN coatings. *Surface and Coatings Technology*, *259*, 599–607. https://doi.org/10.1016/j.surfcoat.2014.10.024

82. **Kumar, S.,** Mondal, S., Kumar, A., Ranjan, A., & Prasad, N. (2017). Chemical Vapor Deposition of TaC/SiC on Graphite Tube and Its Ablation and Microstructure Studies. *Coatings*, *7*, 101. https://doi.org/10.3390/coatings7070101

83. **Laikhtman, A.,** Rapoport, L., Perfilyev, V., Moshkovich, A., Akhvlediani, R., & Hoffman, A. (2009). Tribological and Adhesion Properties of CVD Diamond Films Grown on Steel with a CrN Interlayer. *AIP Conference Proceedings*, *1151*. https://doi.org/10.1063/1.3203226

84. **Larsson, A.,** & Ruppi, S. (2002). Microstructure and properties of Ti(C,N) coatings produced by moderate temperature chemical vapour deposition. *Thin Solid Films*, *402*(1), 203–210. https://doi.org/10.1016/S0040-6090(01)01712-6

85. **Lavrinenko, I.** (2022). CVD Diamonds in Diamond Tools: Features and Properties, Peculiarities of Processing, and Application in Modern Diamond Tools (Review). *Journal of Superhard Materials*, *44*(6), 431–449. https://doi.org/10.3103/ S106345 7622060077

86. **Leroux, P.** (2014). *Automated Multi Sample Scratch Testing*. https://doi.org/10.131 40/RG.2.1.1022.8644

87. **Lim, H.,** Lim, S. C., & Lee, K. S. (1999). Wear of TiC-coated carbide tools in dry turning. *Wear*, *225–229*, 354–367. https://doi.org/10.1016/S0043-1648(98)00366-4

88. **Liu, Y.,** Liu, H. D., Pelenovich, V., Wan, Q., Guo, J. L., Chen, Y. M., Zhang, J., Xue, L. J., Li, Z. G., & Yang, B. (2021). Influences of modulation period on structure and properties of AlTiSiN/AlCrSiN nanocomposite multilayer coatings. *Vacuum*, *193*, 110516. https://doi.org/10.1016/j.vacuum.2021.110516

89. **Love, A.,** Middleman, S., & Hochberg, A. K. (1993). The dynamics of bubblers as vapor delivery systems. *Journal of Crystal Growth*, *129*(1), 119–133. https://doi.org/ 10.1016/0022-0248(93)90441-X

90. **Madar, R.,** Rouault, A., Blanquet, E., Bernard, C., & Dutron, A.-M. (2001). *Non-plasma CVD method and apparatus of forming Ti1-xA1xN coatings* (United States/Patent/US6238739B1).https://patents.google.com/patent/US6238739B1/en

91. **Martin,** P. M. (2010). *Handbook of Deposition Technologies for Films and Coatings: Science, Applications and Technology*. William Andrew. ISBN: 978-0-8155-2031-3

92. **Mayrhofer, P.,** Mitterer, C., Hultman, L., & Clemens, H. (2006). Microstructural Design of Hard Coatings. *Progress in Materials Science*, *51*, 1032–1114. https://doi.org/10.1016/j.pmatsci.2006.02.002

93. **Mei, H.,** Lin, C., Li, Y., Shen, Y., Li, Q., Wang, R., Zeng, W., Mei, W., & Gong, W. (2023). Effect of V/Mo Atomic Ratio on the Microstructure and Mechanical Properties of MoVCuN Coatings. *Materials*, *17*(1), 229. https://doi.org/10.3390/ma17010229

94. **Moritz, Y.,** Kainz, C., Peritsch, P., Mitterer, C., & Schalk, N. (2023). Oxidation mechanism of sputter deposited model SiNx/TiN/SiNx coatings. *Surface and Coatings Technology*, 468, 129753. https://doi.org/10.1016/j.surfcoat.2023.129753

95. **Movchan, A.,** & Demchishin, A. V. (1969). Structure and properties of thick condensates of nickel, titanium, tungsten, aluminum oxides, and zirconium dioxide in vacuum. Fiz. *Metal. Metalloved.* 28: 653-60. https://www.osti.gov/biblio/4181669

96. **Naik, S. N.,** & Walley, S. M. (2020). The Hall–Petch and inverse Hall–Petch relations and the hardness of nanocrystalline metals. *Journal of Materials Science*, *55*(7), 2661–2681. https://doi.org/10.1007/s10853-019-04160-w

97. **Narasimhan, K.,** Boppana, S. P., & Bhat, D. G. (1995). Development of a graded TiCN coating for cemented carbide cutting tools—A design approach. *Wear*, *188*(1), 123–129. https://doi.org/10.1016/0043-1648(95)06635-7

98. **Nilsson, M.,** & Olsson, M. (2011). Tribological testing of some potential PVD and CVD coatings for steel wire drawing dies. *Wear*, *273*(1), 55–59. https://doi.org/10.1016/j.wear.2011.06.020

99. **Noel, S.,** & Kovar, D. (2002). Laser chemical vapor deposition of TiC on tantalum. *Journal of Materials Science*, *37*(4), 689–697. https://doi.org/10.1023/A:1013871326880

100. **Ohring, M.** (1992). *The Materials Science of Thin Films*. Academic Press. ISBN: 978-0-12-524975-1

101. **Pal, S.,** & Deevi, S. C. (2003). Single layer and multilayer wear resistant coatings of (Ti,Al)N: A review. *Materials Science and Engineering: A*, *342*(1), 58–79. https://doi.org/10.1016/S0921-5093(02)00259-9

102. **Pang, H.,** Hu, Y.-K., Zhai, S.-J., Zhang, Q.-C., Ma, L.-J., & Feng, Q.-G. (2022). High temperature oxidation and tribological properties of cemented carbide material under different cooling condition. *International Journal of Refractory Metals and Hard Materials*, *108*, 105937. https://doi.org/10.1016/j.ijrmhm.2022.105937

103. **Patscheider, J.** (2003). Nanocomposite Hard Coatings for Wear Protection. *MRS Bulletin*, *28*(3), 180–183. https://doi.org/10.1557/mrs2003.59

104. **Pedersen, H.,** & Elliott, S. (2014). Studying chemical vapor deposition processes with theoretical chemistry. *Theoretical Chemistry Accounts*, *133*, 1476. https://doi.org/10.1007/s00214-014-1476-7

105. **Peng, D.,** Li, Z., Wu, H., Cong, D., Huang, A., Song, K., Zhang, M., Wang, X., Wei, Y., Jiang, B., Du, J., Bai, Y., & Ding, X. (2023). Sliding friction behaviors of TiCN/Cr3C2-NiCr and TiCN/WC-CoCr duplex coatings fabricated by combining HVOF and HT-CVD procedures. *Surface and Coatings Technology*, *474*, 130078. https://doi.org/10.1016/j.surfcoat.2023.130078

106. **Peng, Y.,** Miao, H., & Peng, Z. (2013). Development of TiCN-based cermets: Mechanical properties and wear mechanism. *International Journal of Refractory Metals and Hard Materials*, *39*, 78–89. https://doi.org/10.1016/j.ijrmhm.2012.07.001

107. **Pierson, H. O.** (1999). *Handbook of Chemical Vapor Deposition (CVD) principles, technology, and applications* (2 ed). Noyes Publications : William AndrewPublishing. http://www.sciencedirect.com/science/book/9780815514329

108. **Qian, C.,** Liu, Y., Cheng, H., Li, K., Liu, B., & Zhang, X. (2022). The Effect of Carbon Content on the Microstructure and Mechanical Properties of Cemented Carbides with a CoNiFeCr High Entropy Alloy Binder. *Materials*, *15*(16), Article 16. https://doi.org/10.3390/ma15165780

109. **Qiu, L.,** Chen, H., Zeng, F., Zhou, S., & Du, Y. (2024). Microstructure, mechanical properties and cutting performance of super-hard Ti(B,C,N) coatings prepared by chemical vapor deposition method. *Surface and Coatings Technology*, *480*, 130599. https://doi.org/10.1016/j.surfcoat.2024.130599

110. **Rabinowicz, E.** (1995). *Friction and Wear of Materials* (2nd edition). Wiley-Interscience. ISBN: 978-0-471-83084-9

111. **Ragothuman, A.,** Kanthi Natarajan, G. V., & Shanmugavel, B. P. (2019). Wear and thermal stability of TiCN-WC-Co-Cr3C2 cermets modified by TiN. *International Journal of Refractory Metals and Hard Materials*, *84*, 105020. https:// doi.org/10.1016 /j.ijrmhm.2019.105020

112. **Rebouta, L.** (1995). Oxidation resistance of (Ti,Al,Zr,Si)N coatings in air. *Surface and Coatings Technology*. https://www.academia.edu/105158581/Oxidation_resistance _of_Ti_Al_Zr_Si_N_coatings_in_air

113. **Rickerby, S.,** & Matthews, A. (Eds.). (1991). *Advanced surface coatings: A handbook of surface engineering*. Blackie ; Chapman and Hall. ISBN: 0412025418

114. **Rovere, F.,** Mayrhofer, P. H., Reinholdt, A., Mayer, J., & Schneider, J. M. (2008). The effect of yttrium incorporation on the oxidation resistance of Cr–Al–N coatings. *Surface and Coatings Technology*, *202*(24), 5870–5875. https://doi.org/10.1016/ j.surfcoat.2008.06.161

115. **Ruppi, S.,** Ho¨grelius, B., & Huhtiranta, M. (1998). Wear characteristics of TiC, Ti(C,N), TiN and $Al_2O_3$ coatings in the turning of conventional and Ca-treated steels. *International Journal of Refractory Metals and Hard Materials*, *16*(4), 353–368. https://doi.org/10.1016/S0263-4368(98)00039-0

116. **Schalk, N.,** Tkadletz, M., & Mitterer, C. (2022). Hard coatings for cutting applications: Physical vs. chemical vapor deposition and future challenges for the coatings community. *Surface and Coatings Technology*, *429*, 127949. https://doi.org/ 10.101 6/j.surfcoat.2021.127949

117. **Schwanekamp, T.,** Marginean, G., Reuber, M., & Ostendorf, A. (2022). Impact of cobalt content and grain growth inhibitors in laser-based powder bed fusion of WC-Co. *International Journal of Refractory Metals and Hard Materials*, *105*, 105814. https://doi.org/10.1016/j.ijrmhm.2022.105814

118. **Shen, T.,** Zhu, L., & Liu, Z. (2020). Effect of micro-blasting on the tribological properties of TiN/MT-TiCN/$Al_2O_3$/TiCNO coatings deposited by CVD. *International Journal of Refractory Metals and Hard Materials*, *88*, 105205. https://doi. org/10.1016/j.ijrmhm.2020.105205

119. **Shi, Z.,** Zhang, D., Chen, S., & Wang, T. (2013). Effect of nitrogen content on microstructures and mechanical properties of Ti(C, N)-based cermets. *Journal of Alloys and Compounds*, *568*, 68–72. https://doi.org/10.1016/j.jallcom.2013.03.138

120. **Singh, A. K.,** Nath, A. K., Pratihar, D. K., & Choudhury, A. R. (2024). Development and Performance of Additively Manufactured Tungsten Carbide Tool Insert: An Application of Additive Manufacturing Towards Flexible and Customized Machining. *Tribology International*, 109780. https://doi.org/10.1016/j.triboint.2024.109780

121. **Sousa & Silva.** (2020). Recent Advances in Turning Processes Using Coated Tools—A Comprehensive Review. *Metals*, *10*, 170. https://doi.org/10.3390/met10020170

122. **Stylianou, R.,** Velic, D., Daves, W., Ecker, W., Tkadletz, M., Schalk, N., Czettl, C., & Mitterer, C. (2020). Thermal crack formation in TiCN/α-$Al_2O_3$ bilayer coatings grown by thermal CVD on WC-Co substrates with varied Co content. *Surface and Coatings Technology*, *392*, 125687. https://doi.org/10.1016/j.surfcoat.2020.125687

123. **Terek, V.,** Kovačević, L., Drnovšek, A., Panjan, P., Škorić, B., Kovač, J., Bobić, Z., & Terek, P. (2024). High-temperature tribological behavior of nanolayered TiAlN/TiSiN coating deposited on WC-Co cemented carbide. *Surface and Coatings Technology*, *477*, 130316. https://doi.org/10.1016/j.surfcoat.2023.130316

124. **Thornton, A.** (1974). Influence of apparatus geometry and deposition conditions on the structure and topography of thick sputtered coatings. *Journal of Vacuum Science and Technology*, *11*(4), 666–670. https://doi.org/10.1116/1.1312732

125. **Todt, J.,** Zalesak, J., Daniel, R., Pitonak, R., Köpf, A., Weißenbacher, R., Sartory, B., Mitterer, C., & Keckes, J. (2016). Al-rich cubic $Al_{0.8}Ti_{0.2}N$ coating with self-organized nano-lamellar microstructure: Thermal and mechanical properties. *Surface and Coatings Technology*, *291*, 89–93. https://doi.org/10.1016/j.surfcoat.2016.02.027

126. **Tsujimoto, A.,** Barkmeier, W. W., Fischer, N. G., Nojiri, K., Nagura, Y., Takamizawa, T., Latta, M. A., & Miazaki, M. (2018). Wear of resin composites: Current insights into underlying mechanisms, evaluation methods and influential factors. *Japanese Dental Science Review*, *54*(2), 76–87. https://doi.org/10.1016/j.jdsr.2017.11.002

127. **Tyagi, A.,** Walia, R. S., & Murtaza, Q. (2019). Tribological behavior of temperature dependent environment friendly thermal CVD diamond coating. *Diamond and Related Materials*, *96*, 148–159. https://doi.org/10.1016/j.diamond.2019.05.003

128. **Vasu, Ch.,** Andhare, A. B., & Dumpala, R. (2024). Machinability and tool wear studies on AZ91/B4C metal matrix composites using uncoated and CVD diamond coated WC-Co turning inserts. *International Journal of Refractory Metals and Hard Materials*, *119*, 106538. https://doi.org/10.1016/j.ijrmhm.2023.106538

129. **Vogiatzis, S.,** Papageorgiou, V., Strakov, H., & Auger, M. (2017). *CVD TiAlN technology-Coating properties and applications*. International conference: 19th Plansee Seminar, 29 May – 2 June, 2017. Reutte, Austria.

130. **Von Fieandt, L.,** Johansson, K., Larsson, T., Boman, M., & Lindahl, E. (2018). On the growth, orientation and hardness of chemical vapor deposited Ti(C,N). *Thin Solid Films*, *645*, 19–26. https://doi.org/10.1016/j.tsf.2017.10.037

131. **Veprek, S.,** Veprek-Heijman, M. G. J., Karvankova, P., & Prochazka, J. (2005). Different approaches to superhard coatings and nanocomposites. Thin Solid Films, 476(1), 1–29. https://doi.org/10.1016/j.tsf.2004.10.053

132. **Wächtler, C.,** Wüstefeld, C., Šíma, M., Pikner, J., & Rafaja, D. (2024). Effect of the substrate treatment on the microstructure of CVD Ti(C,N)/α-$Al_2O_3$/TiN hard coatings. *Surface and Coatings Technology*, *477*, 130296. https://doi.org/10.1016/j.surfcoat.2023.130296

133. **Wagner, J**. (2007). *Chemical vapor deposition of titanium nitride-based hard coatings* (Doctoral dissertation). Montanuniversität, Leoben, Austria.

134. **Wagner, J.,** Hochauer, D., Mitterer, C., Penoy, M., Michotte, C., Wallgram, W., & Kathrein, M. (2006). The influence of boron content on the tribological performance of Ti–N–B coatings prepared by thermal CVD. *Surface and Coatings Technology*, *201*(7), 4247–4252. https://doi.org/10.1016/j.surfcoat.2006.08.071

135. **Wang, F.,** & Wu, J. (2023). Chapter 13—Applications in information display films. In F. Wang & J. Wu (Eds.), *Modern Ion Plating Technology* (pp. 341–363). Elsevier. https://doi.org/10.1016/B978-0-323-90833-7.00013-9

136. **Wang, H.,** Webb, T., & Bitler, J. (2015). Study of thermal expansion and thermal conductivity of cemented WC–Co composite. *International Journal of Refractory Metals and Hard Materials*, *49*, 170–177. https://doi.org/10.1016/j.ijrmhm.2014.06.009

137. **Wang, Z.,** Xiong, J., Guo, Z., Yang, T., Liu, J., & Chai, B. (2019). The microstructure and properties of novel Ti(C,N)-based cermets with multi-component CoCrFeNiCu high-entropy alloy binders. *Materials Science and Engineering: A*, *766*, 138345. https://doi.org/10.1016/j.msea.2019.138345

138. **Weber, B.,** Scheibert, J., de Boer, M. P., & Dhinojwala, A. (2022). Experimental insights into adhesion and friction between nominally dry rough surfaces. *MRS Bulletin*, *47*(12), 1237–1246. https://doi.org/10.1557/s43577-022-00464-6

139. **Wei, X.,** Yue, C., Hu, D., Liu, X., Ding, Y., & Liang, S. Y. (2022). Research on Surface Roughness of Supersonic Vibration Auxiliary Side Milling for Titanium Alloy. *Chinese Journal of Mechanical Engineering*, *35*(1), 101. https://doi.org/10.1186/s10033-022-00770-9

140. **Weiser, M.,** Chater, R. J., Shollock, B. A., & Virtanen, S. (2019). Transport mechanisms during the high-temperature oxidation of ternary γ/γ′ Co-base model alloys. *Npj Materials Degradation*, *3*(1), 1–11. https://doi.org/10.1038/s41529-019-0096-z

141. **Xin, T.,** Pei, H., & Shucai, Y. (2022). Coating and micro-texture techniques for cutting tools. *Journal of Materials Science*, *57*(36), 17052–17104. https://doi.org/10.1007/s10853-022-07704-9

142. **Yalçin, D.,** Güler, O., Karabacak, A. H., Çanakçi, A., Varol, T., Kocaman, M., Çelebi, M., & Akçay, S. B. (2024). Pre-hardening water quenching effect on the wear resistance of TiCN coated 4140 steels. *Surface and Coatings Technology*, *480*, 130591. https://doi.org/10.1016/j.surfcoat.2024.130591

143. **Yang, L.,** Xiong, J., Chen, X., Li, X., Deng, C., Zhang, D., & Yi, L. (2023). Study on the growth and wear characters of CVD coating deposited on Ti(C, N)-based cermets with adding different C/N ratios of Ti(C, N) powders. *Ceramics International*, *49*(11, Part B), 18023–18034. https://doi.org/10.1016/j.ceramint.2023.02.255

144. **Yoon, Y.,** Kim, J., & Kim, K. (2002). A comparative study on tribological behavior of TiN and TiAlN coatings prepared by arc ion plating technique. *Surface & Coatings Technology - Surf Coat Tech*, *161*, 237–242. https://doi.org/10.1016/S0257-8972(02)00474-7

145. **You, Q.,** Xiong, J., Li, H., Guo, Z., & Huo, Y. (2021). Study on the microstructure and high temperature friction and wear characteristics of three CVD coated cermets.

*International Journal of Refractory Metals and Hard Materials*, *96*, 105495. https://doi.org/10.1016/j.ijrmhm.2021.105495

146. **Yunata, E.,** Aizawa, T., Tamaoki, K., & Kasugi, M. (2017). Plasma Polishing and Finishing of CVD-Diamond Coated WC (Co) Dies for Dry Stamping. *Procedia Engineering*, *207*, 2197–2202. https://doi.org/10.1016/j.proeng.2017.10.981

147. **Zhang, J.,** Zhang, Y., Fu, Y., & Li, H. (2025). Research progress in chemical vapor deposition for high-temperature anti-oxidation/ablation coatings on thermal structural composites. Composites Part B: Engineering, 291, 112015. https://doi.org/10.1016/j .compositesb. 2024. 112015

148. **Zhao, L.,** Zhou, K., Tang, D., Wang, H., Li, D., & Peng, Y. (2022). Experimental and Numerical Study on Friction and Wear Performance of Hot Extrusion Die Materials. *Materials*, *15*(5), 1798. https://doi.org/10.3390/ma15051798

149. **Zhou, J.,** Ouyang, J.-H., Su, W.-T., Kong, X.-R., Xu, C.-G., Li, Y., Wang, Y.-J., Chen, L., & Zhou, Y. (2024). Insights into hardening and strengthening in ultrafine Ti(C, N)-based cermets. *Journal of Alloys and Compounds*, *996*, 174843. https://doi.org/ 10.1016/j.jallcom.2024.174843

150. **Zhu, L.,** Zhang, Y., Hu, T., Leicht, P., & Liu, Y. (2016). Oxidation resistance and thermal stability of Ti(C,N) and Ti(C,N,O) coatings deposited by chemical vapor deposition. *International Journal of Refractory Metals and Hard Materials*, *54*, 295–303. https://doi.org/10.1016/j.ijrmhm.2015.08.006

# Appendix-A

**Publications related to the dissertation:**

I. **Gyurika, I.,** Ali, O., & Jakab, M. Determination of Research Guidelines and Establishing of Test Framework for the Development of New CVD Coating Formulations and New Approach Coating Equipment, Indexed in Springer Nature and Scopus. In STUE (2022), Vol. *536*, pp 420–431. doi.org/10.1007/978-3-031-20141-7_39

II. **Ali, O.,** & Gyurika, I. Recent Advances in Development and Characterization of CVD Multilayer Composite Coatings-A Comprehensive Review. Indexed in Springer Nature Switzerland and Scopus. In ICTM (2022), Vol. *657*, pp 63–75. doi. org/10.1007/978-3-031-36201-9_6

III. **Jakab, M.,** Ali, O., Gyurika, I., Korim, T., & Telegdi, J. (2023). The Tribological Behavior of TiN/TiC CVD Coatings under Dry Sliding Conditions against Zirconia and Steel Counterparts. *Coatings*, *13*. doi.org/10.3390/coatings13050832. IF= 2.9, CiteScore: 5.0

IV. **Ali, O.,** Gyurika, I., Korim, T., & Jakab, M. (2024). A novel approach to investigate oxidation behaviour and mechanical properties of CVD bilayer TiN/TiC coatings. *Processing and Application of Ceramics*, *18*, 213–223. doi.org/10.2298/PAC2402213A. IF5=1.4, CiteScore: 2.2

V. **Ali, O.,** & Gyurika, I. (2024). Oxidation Behaviour of TiC/TiN Coatings Deposited by Chemical Vapor Deposition (CVD): Mechanisms, Structures, and Properties. *Archives of Advanced Engineering Science*, 1–12. doi.org/10.47852/bonviewAAES42022613

VI. **Osamah Ali,** István Gyurika, Tamás Korim, & Miklós Jakab (2024). Comparison of Wear and Friction Properties of Titanium-Nitride Based Coatings, *Hungarian Journal of Industry and Chemistry*, vol. *52*, no. 2, pp. 35–46. DOI: 10.33927/hjic-2024-17 IF= 0.5

# Appendix-B


**Figure B1**: Optical microscopy setup used in the present study.

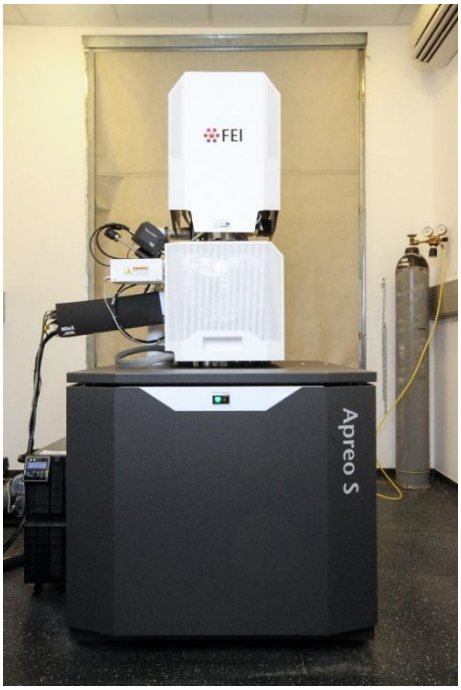


**Figure B2**: Scanning electron microscope (SEM) and energy dispersive spectroscopy (EDS) system.

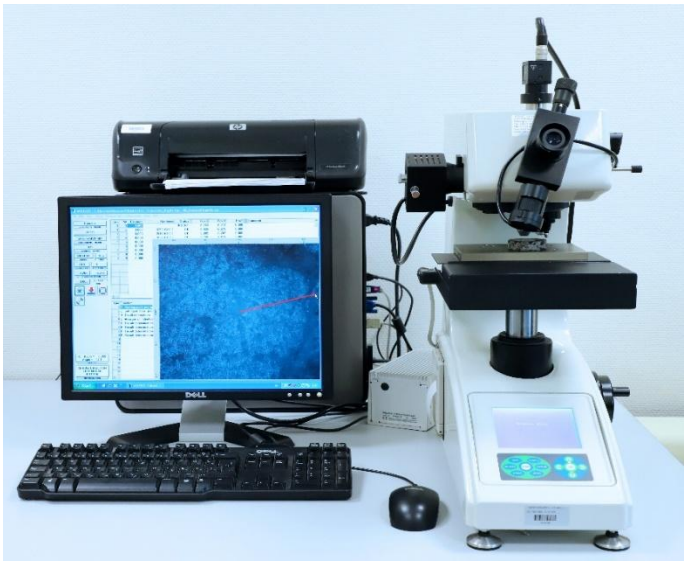

**Figure B3**: Vickers microhardness tester.

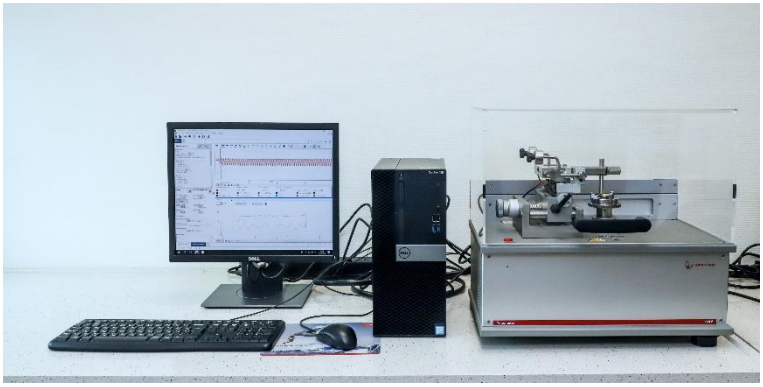

**Figure B4**: TRB3 tribometer used during tribological and scratch tests.

**Figure B5**: High-temperature furnace for oxidation tests.

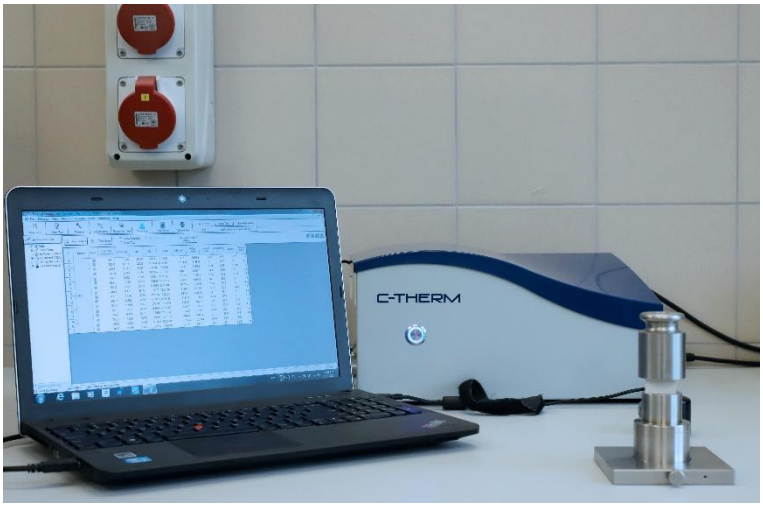


**Figure B6**: C-Therm thermal conductivity analyzer setup.

**Figure B7**: X-ray diffractometer (XRD).

# Appendix-C

**Table C1**: Roughness measurement data for sample A before wear test.

| |
|---|
| Batch Name = 0126 00049 |
| $L_c$ = 0.80mm |
| $L_n$ = 4mm |
| Filter = Gauss |
| Range = 100µm |
| $R_a$ = 0.19µm |
| $R_t$ = 4.50µm |
| $R_v$ = 1.74µm |
| $R_p$ = 0.84µm |
| $R_z$ = 1.74µm |
| $R_c$ = 1.11µm |
| $R_{z1max}$ = 4.50µm |
| $R_{Sm}$ = 16µm |
| $R_q$ = 0.47µm |
| $R_{dq}$ = 13.4° |
| $R_{sk}$ = 0.349 |
| $R_{ku}$ = 5.110 |
| $R_{mr}$ = 0.0% |
| +10.00µm |
| $R_{pc}$ = 0/cm |
| Bandwidth =10.00µm |
| $R_{dc}$ = 1.12µm |
| %1 = 10 %2 = 90 |

**Table C2**: Roughness measurement data for sample B before wear test.

| |
|---|
| Batch Name = 0126 00044 |
| $L_c$ = 0.80mm |
| $L_n$ = 4mm |
| Filter = Gauss |
| Range = 100µm |
| $R_a$ = 0.15µm |
| $R_t$ = 2.16µm |
| $R_v$ = 1.08µm |
| $R_p$ = 0.81µm |
| $R_z$ = 1.65µm |
| $R_c$ = 0.83µm |
| $R_{z1max}$ = 2.12µm |
| $R_{Sm}$ = 14µm |
| $R_q$ = 0.31µm |
| $R_{dq}$ = 12.2° |
| $R_{sk}$ = 0.037 |
| $R_{ku}$ = 3.679 |
| $R_{mr}$ = 0.0% |
| +10.00µm |
| $R_{pc}$ = 0/cm |
| Bandwidth =10.00µm |
| $R_{dc}$ = 0.80µm |
| %1 = 10 %2 = 90 |

**Table C3**: Roughness measurement data for sample A against steel.

| |
|---|
| Batch Name = 0126 00043 |
| $L_c$ = 0.80mm |
| $L_n$ = 4mm |
| Filter = Gauss |
| Range = 100µm |
| $R_a$ = 0.29µm |
| $R_t$ = 2.91µm |
| $R_v$ = 1.51µm |
| $R_p$ = 1.23µm |
| $R_z$ = 2.41µm |
| $R_c$ = 0.84µm |
| $R_{z1max}$ = 2.88µm |
| $R_{Sm}$ = 22µm |
| $R_q$ = 0.42µm |
| $R_{dq}$ = 10.6° |
| $R_{sk}$ = -1.480 |
| $R_{ku}$ = 6.387 |
| $R_{mr}$ = 0.0% |
| +10.00µm |
| $R_{pc}$ = 0/cm |
| Bandwidth =10.00µm |
| $R_{dc}$ = 0.90µm |
| %1 = 10 %2 = 90 |

**Table C4**: Roughness measurement data for sample A against $ZrO_2$.

| |
|---|
| Batch Name = 0126 00042 |
| $L_c$ = 0.80mm |
| $L_n$ = 4mm |
| Filter = Gauss |
| Range = 100µm |
| $R_a$ = 0.42µm |
| $R_t$ = 2.85µm |
| $R_v$ = 1.51µm |
| $R_p$ = 1.37µm |
| $R_z$ = 2.58µm |
| $R_c$ = 0.78µm |
| $R_{z1max}$ = 2.74µm |
| $R_{Sm}$ = 29µm |
| $R_q$ = 0.55µm |
| $R_d$ = 10.7° |
| $R_{sk}$ = -0.562 |
| $R_{ku}$ = 3.124 |
| $R_{mr}$ = 0.0% |
| +10.00µm |
| $R_{pc}$ = 0/cm |
| Bandwidth =10.00µm |
| $R_{dc}$ = 1.58µm |
| %1 = 10 %2 = 90 |

**Table C5:** Roughness measurement data for sample B against steel.

| |
|---|
| Batch Name = 0126 00047 |
| $L_c$ = 4mm |
| $L_n$ = 1.60mm |
| Filter = Gauss |
| Range = 100µm |
| $R_a$ = 0.40µm |
| $R_t$ = 3.03µm |
| $R_v$ = 1.08µm |
| $R_p$ = 1.28µm |
| $R_z$ = 2.55µm |
| $R_c$ = 0.85µm |
| $R_{z1max}$ = 3.03µm |
| $R_{Sm}$ = 27µm |
| $R_q$ = 0.53µm |
| $R_{dq}$ = 11.0° |
| $R_{sk}$ = 0.790 |
| $R_{ku}$ = 3.507 |
| $R_{mr}$ = 0.0% |
| +10.00µm |
| $R_{pc}$ = 0/cm |
| Bandwidth =10.00µm |
| $R_{dc}$ = 1.36µm |
| %1 = 10 %2 = 90 |

**Table C6**: Roughness measurement data for sample B against $ZrO_2$.

| |
|---|
| Batch Name = 0126 00046 |
| $L_c$ = 4mm |
| $L_n$ = 1.60mm |
| Filter = Gauss |
| Range = 100µm |
| $R_a$ = 0.35µm |
| $R_t$ = 3.49µm |
| $R_v$ = 1.74µm |
| $R_p$ = 1.57µm |
| $R_z$ = 3.06µm |
| $R_c$ = 0.97µm |
| $R_{z1max}$ = 3.49µm |
| $R_{Sm}$ = 20µm |
| $R_q$ = 0.50µm |
| $R_{dq}$ = 12.1° |
| $R_{sk}$ = -0.740 |
| $R_{ku}$ = 5.086 |
| $R_{mr}$ = 0.0% |
| +10.00µm |
| $R_{pc}$ = 0/cm |
| Bandwidth =10.00µm |
| $R_{dc}$ = 1.15µm |
| %1 = 10 %2 = 90 |

**Table C7**: Roughness measurement data for sample A against $ZrO_2$ after 1550 m.

| |
|---|
| Batch Name = 0126 00050 |
| $L_c$ = 4mm |
| $L_n$ = 1.60mm |
| Filter = Gauss |
| Range = 100µm |
| $R_a$ = 0.73µm |
| $R_t$ = 5.47µm |
| $R_v$ = 2.18µm |
| $R_p$ = 2.39µm |
| $R_z$ = 4.57µm |
| $R_c$ = 0.87µm |
| $R_{z1max}$ = 5.47µm |
| $R_{Sm}$ = 45µm |
| $R_q$ = 0.94µm |
| $R_{dq}$ = 12.0° |
| $R_{sk}$ = -0.301 |
| $R_{ku}$ = 2.836 |
| $R_{mr}$ = 0.0% |
| +10.00µm |
| $R_{pc}$ = 0/cm |
| Bandwidth =10.00µm |
| $R_{dc}$ = 2.57µm |
| %1 = 10  %2 = 90 |

# Appendix-D

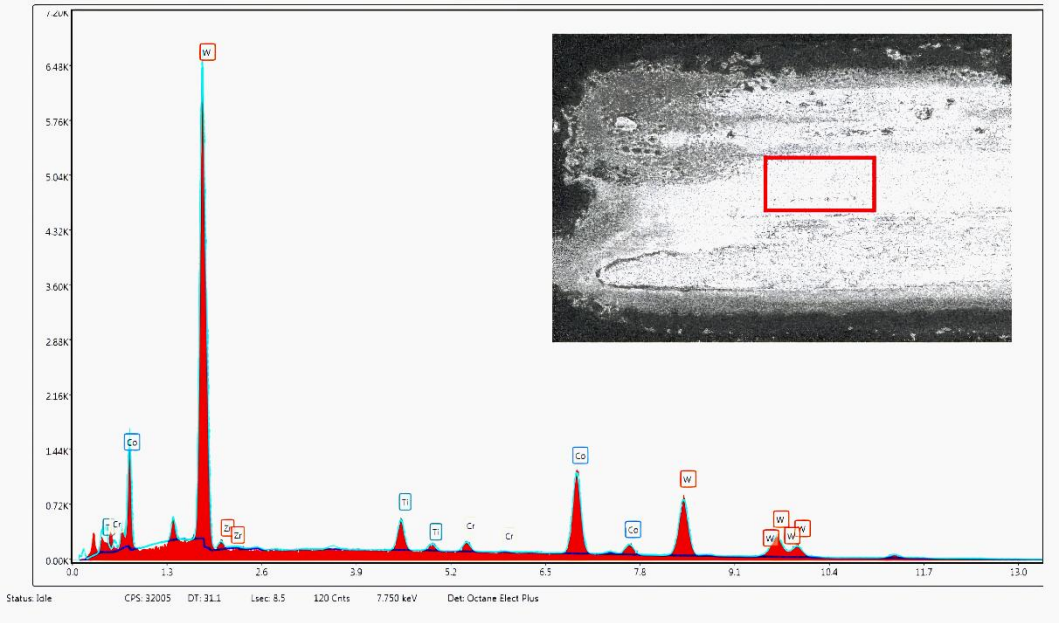


**Figure-D**: EDS Analysis results of the worn-off surface of oxidized sample.

# Appendix-E

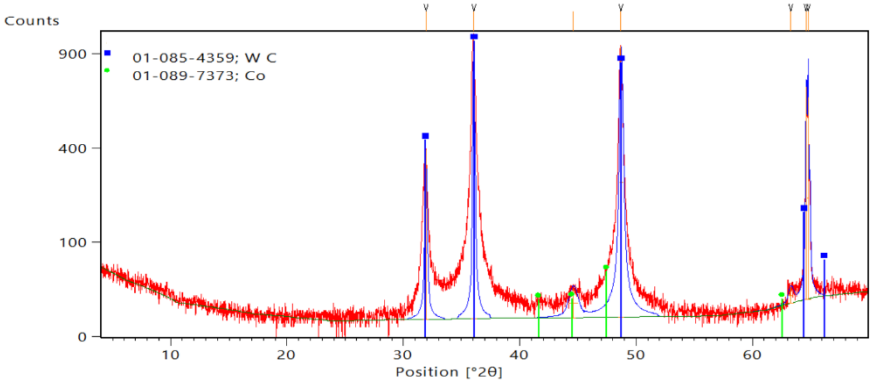


**Figure E-1**: XRD spectrum of WC–Co substrate.

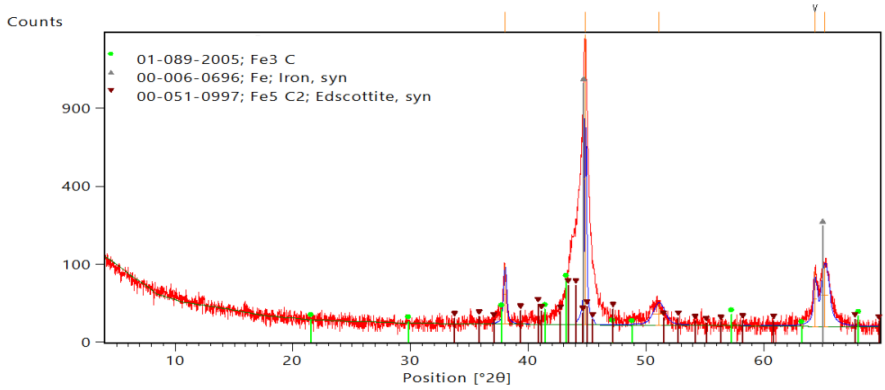


**Figure E-2**: XRD spectrum of steel substrate.

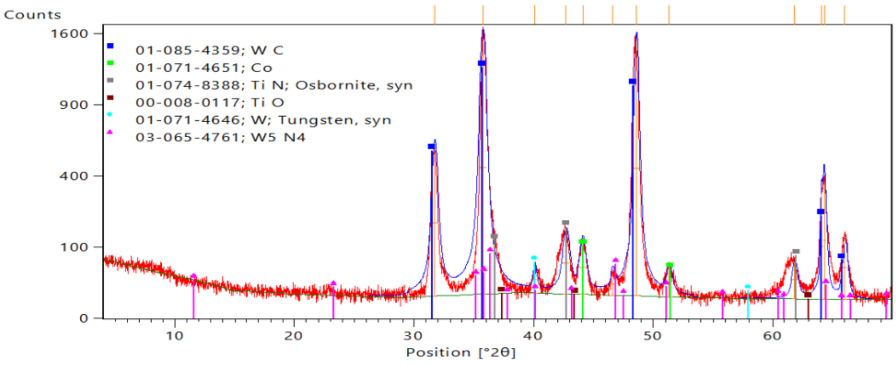


**Figure E-3**: XRD spectrum of TiN1.

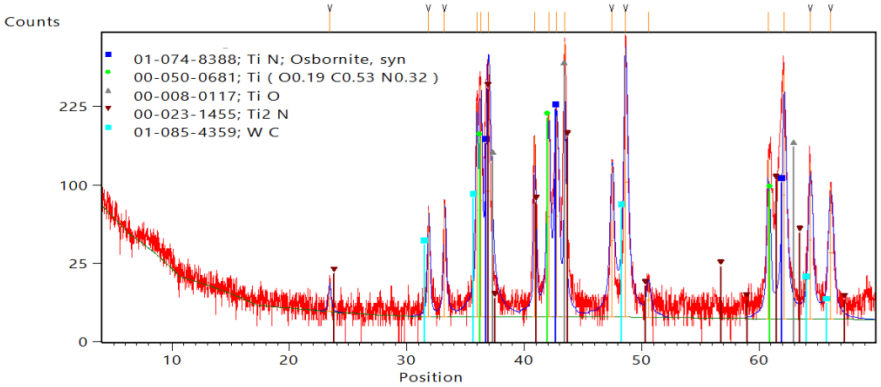


**Figure E-4**: XRD spectrum of TiN2.

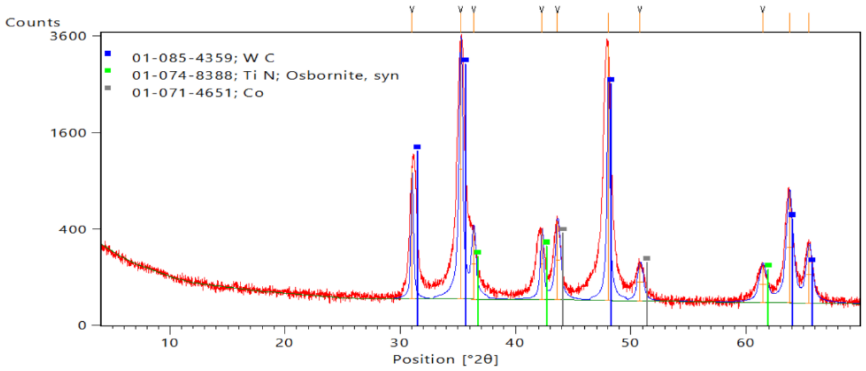


**Figure E-5**: XRD spectrum of TiN3.

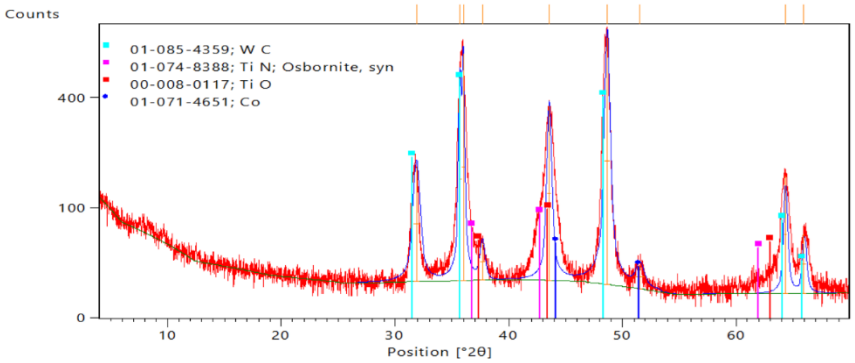


**Figure E-6**: XRD spectrum of TiN4.

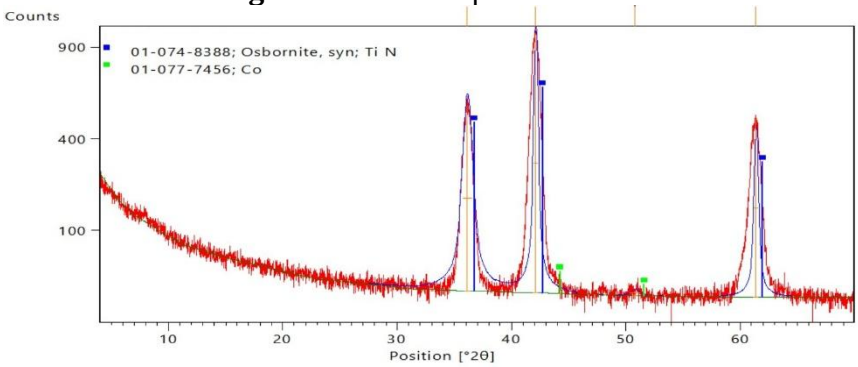


**Figure E-7**: XRD spectrum of TiN5.

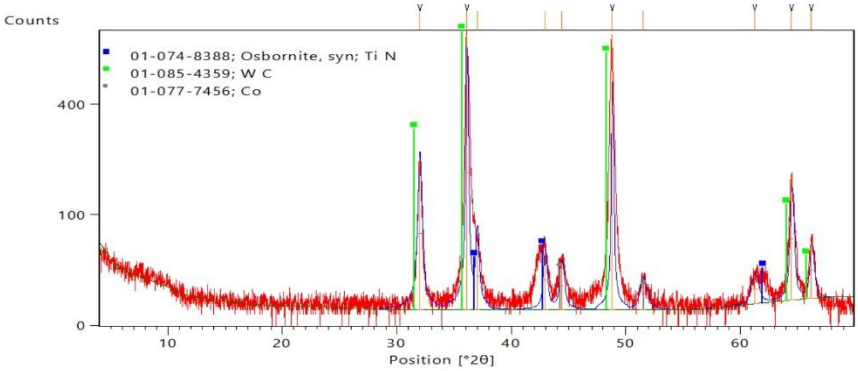


**Figure E-8**: XRD spectrum of TiN6.

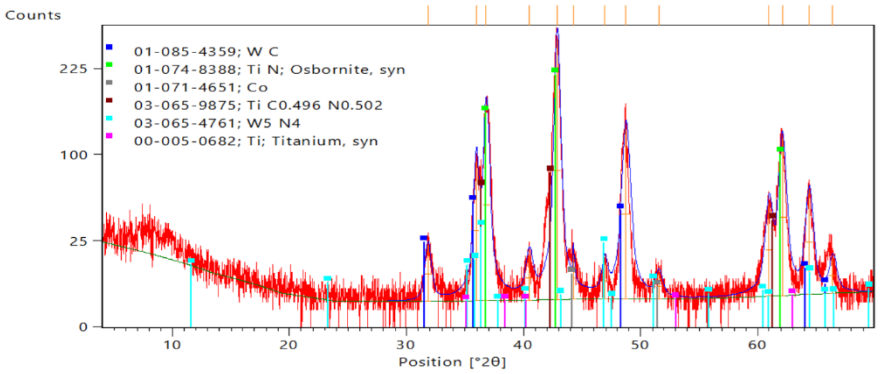


**Figure E-9**: XRD spectrum of TiC/TiN.

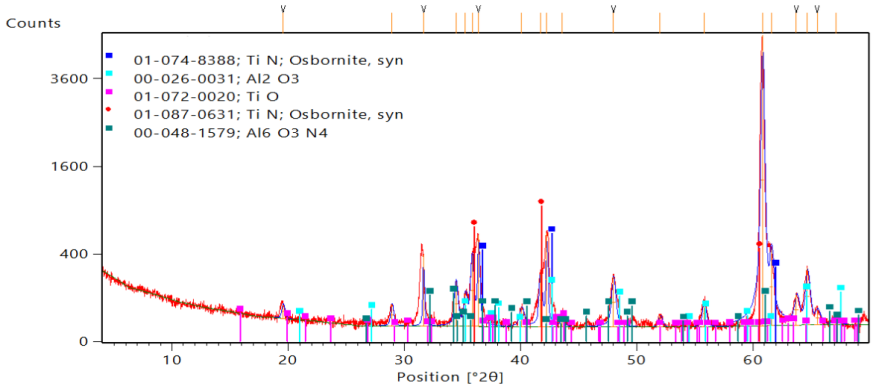


**Figure E-10**: XRD spectrum of TiCN/Al/TiN.

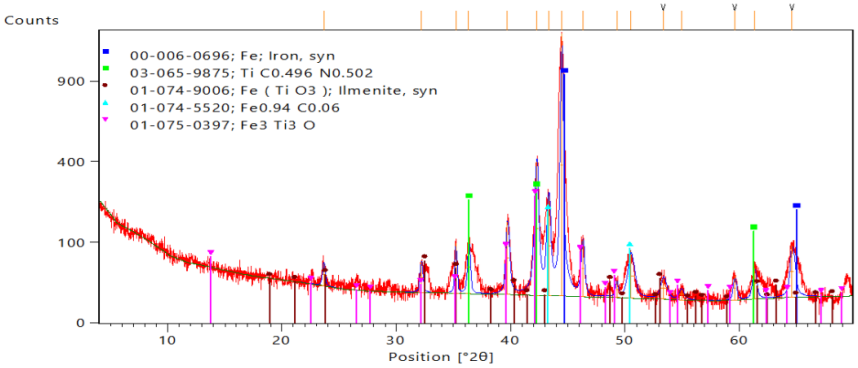


**Figure E-11**: XRD spectrum of TiCN.